

# POLITECNICO DI TORINO

Corso di Laurea Magistrale  
in Ingegneria Energetica e Nucleare

Tesi di Laurea Magistrale

## DEEP BIOGAS CLEANING THROUGH AN INNOVATIVE CRYOGENIC SYSTEM



**Relatore**

Prof. Marta Gandiglio

**Correlatore**

Prof. Andrea Lanzini

**Candidato**

Bruno Giuseppe Cardea

A.A. 2019/2020



## ABSTRACT

---

The present work focuses its attention on the European project Waste2Watss, which aims to design and construct the cleaning system for a biogas-fed Solid Oxide Fuel Cell (SOFC) power plant. Biogas, produced through anaerobic digestion, consisting mainly in methane and carbon dioxide, with a certain amount of contaminants to be removed. For large-scale applications, many biogas cleaning systems are available, based on chemical or biological agents, adsorption/absorption process. Cryogenic systems are also employed in this field, involving lower operating costs, despite for biomethane production, i.e. removal of carbon dioxide compounds as well. Hence, the present work focuses on the design of an innovative cryogenics-based biogas cleaning system for contaminants removal only, avoiding the usage of chemicals or biological agents.

The starting conditions are based on a previous work where a proper thermodynamic model describing the binary system  $\text{CH}_4\text{-CO}_2$  was developed. These data allow to explore different scenarios, aiming to the optimal one. The analysis is focused on the P-x diagram at three different temperature:  $-100\text{ }^\circ\text{C}$ ,  $-90\text{ }^\circ\text{C}$  and  $-80\text{ }^\circ\text{C}$  (based on a deep literature analysis on cryogenic system and agreed with the company). With these working conditions, a general system design is performed, under certain assumptions. Results were useful for Biokomp company, the project partner responsible for the cryogenic unit design, to have a clear picture of the overall system behaviour to be installed.

Results exhibit that cooling down the biogas at  $-80\text{ }^\circ\text{C}$ , working in a pressure range between 1 bara and 2 bara, no solid formation ( $\text{CO}_2$ ) is observed. Such results set the basis for the analysis of the system working at these operating conditions, thus reaching the complete system sizing. Finally, a proper heat exchanger is chosen, whose sizing is carried as well as its cost evaluation.

The final scenario aims to demonstrate the feasibility of cryogenic contaminants removal for biogas-fed SOFC system. Results proved that, using a plate-fin heat exchanger, the required thermodynamic conditions are achieved, ensuring low capital costs regarding heat exchangers and the overall system as well. Furthermore, no carbon filters or chemical agents are used, as is it foreseen for traditional desulphurization systems, where the contaminants removal is achieved by electricity consumption only.

# TABLE OF CONTENTS

---

LIST OF FIGURES .....	4
LIST OF TABLES .....	7
<b>1 INTRODUCTION.....</b>	<b>1</b>
1.1 Traditional biogas cleaning technologies .....	2
1.1.1 Physico-chemical process .....	2
1.1.2 Biological process.....	4
1.2 Cryogenic biogas upgrading.....	5
1.2.1 Cryogenic system combined with carbon capture.....	6
1.2.2 Cryogenic packed bed.....	8
1.2.3 Cryo pur system .....	9
1.2.4 CryoCell® separation system .....	10
1.2.5 Pioneer cryogenic siloxane removal.....	11
1.3 Cryogenic system for biogas purification .....	13
1.3.1 System description.....	13
1.4 Yokozeky thermodynamic model .....	15
<b>2 CRYOGENIC SYSTEM DESIGN.....</b>	<b>19</b>
2.1 Compressor .....	20
2.2 Dehumidification section .....	22
2.3 Economizer .....	23
2.4 Cryogenic heat exchanger .....	24
2.4.1 CO <sub>2</sub> frosting percentage .....	24
2.4.2 Thermodynamic behaviour .....	26
2.5 Heat transfer areas .....	28
2.5.1 ε-NTU method .....	29
2.5.2 LMTD method .....	30
2.5.3 Heat transfer area for cryogenic applications.....	31
<b>3 RESULTS.....</b>	<b>35</b>
3.1 P-x phase diagrams for CH <sub>4</sub> – CO <sub>2</sub> mixture .....	35

3.2	Properties evaluation.....	38
3.2.1	Specific heat evaluation.....	38
3.2.2	Other properties .....	41
3.3	Complete system analysis.....	42
3.3.1	Compressor .....	45
3.3.2	Economizer .....	46
3.3.3	Cryogenic heat exchanger .....	48
3.4	Heat transfer surface .....	51
<b>4</b>	<b>OPTIMAL OPERATING CONDITIONS .....</b>	<b>58</b>
4.1	System sizing.....	58
4.2	Heat exchanger design.....	61
4.3	Economic analysis .....	71
4.3.1	Investment cost .....	71
4.3.2	Operating cost .....	75
<b>5</b>	<b>CONCLUSIONS .....</b>	<b>78</b>
	<b>REFERENCES.....</b>	<b>80</b>

## LIST OF FIGURES

---

Figure 1 – Schematic flow of the THIOPAQ O&G desulphurisation technology, produced by Paqell company [7]. .....	5
Figure 2 - Flash liquefaction system flow diagram for biogas upgrading combined with carbon capture [9]......	6
Figure 3 - Schematic of liquefaction combined with de-sublimation process for biogas upgrading [9]. .....	7
Figure 4 - Schematic flow diagram for a typical distillation system [9]. .....	7
Figure 5 - Cryogenic packed-bed process schematic for biogas purification [10]. .....	8
Figure 6 - Schematic of Cryo Pur process for liquid biomethane production and pure liquid CO <sub>2</sub> [11]. .....	9
Figure 7 - Process flow diagram for a CryoCell plant, in low carbon dioxide/rich natural gas configuration [12]......	10
Figure 8 – Pioneer DCR system for siloxane removal [13]. .....	12
Figure 9 – Location of the installation site, in the area of Vilnius, Lithuania. ....	13
Figure 10 - 3D system layout, including the Stirling engine, compressor and the heat exchanger (HE) container. ....	14
Figure 11 – Scheme of the Stirling engine used for the production of liquid Nitrogen, used as refrigerant fluid in the cryogenic process [14]......	15
Figure 12 - P-x diagram at T = -100 °C for the binary mixture CH <sub>4</sub> -CO <sub>2</sub> [15]. .....	18
Figure 13 - Process flow diagram for the cryogenic system designed by Biokomp.....	19
Figure 14 - Part of the P&I diagram of the whole system, representing the dehumidification section. ....	22
Figure 15 - Economizer flow scheme, showing inlet and outlet streams. ....	23
Figure 16 - Cryogenic heat exchanger schematic flow, highlighting inlet and outlet streams. ..	24
Figure 17 – Example of lever rule applied on the P-x phase diagram for the binary mixture of CH <sub>4</sub> -CO <sub>2</sub> . .....	25
Figure 18 - SPC-1 cooling power curve [35]. .....	26
Figure 19 - Physical effects that should be considered compared to design effectiveness [19].	31
Figure 20 - Schematic of the CRYO-HX modelling for heat transfer surface estimation. ....	33
Figure 21 - P-x phase diagram for CH <sub>4</sub> -CO <sub>2</sub> mixture, obtained at -80 °C, where only S-SV and V-SV lines are drawn.....	35
Figure 22 - P-x diagram for the binary mixture CH <sub>4</sub> -CO <sub>2</sub> , at -100 °C, where only S-SV and V-SV lines are drawn.....	36

Figure 23 - P-x diagram for the binary CH <sub>4</sub> -CO <sub>2</sub> mixture at -90 °C, where only S-SV and V-SV lines are drawn. ....	36
Figure 24 - Comparison between the three V-SV equilibrium curves.....	37
Figure 25 – Specific heat capacity of CO <sub>2</sub> as temperature varies, with the fitting coefficient and the goodness of fitting values. ....	39
Figure 26 - CH <sub>4</sub> specific heat as function of temperature, with the fitting curve, as well as fitting coefficients and goodness of results. ....	40
Figure 27 – N <sub>2</sub> specific heat as function of temperature, with the fitting curve, as well as fitting coefficients and goodness of results. ....	41
Figure 28 - Excel spreadsheet for the calculus carried for this analysis.....	43
Figure 29 – Biogas mass flow rate behaviour as function of pressure, in the three different scenarios. ....	44
Figure 30 - Compression power at the different operating conditions analysed. ....	46
Figure 31 - ECO-HX downstream temperature, at the different operating conditions considered. ....	47
Figure 32 - Economizer thermal power exchanged, at different operating conditions.....	47
Figure 33 - Dependence between thermal power exchanged within economizer and biogas flow rate. ....	48
Figure 34 - Excel spreadsheet employed to estimate the heat transfer areas of ECO-HX and CRYO-HX (method 1) components. ....	51
Figure 35 – Part of the Excel spreadsheet exploited to compute method 2 in the estimation of CRYO-HX area. ....	52
Figure 36 - Temperature evolution within the CRYO-HX component, used to as check for the second method. ....	53
Figure 37 - ECO-HX heat transfer areas, for scenarios 1 and 2. ....	53
Figure 38 - Heat transfer areas for the third scenario, ECO-HX component. ....	54
Figure 39 – CO <sub>2</sub> frosting point at different pressure conditions. ....	55
Figure 40 - Trend of the estimation error with respect to CO <sub>2</sub> solid mass fraction.....	57
Figure 41 – Biogas density as a function of temperature, at a fixed pressure.....	59
Figure 42 - Different heat exchanger type for cryogenic applications.....	61
Figure 43 - BV brazed heat exchanger schematic flow arrangement and plate configuration [36]. ....	62
Figure 44 - Pacetti BV95 brazed heat exchanger, geometry scheme. ....	63
Figure 45 - Dynamic viscosity of CO <sub>2</sub> as temperature varies, at different pressures [21].....	66

Figure 46 - Dynamic viscosity of methane as a function of both temperature and pressure [21].  
..... 67

Figure 47 - Stainless steel 316L thermal conductivity trend as function of temperature, with the equation describing the curve behaviour, together with  $R^2$ ..... 67

Figure 48 – Capital costs for the two system configurations; within the cleaning unit are summarized different equipment costs: for the cryogenic solution, it includes HEs, Stirling engine and chiller components. While, for the desulphurization system, the cleaning unit groups both desulphurization and dehumidification systems. .... 75

Figure 49 – OPEX comparison between the two system configurations. .... 77

## LIST OF TABLES

---

Table 1 - Comparison between the cryogenic technologies already described, mentioning pros and cons [12].	11
Table 2 – Definition of each stream of the system to be analysed.	19
Table 3 - Definition of each component.	20
Table 4 - Mass fraction of CO <sub>2</sub> frosted at different thermodynamic conditions.	37
Table 5 – CO <sub>2</sub> specific heat at the required temperatures.	39
Table 6 – CH <sub>4</sub> specific heat at the temperatures considered.	40
Table 7 – Biogas Specific heat at the required temperatures.	40
Table 8 – Specific heat of Nitrogen at temperatures of interests.	41
Table 9 - Cooling power provided by the Stirling engine, in the three different scenarios considered.	43
Table 10 – Results for the biogas mass flow rate in the three different scenarios.	44
Table 11 - Compressor results, including the discharge temperature, as well as the work of compression.	45
Table 12 - CRYO-HX results obtained for scenario 1, for a downstream temperature of -80 °C.	48
Table 13 - CRYO-HX results for scenario 2, when biogas is brought up to -90 °C.	49
Table 14 – CRYO-HX results in the third scenario, for a downstream temperature of -100 °C.	49
Table 15 – Results for the N <sub>2</sub> stream, used as refrigerant fluid.	50
Table 16 - Comparison between the two methods developed for the CRYO-HX area estimation, scenario 1.	55
Table 17 - Comparison between the two methods applied for the CRYO-HX area estimation, scenario 2.	56
Table 18 - Comparison between the two methods applied for the CRYO-HX area estimation, scenario 3.	56
Table 19 - Stream temperature results for the final scenario analysed.	59
Table 20 – Biogas flow rate in the different system streams, both mass and volume rate are presented.	60
Table 21 - Thermal power exchanged in each system component.	60
Table 22 - Pacetti BV 95 heat exchanger geometrical data.	63
Table 23 - Pacetti BV 95 heat exchanger other features, i.e. operating conditions and material composition.	64
Table 24 – Mean fluid temperatures at which properties are estimated and surface temperature.	68

Table 25 - Thermophysical properties for biogas stream within the ECO-HX. ....	68
Table 26 – Thermophysical properties for both biogas an N <sub>2</sub> stream within CRYO-HX.....	69
Table 27 – Dimensionless numbers and convective heat transfer coefficient results for CRYO-HX and ECO-HX. ....	69
Table 28 - Stainless steel 316L thermal conductivity results. ....	69
Table 29 - Overall heat transfer coefficient of both ECO-HX and CRYO-HX.....	69
Table 30 - Heat exchangers final dimensions.....	70
Table 31 - Capital cost estimation for CRYO-HX and ECO-HX. ....	72
Table 32 - Capital costs for the cryogenic system.....	73
Table 34 - Capital costs for a traditional desulphurization system.....	74
Table 33 - Electrical consumption of the cryogenic cleaning unit. ....	76
Table 35 - Electrical consumption of a traditional desulphurization system.....	76
Table 36 - Chemical agent costs for a traditional desulphurization system. ....	77

# 1 INTRODUCTION

---

The energy transition from fossil fuels to renewable energy sources is becoming more widespread and greater efforts are made in order to counteract the climate changes our planet is undergoing. The European project *Waste2Watts* aims to this, where eleven partners are cooperating in “*the design and engineer of an integrated biogas-Solid Oxide Fuel Cell combined heat and power system with minimal gas pre-processing, focusing on low-cost biogas pollutant removal and optimal thermal system integration*” [1]. Among the participating partners, the Polytechnic of Turin is collaborating with the Italian company *Biokomp*, whose purpose is to design and construct an innovative biogas purification system based on cryogenics and make it suitable for the fuel cell gas pre-processing.

As it is known, biogas is produced from the anaerobic digestion of organic waste. It is constituted mainly by methane  $\text{CH}_4$  (50-70 vol %), carbon dioxide  $\text{CO}_2$  (25-45 vol %) and other contaminants such as  $\text{H}_2\text{S}$ ,  $\text{H}_2\text{O}$  and siloxanes. The amount and species of contaminants depend on different factors, such as the stage of the decomposition process, temperature, pressure and the age and type of waste treated, and thus on the source from where biogas is produced. These sources can be:

- Landfill waste.
- Organic Fraction of Municipal Solid Waste (OFMSW).
- Agriculture waste (manure, crops).
- Sludge from *Waste Water Treatment Plant (WWTP)*.

The impurities can cause the degradation of the cell performances and overall system durability. The most harmful contaminants for SOFC applications are hydrogen sulphide ( $\text{H}_2\text{S}$ ), Volatile Organic Compounds (VOCs) and siloxanes. Other impurities such as alkanes, halogenated hydrocarbons and other VOCs can be neglected since they represent a minor danger than the substance mentioned above.

$\text{H}_2\text{S}$  compounds, if they are adsorbed on the active site of the tri-phase boundary (TPB), can impede the fuel oxidation at the anode side of the SOFC. Indeed,  $\text{H}_2\text{S}$  poisons the Nickel catalyst, promoting its migration and thus compromising the percolating nickel network, reducing the anode electrical conductivity [2]. This kind of compound is produced during the anaerobic digestion, which quantity depends on the feedstock treated: for instance, sludge in the WWTP contains a larger amount of hydrogen sulphide compared to that carried by the biogas produced from landfill waste.

Siloxanes are compound belonging to silicones, whose molecular structure can be linear, named with letter L, or cyclic, named with D; the letter is followed by a number, indicating the number of Si atoms in the molecule. They have Si-O bonds, where the atom of Si is linked with other functional organic groups, such as methyl and ethyl. Siloxane compounds are found in cosmetics and soaps (in general in silicon-based cosmetics) and are produced by the digestion of sewage sludge in WWTP, where a large amount of cyclic siloxane is found, in particular the type D4 and D5. They can cause irreversible damage on the cell, due to the Si deposition on the interconnector forming an insulating layer, which in turns let the ohmic resistance increase. It has been observed that a concentration of 10 ppm of D5 can cause a rapid failure of the SOFC performances, even within hours [3].

Hence, the necessity to remove this kind of compounds is crucial for SOFC lifetime, and a proper gas pre-processing system has to be employed to avoid performances degradation. In literature, some limit values have been found: 1 ppm concerning the H<sub>2</sub>S and few ppb for siloxanes. It will follow a series of technologies whose aim is to remove mainly sulphur compound.

## 1.1 TRADITIONAL BIOGAS CLEANING TECHNOLOGIES

Several techniques are used to remove contaminants from raw biogas, in order to increase its calorific value and thus producing a gas that can be exploited as a fuel. The main processes commercially available for biogas upgrading will be illustrated in this chapter. Furthermore, cryogenic systems already in commerce will be presented, even though most of them are employed in the biomethane production, and thus in the removal of CO<sub>2</sub>. In biogas-SOFC system, CO<sub>2</sub> removal is not required since it is exploited for both dry and steam reforming process. Thus, it is useless to spent energy for its removal. Hence, technologies such as amines-based process, PSA (pressure swing adsorption) and water scrubbing are not of interest for the purpose of this work. Here, H<sub>2</sub>S, siloxanes and VOCs removal technologies will be illustrated.

### 1.1.1 Physico-chemical process

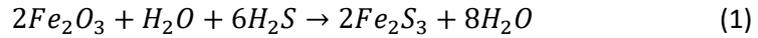
First, a distinction should be made between absorption and adsorption: the first is a volume-related phenomenon, while adsorption is meant for processes where the contaminant is kept on the adsorbing material surface.

- **Absorption processes**

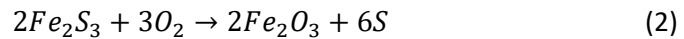
Absorption-based processes can be further divided into solid and liquid absorption.

- *Solid absorption* is mainly focused on the use of metal oxides, such as ZnO, Cu doped with ZnO/SiO<sub>2</sub>, iron oxide. *Desotec* company [4] performs H<sub>2</sub>S removal with iron

oxide, also called iron sponge process, that consists of wood chips impregnated with hydrate iron oxide. This kind of process is applied to gases containing a low amount of hydrogen sulphide, < 300 ppm, and it follows the reaction showed by Eq. (1).



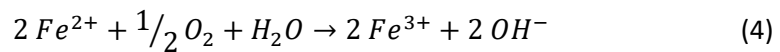
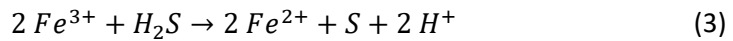
Iron sulphide is then removed from the system by adding air, and it can be re-oxidized to iron oxide and elemental sulphur, as the exothermic reaction in equation (2) states.



The greater advantage of using iron oxide in gas cleaning small-scale biogas power systems is that it can be easily regenerated at low temperature and it can operate at ambient temperature.

- *Liquid sorption*

- \* *Fe-chelated solution*: it involves the use of the redox reaction illustrated by equations (3) and (4).

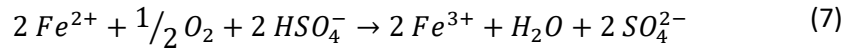
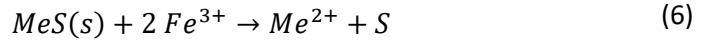


*AirScience* company [5] offers a desulphurization system based on this concept, the *Ferrachel II*<sup>®</sup> iron chelate process, suitable for high H<sub>2</sub>S concentration. The system, operating at ambient temperature and atmospheric pressure, is composed of three towers where biogas is sent; in the first, the H<sub>2</sub>S rich biogas interacts with the Fe-chelate solution absorbing the contaminant particles. Then, the spent solution is regenerated producing elemental sulphur, that is then separated by filtration. Such a process can reduce the biogas H<sub>2</sub>S content to less than 100 ppm; hence, a further cleaning process is required to bring its concentration to values below 2 ppm.

On the other hand, this kind of process is complex to be applied to a small-scale SOFC application.

- \* *Metal sulphate solution*: the principal reaction involved in this process are listed below in equations (5), (6), (7), (8).





For small scale application, due to the limit of an operating temperature above 60 °C and to the complexity of generating acids as H<sub>2</sub>SO<sub>4</sub>, it is difficult to realize.

- **Adsorption processes**

Adsorption processes have been demonstrated that are very effective in H<sub>2</sub>S, siloxane and mercaptans removal. Adsorption is a phenomenon in which the contaminants are kept on the surface of an adsorbing material, that could be activated carbon, zeolites or carbon molecular sieves. Activated carbon is the most adsorbent used so far, which are obtained through thermal processes, pyrolysis or gasification, involving amorphous carbon materials. Via this process, a microporous structure is obtained, with a high internal surface area. Activated carbons commercially available have been proved to effectively remove H<sub>2</sub>S and siloxane compounds up to SOFC limits, i.e. < 1 ppm. Furthermore, its adsorption capacity can be improved by impregnating the activated carbon with solid or liquid chemicals [6].

In general, involves high operating costs due to the materials disposal, unless they are regenerated, which, however, is currently hardly pursued on the market.

### 1.1.2 Biological process

This kind of processes do not involve chemical agents, instead, micro-organisms are exploited. Biological technologies are capable to remove simultaneously hydrogen sulphide, mercaptans and siloxane. One of the most used technologies employing biological process is the *bio-trickling filter*, which is considered as a valid alternative to chemical scrubbers. The gas is passed through a packed inert bed, where micro-organism lays and capture contaminants. Such a technology is able to achieve an H<sub>2</sub>S removal efficiency of above 70%, and some laboratory tests experienced that the presence of mercaptans can enhance bioreactor performance, leading to a reduction of sulphur accumulation within the reactor. Hence, bio-trickling filters are suitable for biogas-SOFC applications as contaminants removal, but it would require a further cleaning system to bring H<sub>2</sub>S concentration up to SOFC limits.

An industrial system, already in commerce, is *THIOPAQ O&G* desulphurisation technology, produced by *Paqell* company [7]. In Figure 3 a schematic of the process layout is shown.

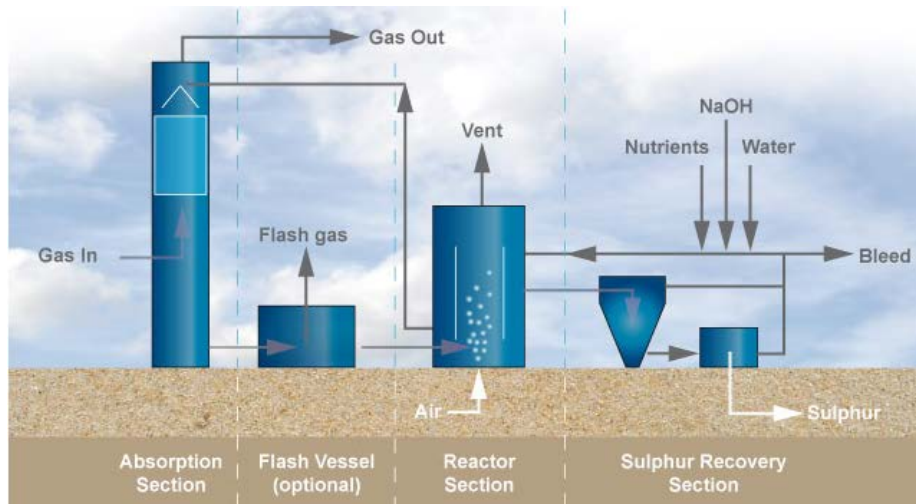


Figure 1 – Schematic flow of the THIOPAQ O&G desulphurisation technology, produced by Paqell company [7].

In such a process, gas purification is integrated with sulphur removal in a single unit. The  $H_2S$  rich gas is passed through the contactor, in the absorption section, where it gets in contact and absorbed by a wildy alkaline sodium hydroxide solution, forming sodium sulphides. The clean gas exits the contactor from the top. Subsequently, depending on the feed gas pressure, the solution is passed through a flash vessel or directly into the bioreactor, which operates at atmospheric conditions and ambient temperature. Here, a controlled amount of air is introduced to facilitate bacteria growth, which oxidizes sulphide ions to elemental sulphur. The sodium solution is then recirculated into the absorber, thus minimizing chemicals consumptions in the absorption section. On the other hand, the sulphur-rich solution is pumped to the sulphur recovery section, where sulphur is separated from the solution by a decanter centrifuge. Such a system does not remove contaminants up to SOFC tolerated limits, requiring thus an additional cleaning system to match the required impurity levels[6], [7].

## 1.2 CRYOGENIC BIOGAS UPGRADING

More attention is being paid to cryogenic process for contaminants removal. Indeed, Hofmann et al [8], in his article, studied a cryogenic process to produce liquefied biomethane. In this paper, he claimed that at 193 K (-80 °C) the biogas is free of  $H_2O$ ,  $H_2S$  and  $NH_3$  residual content. Hence, it is possible to condense contaminants decreasing the temperature up to cryogenic level, i.e. at a temperature below -50 °C.

However, most of the cryogenic process available on the market are employed on biomethane production, thus cleaning the biogas from all the contaminant and  $CO_2$  as well, aiming to obtain a pure  $CH_4$  gas or liquid stream. A brief presentation of some of such technologies will be illustrated in this paragraph, mentioning which companies employ their efforts in this field.



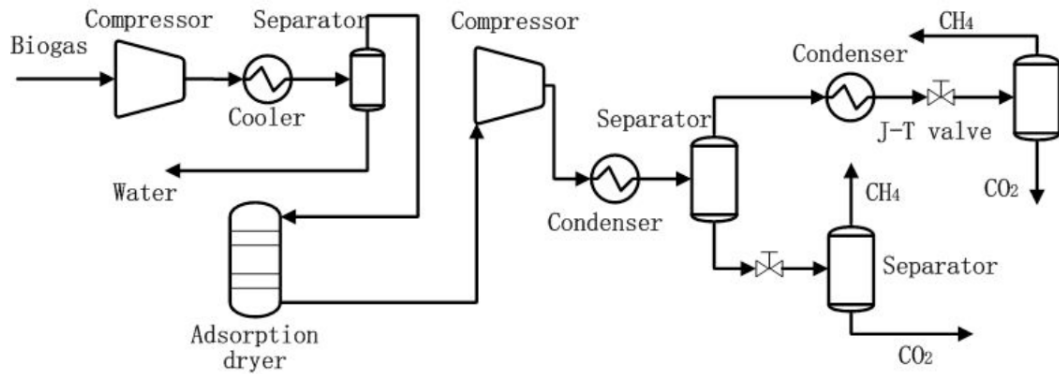


Figure 3 - Schematic of liquefaction combined with de-sublimation process for biogas upgrading [9].

Studies have reported that, in such a system, compressing the biogas at 80 bar allows to obtain a CH<sub>4</sub> purity above 97 %.

*Distillation process* is the most common technique adopted for cryogenic biogas upgrading. In this kind of process, CO<sub>2</sub> is separated from methane by liquefaction. A schematic of the process is presented in Figure 4.

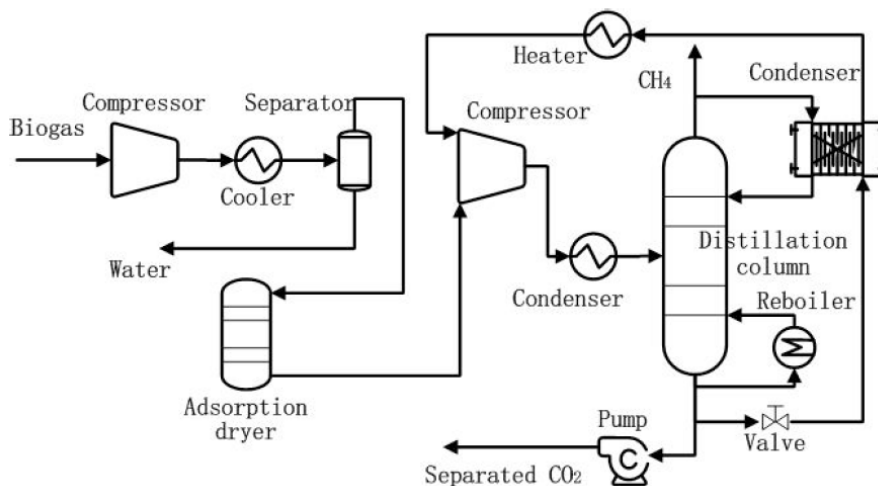


Figure 4 - Schematic flow diagram for a typical distillation system [9].

The feed biogas is first compressed (18-30 bar) and cooled down to -45/-60 °C, in order to remove moisture content and to liquefy other gaseous impurities, except for carbon dioxide, which sublimation is avoided thanks to high pressure. Then, it is compressed and cooled down again, feeding thus the central part of the distillation column. At the top of the reactor, vapour products are partially condensed; the liquid part turns back into the column, while CH<sub>4</sub> in the vapour phase is collected. So, the liquid CO<sub>2</sub> is heated up by the fed biogas, in the middle of the column, hence further separating CH<sub>4</sub>. With this such a system, a purity of 94.5% and 99.7% can be reached for CH<sub>4</sub> and CO<sub>2</sub>, respectively [9].

### 1.2.2 Cryogenic packed bed

A novel technology in cryogenic biogas upgrading field is the use of dynamically operated packed bed, which were originally developed for CO<sub>2</sub> capture from flue gas, and then applied to other uses, such as biogas upgrading. The process can be basically divided into three steps:

- Cooling step: the packed bed is cooled down to -120 °C, in order to sublimate or condensate contaminants, such as CO<sub>2</sub> and water.
- Capture step: biogas is fed to the previously cooled packing bed, where carbon dioxide starts to desublimates while leaving other substances, such as methane and nitrogen, in the gaseous phase flowing through the bed.
- Recovery step: once the bed is saturated, it is switched to the recovery mode. For biogas application, Nitrogen or air could be injected. Due to the presence of methane, injecting air could cause the formation of the mixture CH<sub>4</sub>/O<sub>2</sub> that is within the explosion limits. To avoid this, first N<sub>2</sub> is injected removing thus CH<sub>4</sub> from the bed, and then air can be flushed to remove other contaminants. Normally, during this phase, when flue gas feeds the packing bed, gaseous CO<sub>2</sub> is injected, allowing to obtain pure CO<sub>2</sub> at the outlet (for CO<sub>2</sub> capture purpose).

A schematic of the process is shown in Figure 5.

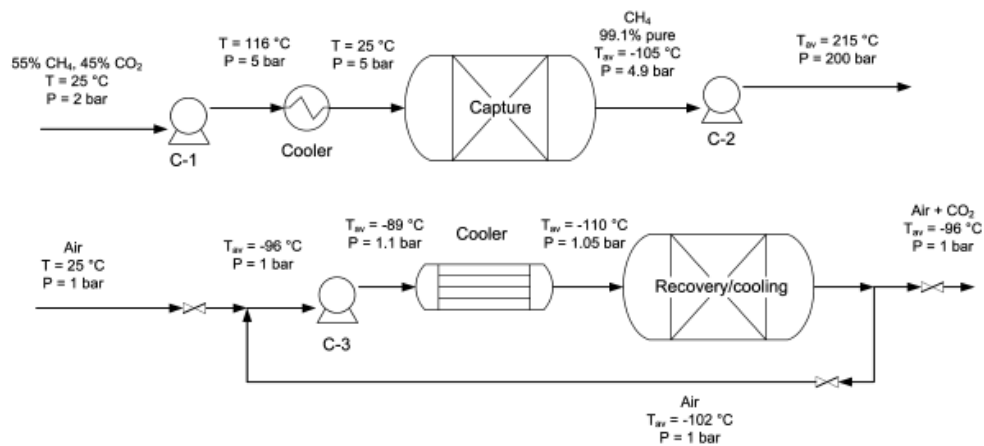


Figure 5 - Cryogenic packed-bed process schematic for biogas purification [10].

Three compressors are needed: the first to bring the biogas to 5 bar (C1), the second one (C2) to pressurize the produced methane to 200 bar, and the third (C3) is used flush air into the cooler and the bed. It has been experimentally proved that cooling down the bed at -110 °C and pressurizing the feeding gas, CH<sub>4</sub> purity at the outlet of the process reaches the value of 99.1 %, as illustrated in Figure 5 [10].

### 1.2.3 Cryo pur system

Cryo Pur company [11] has developed an innovative technology that transforms biogas, produced from organic waste, into liquid biomethane, also known as bioLNG, and into liquid CO<sub>2</sub> for industrial applications. Such a system offers the opportunity to produce biomethane from farmers, operators of WWTP, landfill operators or food processing companies. A schematic of such a process is shown in Figure 6.

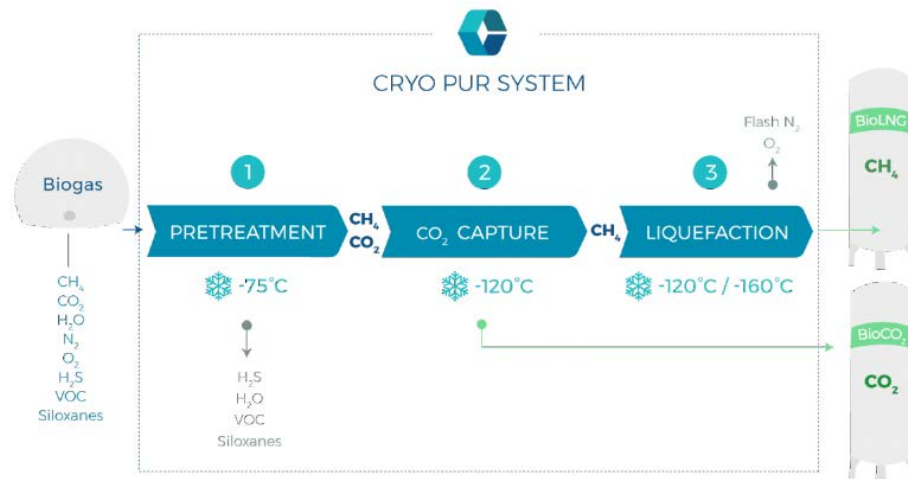


Figure 6 - Schematic of Cryo Pur process for liquid biomethane production and pure liquid CO<sub>2</sub> [11].

Three main steps are identified:

- Biogas pre-treatment: the feed gas is cleaned from its impurities, such as H<sub>2</sub>s, VOCs and siloxanes. First, it is passed through an activated carbon filter, where hydrogen sulphide is removed. Then, VOCs and siloxanes together with water are removed by two dehumidification steps: first, the gas is cooled down up to -40 °C, by means of two heat exchangers, alternating water frosting and defrosting phases; in the second dehumidification step, similar to the first, biogas is cooled to -75 °C.
- Carbon capture: here, two heat exchangers are used to frost and defrost the CO<sub>2</sub>, bringing the biogas to a temperature of -120 °C. During this phase, CO<sub>2</sub> is recovered as liquid phase so that it can be directly exploited as a product.
- Biomethane liquefaction: biomethane is compressed to 15 bar and liquefied at -120 °C, which can be finally stored in a cryogenic vessel. Furthermore, biomethane can be liquefied at 2 bar and -160 °C through a boil-off and a re-liquefaction process.

These different steps are all integrated into a unique system, with the consequent minimization in electricity consumption. In addition, Cryo Pur system allows recovering thermal energy from the refrigerant system, which is, in turn, exploited to meet the digester heating request upstream the system.

#### 1.2.4 CryoCell® separation system

Another cryogenic solution for contaminants removal is *CryoCell*® separation. Its working principle is based on cooling the gas feed to the freezing point of carbon dioxide; part of such a stream is condensed and then expanded in a Joule-Thomson valve, ensuring the separation of the liquid, solid and gas phase. Subsequently, in a separator the separation of the phases occurs, ensuring a gas stream with low carbon concentration, while the denser phases with high CO<sub>2</sub> concentration. Finally, Carbon dioxide is melted and mixed with the liquid phase, so that it can be removed from the system. *CryoCell*® plant can be exploited in different configurations, in order to meet specific conditions. In Figure 7, a flow diagram of the process is presented [12].

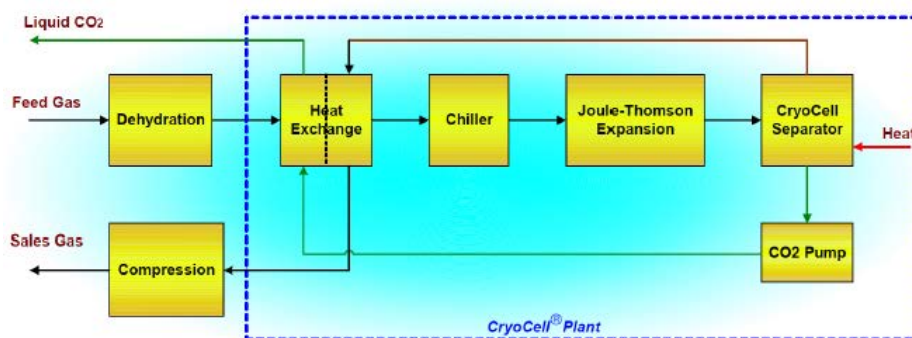


Figure 7 - Process flow diagram for a CryoCell plant, in low carbon dioxide/rich natural gas configuration [12].

A comparative table of the different technologies already described is listed in Table 1, where also advantages and disadvantages are illustrated. In the mentioned table, concerning processes described in section 1.2.1, just the distillation is reported, representing the most used among the three presented.

Table 1 - Comparison between the cryogenic technologies already described, mentioning pros and cons [12].

Technology	Pros	Cons
<b>Cryogenic distillation</b>	<ul style="list-style-type: none"> <li>• Low CH<sub>4</sub> losses</li> <li>• works well for high CO<sub>2</sub> content</li> <li>• CH<sub>4</sub> and CO<sub>2</sub> purity between 94.5 % and 99.7 %.</li> </ul>	<ul style="list-style-type: none"> <li>• More expensive than traditional upgrading technologies.</li> <li>• Possible solid formation in the distillation column at different pressure</li> <li>• Not suitable for diluted CO<sub>2</sub> streams</li> </ul>
<b>Cryogenic packed-bed</b>	<ul style="list-style-type: none"> <li>• Low CH<sub>4</sub> losses</li> </ul>	<ul style="list-style-type: none"> <li>• More expensive than traditional biogas upgrading technologies.</li> <li>• Possibility of blockage during operation.</li> </ul>
<b>Cryo Pur system</b>	<ul style="list-style-type: none"> <li>• Low methane losses, Easily scalable and high heat recovery</li> <li>• Integrates biogas upgrading, biomethane liquefaction and cryogenic distillation column</li> <li>• Liquid methane and CO<sub>2</sub> purity of 99%</li> </ul>	<ul style="list-style-type: none"> <li>• More expensive than traditional upgrading technologies</li> <li>• Not domestic, but suitable for large gas flows at high concentrations</li> <li>• Energy-intensive and high maintenance costs</li> </ul>
<b>CryoCell® separation</b>	<ul style="list-style-type: none"> <li>• Low CH<sub>4</sub> losses</li> <li>• Multiple configurations for different types of gas streams</li> <li>• No foaming or corrosion potential</li> <li>• Scalable</li> </ul>	<ul style="list-style-type: none"> <li>• More expensive than traditional upgrading technologies</li> <li>• High maintenance costs</li> </ul>

### 1.2.5 Pioneer cryogenic siloxane removal

*Pioneer Air Systems* U.S. company [13] focuses on the design of high-quality biogas treatment, air drying, gas cleaning and process chilling equipment. Until now, it is the only company that performs biogas-contaminants removal through cryogenic technique. Their DCR (Deep Chilling Removal) system, aims at the removal of siloxane from digestion-produced biogas. Its peculiarity is that no media is used. Indeed, as was previously explained, in a media-based siloxane removal system the media can be saturated of contaminants and could be replaced, if it is a consumable media, or regenerated. In the first case, the saturated media can be classified as hazardous when it comes in contact with landfill or digester gas, thus requiring proper method for its disposal. On the other hand, the regeneratable media is heated up, so that regeneration takes place, and the gas is sent to a flare for disposal. However, experiences noticed that the regeneration never reached 100% efficiency, so that the material has to be replaced.

Deep Chilling Removal system either no media is used, and emission discharge does not require the thermal oxidation to remove captured contaminants. Siloxanes and VOCs are removed from the system through the aqueous discharge, which could be returned to the digester or filtered and thus returned to the landfill-leachate system. Such a system is able to remove 96-97% of siloxane content in the feed gas. With a single treatment, an inlet siloxane level of 1000 ppm can be reduced up to 30 ppm. Hence, for SOFC application, a further cleaning system may be installed, such as a small carbon polishing bed. In Figure 8, a scheme of the system is provided.

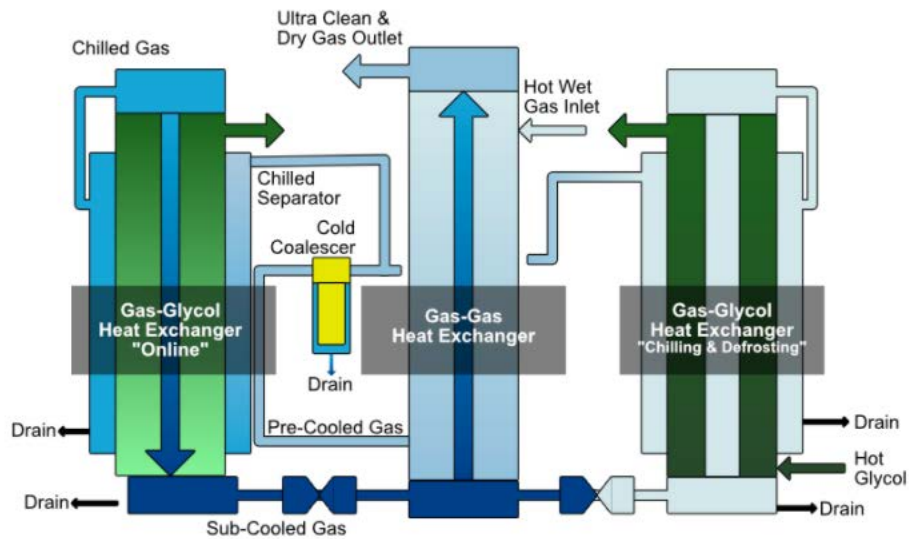


Figure 8 – Pioneer DCR system for siloxane removal [13].

### 1.3 CRYOGENIC SYSTEM FOR BIOGAS PURIFICATION

The system to be designed aims to remove pollutants from the biogas produced from the anaerobic digestion of the Organic Fraction of Municipal Solid Waste (OFMSW), that will be used to produce electricity throughout a Solid Oxide Fuel Cell (SOFC) plant. The same unit can be used also in other biogas production sites, like generic organic waste treatments, large farms, landfill sites and wastewater treatment plants.

The system will be constructed at Biokomp premises and installed in a farm, named *UAB Cestos Maistas*, located in the area of Vilnius, Lithuania. The farm includes both the animal section and the slaughterhouse section. In Figure 9, the installation site and location are shown.



Figure 9 – Location of the installation site, in the area of Vilnius, Lithuania.

The plant is already producing biogas from agriculture and slaughterhouse wastes. The necessity of biogas cleaning is due to the presence of a large amount of hydrogen sulphide ( $H_2S$ ), siloxanes and other impurities that are not tolerated by the fuel cell. Because of that, an innovative cryogenic system for contaminants removal is being studied and will be described as follows.

#### 1.3.1 System description

The system starts with a compressor, that allows to vary the pressure at the desired value. The pressure range in which the system will operate is  $1 \text{ bar} < p < 5 \text{ bar}$  (absolute pressure). Subsequently, the biogas has to be taken to very low temperatures, so that water and contaminants (especially  $H_2S$ ) separation can occur. First, a dehumidifier is encountered, whose purpose is to remove as much water as possible. The dehumidification system consists of a gas/chilled water heat exchanger, where the refrigerant is produced via chiller.

Then, biogas is brought to the operating conditions through two heat exchangers: the one which works at lower temperatures interfaces with the refrigerant produced by the Stirling engine, used in reverse cycle. On the other hand, the intermediate heat exchanger provides the biogas pre-cooling with the vapour fraction outgoing the cryogenic heat exchanger. At the end of the process, a filter of activated carbon is installed, in order to remove any residual contaminants.

Furthermore, a periodic defrosting for the exchanger is foreseen, due to the accumulation of a certain mass of contaminant on the heat exchanger surface. These contaminants are mainly water, carbon dioxide and other pollutants (such as hydrogen sulphide, mercaptans, siloxanes, and so on). In figure 23, it is shown a 3D of the container where such a system will be installed.



Figure 10 - 3D system layout, including the Stirling engine, compressor and the heat exchanger (HE) container.

It can be noticed all the components listed above: the compressor, the Stirling engine and a box containing the two heat exchangers (HE).

The cryogenic heat exchanger works at low temperature, around  $-80\text{ }^{\circ}\text{C}/-100\text{ }^{\circ}\text{C}$ . Stirling engine is found to be a suitable technology to get these thermal levels. Such equipment, provided by *Stirling Cryogenics* company, is exploited in the reverse cycle, whose aim is to liquefy Nitrogen, which is employed as refrigerant fluid. In Figure 11, a scheme of the system is illustrated.

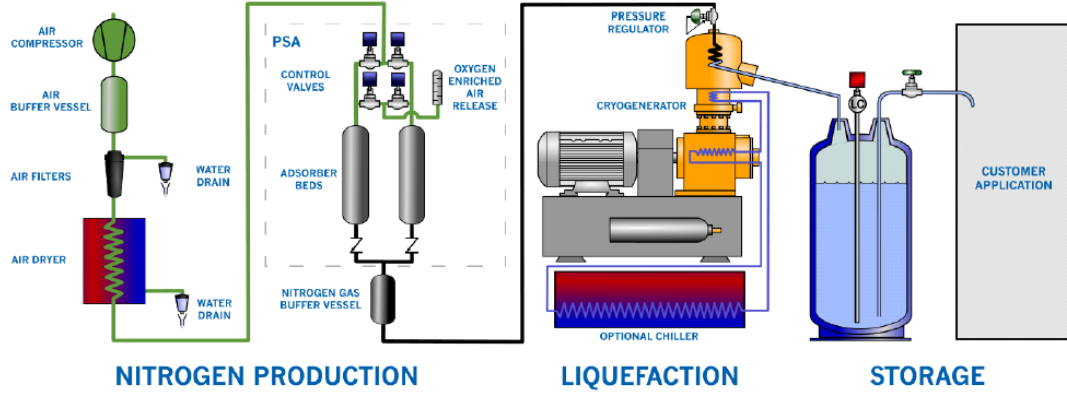


Figure 11 – Scheme of the Stirling engine used for the production of liquid Nitrogen, used as refrigerant fluid in the cryogenic process [14].

Ambient air is compressed, filtered and dried, in order to remove moisture and particles, and thus sent through *Pressure Swing Adsorption* (PSA) unit. Two carbon-based adsorbing bed, working alternatively, are exploited to remove oxygen from the air stream so that pure nitrogen gas is obtained. Two control valve regulates the air flowing into the adsorber beds: once the first adsorber bed is oxygen-saturated, the valve switch over the second bed so that the first can be regenerated by releasing the oxygen-enriched air into the atmosphere. The continuous switching ensures a constant purified nitrogen stream. Finally, liquid nitrogen is obtained into the *cryogenerator*, throughout a Stirling cycle, which then flows by the effect of gravity into a storage vessel linked to the customer cooling load [14].

#### 1.4 YOKOZEKY THERMODYNAMIC MODEL

The present work sets its basis on what has previously done by Falco Federico [15], who made a literature research to find a thermodynamic model suitable for the phase diagram construction of the binary system  $\text{CH}_4\text{-CO}_2$ . The model he used is the Yokozeky one, which is a modified version of the Wan der Walls equation of state, able to represent both fluid and solid phases. The Yokozeky proposed EoS is presented in eq. (9):

$$P = \frac{R \cdot T}{V - b} \cdot \frac{(V - d)^k}{(V - c)^k} - \frac{a}{V^2 + qbV + rb^2} \quad (9)$$

where  $P$  is the pressure,  $T$  the temperature,  $R$  the gas constant,  $c$  the liquid covolume,  $b$  the solid covolume,  $a$  the attractive term,  $d$ ,  $q$ ,  $r$  and  $k$  are constant parameters. The just mentioned equation needs to fulfil two requirements:

$$b < d < c$$

$$k \in \mathbb{N}, \quad k \geq 1$$

The case analysed by Yokozeki, on which the work [15] is based, is the simpler, with  $k = 1$ ,  $q = r = 0$ . Substituting these conditions to the Eq. (9), the SLV-EoS becomes as Eq. (10) states.

$$P = \frac{R \cdot T}{V - b} \cdot \frac{(V - d)^k}{(V - c)^k} - \frac{a}{V^2} \quad (10)$$

Furthermore, Yokozeki found that parameters  $a$  and  $b$  are temperature-dependent functions, expressed by equations (11) and (12).

$$a(T) = \frac{(R T_c)^2}{P_c} [a_0 + a_1 T_r \exp(-a_2 T_r^n)] \quad (11)$$

$$b(T) = V_c [a_0 + a_1 T_r \exp(-a_2 T_r^m)] \quad (12)$$

For applying this model to single component systems, a reduced form can be exploited, where parameters  $b$ ,  $c$  and  $d$  are normalized with respect to the critical volume. Moreover, the pressure, volume, temperature, and the compressibility factor  $Z$  are reduced by using their critical values, i.e. the value they assume in critical conditions. On the other hand, to make parameter  $a$  dimensionless, is obtained as equation (13) shows.

$$a_r = \frac{P_r \cdot a}{(R T_c)^2} \quad (13)$$

The subscript  $r$  states for the reduced form of each parameter. Hence, substituting in the equation of state and explicating in terms of the compressibility factor, equation (14) is obtained.

$$Z = \frac{V_r}{V_r - b_r} \cdot \frac{V_r - d_r}{V_r - c_r} - \frac{a_r}{V_r \cdot Z_c \cdot T_r} \quad (14)$$

The parameters set up is widely discussed in the work [15].

To draw the phase diagram for the single component, there is the necessity to compute the three phase equilibria: Solid-Vapor Equilibrium (SVE), Solid-Liquid Equilibrium (SLE) and Vapor-Liquid Equilibrium (VLE). The condition to be verified for the system to be in a phase equilibrium is the *isofugacity*. The fugacity is the pressure that hypothetically an ideal gas should have for its molar Gibbs free energy to be equal to the equivalent real gas. As it is reported in the Yokozeki article [16], the fugacity coefficient  $\phi$  can be computed by Eq. (15).

$$\ln(\phi) = Z - 1 - \ln(Z) - \int_{\infty}^{V_r} \frac{Z - 1}{V_r} dV_r = Z - 1 - \ln(Z) - I_1 \quad (15)$$

In the single component phase diagram, each phase equilibrium occurs when one of the following conditions is verified:

- If the equality  $\phi_s \cdot x_s = \phi_l \cdot x_l$  is verified, the Solid-Liquid equilibrium (SLE) occurs.
- If the equality  $\phi_s \cdot x_s = \phi_v \cdot x_v$  is verified, the Solid-Vapor equilibrium (SVE) occurs.
- If the equality  $\phi_v \cdot x_v = \phi_l \cdot x_l$  is verified, the Vapor-Liquid equilibrium (VLE) occurs.

The terms  $x$  stands for the molar fractions of the phase considered, identified by the subscripts  $s, l, v$  representing the solid, liquid and vapor phase, respectively. It is clear that all the three conditions need to be verified at the triple point, that is the Solid-Liquid-Vapor (SLV) equilibrium. The latter can be obtained by the solution of equation (16), retrieved by imposing the *Maxwell's equal area* condition between two phases  $\alpha$  and  $\beta$ .

$$P_{r,t}(V_\alpha - V_\beta) = \frac{a_r}{Z_c^2} \left( \frac{1}{V_\alpha} - \frac{1}{V_\beta} \right) + \frac{T_{r,t}}{Z_c (b_r - c_r)} \cdot \left[ b_r \ln \left( \frac{V_\alpha - b_r}{V_\beta - b_r} \right) - c_r \ln \left| \frac{V_\alpha - c_r}{V_\beta - c_r} \right| + d_r \ln \left( \frac{V_\alpha - b_r}{V_\beta - b_r} \cdot \left| \frac{V_\alpha - c_r}{V_\beta - c_r} \right| \right) \right] \quad (16)$$

Considering the binary system CH<sub>4</sub>-CO<sub>2</sub>, the equation of state exploited is the non-reduced form (10). Parameters  $a, b, c$  and  $d$  are modelled by exploiting the *Van der Waals/Lorentz-Berthelot* mixing rule, whose expression are reported by equations (17), (18), (19) and (20), being  $N$  the number of components.

$$a = \sum_{i,j=1}^N \sqrt{a_i \cdot a_j} \cdot (1 - k_{ij}) \cdot x_i x_j \quad (17)$$

$$b = \sum_{i=1}^N b_i x_i \quad (18)$$

$$c = \sum_{i=1}^N c_i x_i \quad (19)$$

$$d = \sum_{i=1}^N d_i x_i \quad (20)$$

Where the parameter  $k_{ij}$  is called *binary interaction parameter*, which is estimated to be included in a range between 0.09 and 0.15, according to [16].

Finally, equation (21) is used to evaluate the fugacity coefficient for the  $i$ -th species in the  $N$  component mixture.

$$\phi_i = \frac{1}{b-c} \left[ c \ln \left| 1 - \frac{c}{V} \right| - b \ln \left( 1 - \frac{b}{V} \right) \right] - \frac{c_i(b-d) + b_i(d-c) + (b-c)(d-d_i)}{(b-c)^2} - \frac{1}{b-c} \left[ \frac{c_i(c-d)}{V-c} + \frac{b_i(d-b)}{V-b} \right] - \frac{2 \sum_{j=1}^N \sqrt{a_i \cdot a_j} \cdot (1 - k_{ij}) \cdot x_j}{V R T} \quad (21)$$

The procedure just illustrated, with other considerations that are demanded to the mentioned works [15],[16], allowed to draw the phase diagram for the binary mixture CH<sub>4</sub>-CO<sub>2</sub>. Particular attention is paid on the P-x diagram (pressure-concentration), in order to estimate the maximum working pressure avoiding liquid phase formation. In Figure 12, the P-x diagram at -100 °C, obtained as a result in [15] is shown.

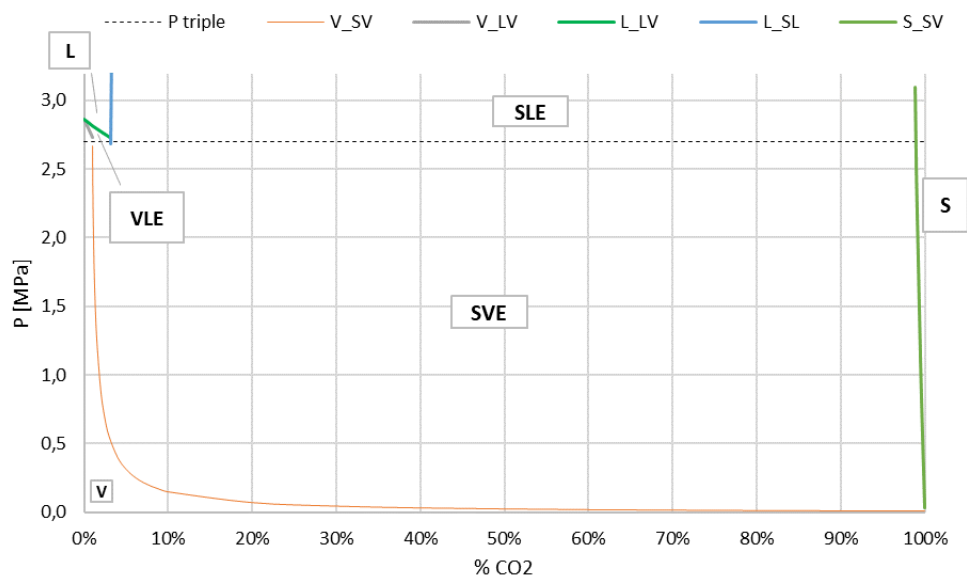


Figure 12 - P-x diagram at  $T = -100 \text{ }^\circ\text{C}$  for the binary mixture CH<sub>4</sub>-CO<sub>2</sub> [15].

## 2 CRYOGENIC SYSTEM DESIGN

The system to be analysed is the one described in section 1.3.1. The main idea is to clean biogas feeding the fuel cell through cryogenics. This is achieved by two thermal steps, through which biogas is brought to a temperature such that undesired contaminants condensate.

A process flow scheme is illustrated in Figure 13, in order to set each stream name as well as each component.

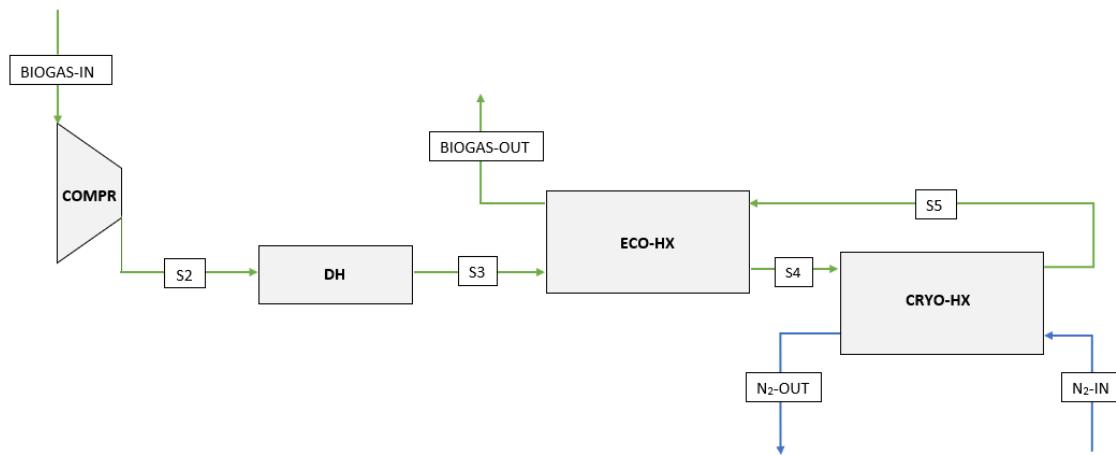


Figure 13 - Process flow diagram for the cryogenic system designed by Biokomp.

In Table 2 each stream is defined, while Table 3 lists each component name.

Table 2 – Definition of each stream of the system to be analysed.

Stream	Description
<b>BIOGAS – IN</b>	Biogas entering the system.
<b>S2</b>	Compressed biogas feeding the dehumidification section.
<b>S3</b>	Dehumidified biogas stream.
<b>S4</b>	Cryogenic heat exchanger inlet, where biogas is supposed to be cleaned by undesired contaminants.
<b>S5</b>	Biogas vapor phase used to make a thermal recovery within the economizer.
<b>BIOGAS – OUT</b>	Heated clean biogas ready for usage.
<b>N<sub>2</sub> – IN</b>	Inlet Nitrogen stream, used as a refrigerant to perform cryogenics.
<b>N<sub>2</sub> – OUT</b>	Outlet of the refrigerant fluid, N <sub>2</sub> .

Table 3 - Definition of each component.

<b>Component</b>	<b>Description.</b>
<b>COMPR</b>	Compressor.
<b>DH</b>	Dehumidification section.
<b>ECO – HX</b>	Economizer, first thermal step.
<b>CRYO – HX</b>	Cryogenic heat exchanger, second thermal step.

Once the system streams and components are defined, it is possible to start the sizing of the system. Due to the complexity of the argument treated, initially no trustworthy results were achieved modelling through Aspen plus®, because the software was not able to properly model the phase transition Vapor-Solid within the cryogenic heat exchanger. Because of that, an excel model is instead developed, in order to manually estimate and understand the behaviour of the system under specific operating conditions. For the calculus that will follows, a minimum  $\Delta T$  is imposed, equal to 10 °C.

The main focus is on the cryogenic part, where the hardest computational part lays. Within this area, some interesting results are achieved.

## 2.1 COMPRESSOR

The compressor is the first component, whose aim is to compress the biogas entering the system. The transformation that biogas undergoes within the component has been modelled as adiabatic, i.e. no heat exchange with the external environment is considered. The isentropic compression is described by the Poisson equation, represented by Eq. (22), where  $\gamma$  is the adiabatic coefficient.

$$p \cdot V^\gamma = const \quad (22)$$

The input data are:

- Inlet temperature,  $T_{biogas,in}$ , equal to 25 °C.
- Compression ratio,  $\beta$ , given by the ratio between the absolute discharge pressure and the absolute suction pressure.
- Suction pressure,  $p_1$ , equal to 1 bar.
- Isentropic efficiency,  $\eta_{is}$ , assumed to a value of 0.8.
- Gas constant  $R^*$ , whose value is evaluated through the procedure illustrated in section 3.2. Its value is 305.66 J/kg/K.
- Laplace's coefficient  $\gamma$ , whose value is estimated through the procedure described in section 3.2.2, however found to be equal to 1.3.

Using the ideal gases law, the Eq. (22) can be rewritten in terms of pressure and temperature, as Eq. (23) states.

$$T \cdot p^{\frac{1-\gamma}{\gamma}} = const \quad (23)$$

Therefore, using this expression, between BIOGAS-IN and S2 streams, it is possible to evaluate the ideal outlet temperature  $T_{2,id}$ , as shown in Eq. (24).

$$T_1 \cdot p_1^{\frac{1-\gamma}{\gamma}} = T_{2,id} \cdot p_2^{\frac{1-\gamma}{\gamma}}$$

$$T_{2,id} = T_1 \cdot \left(\frac{p_2}{p_1}\right)^{\frac{(\gamma-1)}{\gamma}} \quad (24)$$

Where subscript 1 identifies the BIOGAS-In stream. Then, assuming an isentropic efficiency for the compressor of 0.8, it is possible to retrieve the real outlet temperature, obtained inverting the Eq. (25) for the isotropic efficiency, obtaining thus Eq. (26).

$$\eta_{is} = \frac{T_{2,id} - T_1}{T_2 - T_1} \quad (25)$$

$$T_2 = T_1 + \frac{T_{2,id} - T_1}{\eta_{is}} \quad (26)$$

Once the outlet temperature is evaluated, knowing the biogas mass flowrate and its specific heat (whose evaluation are explained in section 3.2.1), it is also possible to estimate the work needed to compress the gas at the desired pressure. It is retrieved starting from the first Law of thermodynamic, written for an adiabatic system, as Eq. (27) states.

$$\Delta U = -L \quad (27)$$

Eq. (27) tells that the work exchanged with the external environment is equal to the variation of the internal energy of the system. Therefore, the work of compression can be evaluated by solving the integral between state 1 and 2, corresponding to streams BIOGAS-IN and S2, and then substituting the pressure with the ratio obtained by inverting Eq. (22).

$$L = \int_1^2 p dV = const \int_1^2 \frac{dV}{V^\gamma} = const \left[ \frac{V^{1-\gamma}}{1-\gamma} \right]_1^2 = \left[ \frac{p V}{1-\gamma} \right]_1^2 = \frac{p_2 V_2 - p_1 V_1}{1-\gamma}$$

The solution to the above integral provides the final work formula, as stated in Eq. (28).

$$L = \frac{R^* T}{1-\gamma} \left[ \beta^{\frac{\gamma-1}{\gamma}} - 1 \right] \quad (28)$$

The equation written in this form, gives a negative result, since the work of compression is provided to the system. Finally, multiplying the Eq. (28) by the mass flow rate, the power needed to compress the biogas is obtained.

## 2.2 DEHUMIDIFICATION SECTION

Originally, another heat exchanger was foreseen conversely to the dehumidifier. This is because, at this stage of the process, moisture content has to be removed from the biogas stream. It was planned a heat exchanger performing thermal recovery with the biogas vapor fraction outgoing the cryogenic heat exchanger. In this way, energy consumption was supposed to be minimized, although it required bigger capital costs for heat exchangers realizations.

Dehumidification is set to obtain an out-flow of biogas at a temperature of 5 °C; since it consists in a dedicated bundle of components, no modelling will be discussed for this part but only the outlet temperature will be taken into account since useful for the rest of the analysis. This step is performed via chiller, ensuring hence the moisture removal from biogas mixture. However, such component involves electricity consumption, whose nominal value is estimated to be around 15 kW.

In Figure 14, a schematic of the dehumidification section is given, taken from the P&I (piping and instrumentations) diagram realized by Biokomp company.

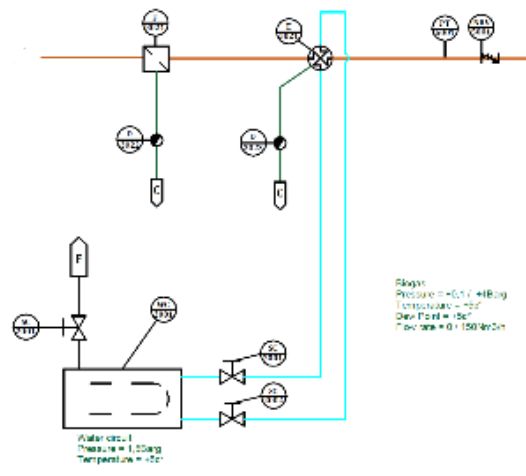


Figure 14 - Part of the P&I diagram of the whole system, representing the dehumidification section.

## 2.3 ECONOMIZER

The economizer is the component that has to cool the biogas as much as possible. It exploits the outgoing vapor phase from the cryogenic heat exchanger to pre-cool the feeding biogas, such that energy consumption is minimized for a fixed flow rate, or to maximize treated biogas flow, given fixed energy consumption. In Figure 15 it is shown such system section.

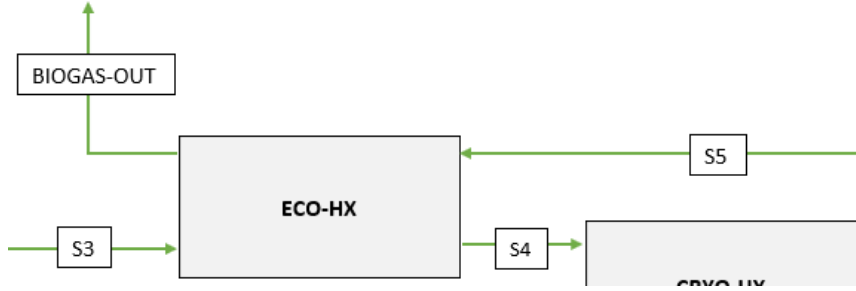


Figure 15 - Economizer flow scheme, showing inlet and outlet streams.

The input data are:

- Hot side inlet temperature,  $T_3$ , corresponding to the DH outlet stream (S3).
- Cold-side inlet temperature,  $T_5$ , corresponding to stream (S5).
- Biogas flow rate for both cold and hot side, retrieved in the cryogenic section.
- Specific heat of both cold and hot side evaluated at the inlet temperatures (whose values are evaluated through the procedure illustrated in section 3.2.1).

Therefore, the hot outlet temperature  $T_4$  and the outlet cold-side temperature  $T_{biogas,out}$  are the only unknown of the system. Temperature differences must respect the constraint of the minimum  $\Delta T$  allowed; consequently, stream BIOGAS-OUT temperature is evaluated as expressed by Eq. (29).

$$T_{biogas,out} = T_3 - \Delta T_{min} \quad (29)$$

As done for the heat exchanger, the unknown temperature can be estimated, by setting the heat exchanged on both cold and hot side as equal (Eq. (30)). Then expanding the expressions and re-writing in terms of  $T_4$ , Eq. (31) is retrieved.

$$\phi_{hot} = \phi_{cold} \quad (30)$$

$$T_4 = T_3 - \frac{(\dot{m} c)_{cold}}{(\dot{m} c)_{hot}} \cdot (T_{biogas,out} - T_5) \quad (31)$$

Finally, the total amount of heat exchanged is evaluated through Eq. (32), where the First Law of Thermodynamic is exploited. This quantity can be estimated indifferently on both cold and hot

side because the evaluation of temperature  $T_4$  ensures the equality of the thermal heat exchanged within the component (Eq. (30)).

$$\phi_{eco} = (\dot{m} c_p)_{hot} \cdot (T_3 - T_4) \quad (32)$$

## 2.4 CRYOGENIC HEAT EXCHANGER

This part was the longest and hardest to model, due to few data available on such topic. Thanks to the previous work carried by [15], where the Yokozeky thermodynamic model is applied to draw some phase diagrams concerning the binary mixture  $\text{CH}_4\text{-CO}_2$ , it has been possible to extract some useful data, i.e. the  $\text{CO}_2$  frosting percentage. Then, along with *Biokomp* company, it has been established some pressure and temperature limits that the system has to use as thresholds, i.e. where the separation should take place effectively. The mentioned conditions are:

- Pressure range:  $0 \text{ bar}(g) < p < 5 \text{ bar}(g)$ .
- Temperature range:  $-80 \text{ }^\circ\text{C} < T < -100 \text{ }^\circ\text{C}$ .

Considering these thermodynamic conditions, three P-x (pressure-composition) phase diagrams are retrieved, exploiting the Yokozeky model, at  $-80 \text{ }^\circ\text{C}$ ,  $-90 \text{ }^\circ\text{C}$  and  $-100 \text{ }^\circ\text{C}$ , each of them falling into the pressure range considered. In Figure 16 the schematic flow diagram of such section is exhibited.

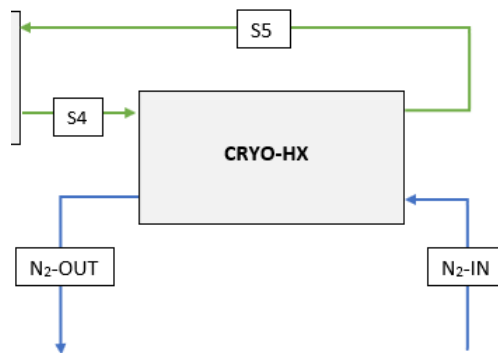


Figure 16 - Cryogenic heat exchanger schematic flow, highlighting inlet and outlet streams.

### 2.4.1 $\text{CO}_2$ frosting percentage

Once the phase diagrams are obtained, in order to establish how much  $\text{CO}_2$  will frost (undesired effect) at different operating conditions, the so-called lever rule has been applied.

The lever rule is used to extract some information from a binary phase diagram. To be more precise, it allows evaluating the mass fraction ( $\omega$ ) of each phase composing the binary

equilibrium of a phase diagram, in this case CH<sub>4</sub>-CO<sub>2</sub> diagram. Considering a generic mixture of two phases,  $\alpha$  and  $\beta$ , composed of two elements  $A$  and  $B$ , the mass fraction of phase  $\alpha$  can be determined throughout Eq. (33).

$$\omega^\alpha = \frac{\omega_B - \omega_B^\beta}{\omega_B^\alpha - \omega_B^\beta} \quad (33)$$

Where  $\omega_B^\alpha$  is the mass fraction of element  $B$  in phase  $\alpha$ ,  $\omega_B^\beta$  is the mass fraction of element  $B$  in phase  $\beta$  and  $\omega_B$  is the mass fraction of element  $B$  in the mixture [17].

Therefore, considering the P-x phase diagram CH<sub>4</sub>-CO<sub>2</sub> at -100 °C, Figure 17, in order to evaluate these parameters a horizontal line is traced at the composition's pressure from one phase to the other, i.e. from the vapor phase to the solid one. The mass fraction of frosting CO<sub>2</sub> will be given by the segment between the equilibrium curve and the CO<sub>2</sub> volume fraction in the mixture, over the length of the segment of the entire SVE region, as shown in Figure 17.

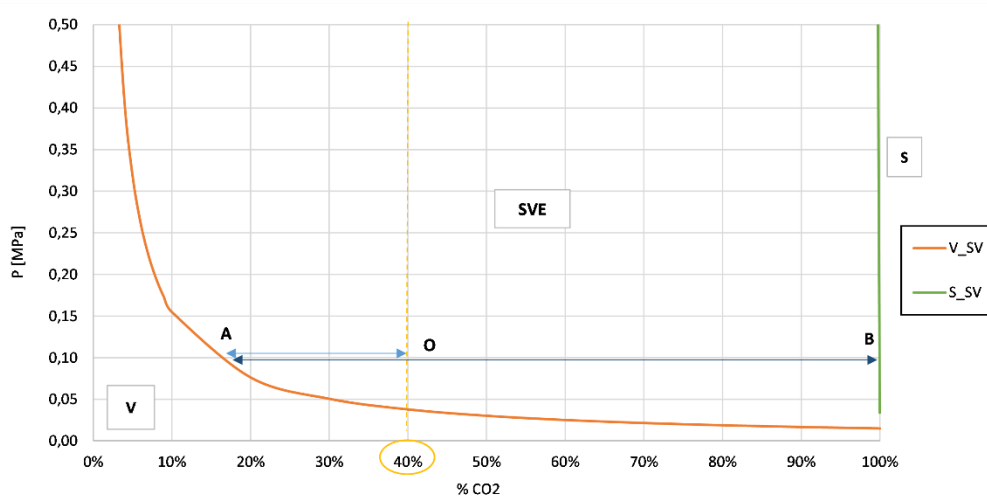


Figure 17 – Example of lever rule applied on the P-x phase diagram for the binary mixture of CH<sub>4</sub>-CO<sub>2</sub>.

Hence, the percentage of CO<sub>2</sub> that frosts at 1 bar and -100 °C will be given by the ratio between segment  $\overline{AO}$ , representing CO<sub>2</sub> solid phase, and segment  $\overline{AB}$ , representing all the SVE region, as eq. (34) states.

$$\%CO_{2_{frost}} = \frac{\overline{AO}}{\overline{AB}} \quad (34)$$

This procedure is applied to all the phase diagrams produced so that a clear behaviour of the binary mixture can be traced. Furthermore, such procedure allowed to set the basis of the working conditions for the whole system, due to the fact that frost of CO<sub>2</sub> is an undesired effect.

## 2.4.2 Thermodynamic behaviour

After the CO<sub>2</sub> frosting behaviour is evaluated, a general sizing of the heat exchanger can be achieved. In particular, in this section, the focus will be put on the evaluation of the biogas mass flow rate that the system can treat, due to the fixed operating conditions on the Stirling engine side.

First, the SPC-1 cooling power curve is exploited, showed in Figure 18, in order to estimate the overall heat that can be transferred to the biogas flowing within the exchanger. The “cold” produced by the Stirling engine is represented by the pink curve, named as “Gross cooling power”. Subsequently, a hypothetical efficiency of 0.9 between the value retrieved from the curve and what is effectively transferred to the biogas is set, hence obtaining the effective cooling power that is transferred. Concerning Figure 18, on the x-axis is found the Stirling engine outlet temperature, coinciding to that entering the cold-side of the cryogenic heat exchanger (stream N<sub>2</sub>-in). Such value is evaluated considering a temperature difference of 20 °C with the outlet biogas flow from the cryogenic heat exchanger, whose value is initially set by the P-x phase diagram.

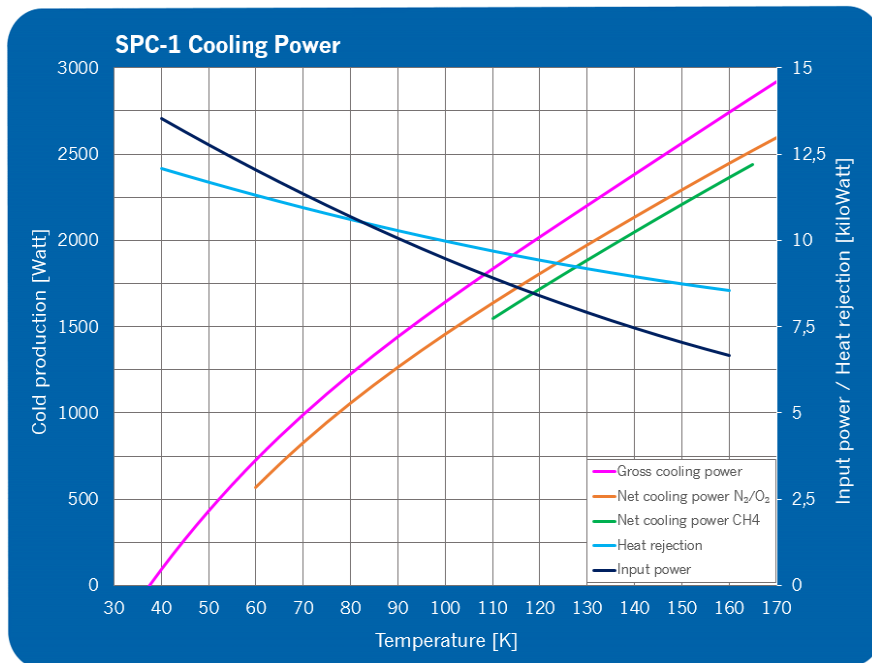


Figure 18 - SPC-1 cooling power curve [35].

At this stage, the input data are:

- Hot-side inlet temperature  $T_4$ , retrieved by Eq. (31).
- Hot-side outlet temperature  $T_5$ , known from the phase diagrams.
- Cold-side inlet temperature  $T_{N_2,in}$ , obtained imposing a difference of 20 °C with  $T_5$ .
- CO<sub>2</sub> solid mass fraction evaluated in section 2.4.1.

- Overall heat supplied from SPC-1 cryogenerator.

Once data are set, the amount of biogas that the system can treat is then estimated, exploiting the excel function “goal seek”. The procedure is illustrated as follows:

- Fix an initial value for the biogas flow rate.
- Knowing the mass fraction of frosting CO<sub>2</sub> ( $\%CO_{2frost}$ ), the vapour and solid flow are evaluated as Eq. (35) and (36) shows.

$$\dot{m}_{frost} = \dot{m}_{gas} \cdot \%CO_{2frost} \quad (35)$$

$$\dot{m}_{vap} = \dot{m}_{gas} - \dot{m}_{frost} \quad (36)$$

- Knowing the specific heat and the latent heat of sublimation ( $L_{hs}$ ), whose values are evaluated through the procedure showed in 3.2.1, the amount of latent heat and sensible heat can be evaluated as Eq. (37) and (38) state, respectively.

$$\phi_{lat} = \dot{m}_{frost} \cdot L_{hs} \quad (37)$$

$$\phi_{sens} = \dot{m}_{vap} \cdot c_p \cdot (T_{in} - T_{out}) \quad (38)$$

Being the sublimation of CO<sub>2</sub> an exothermic process, the amount of heat released during the phase transition has to be removed by the refrigerant fluid [18]. Hence, the overall heat transferred will be given by the sum of these two quantities, as shown in Eq. (39).

$$\phi_{th} = \phi_{sens} + \phi_{lat} \quad (39)$$

- Finally, the Excel goal seek function can be exploited. Setting the overall heat exchanged (Eq. (39)) equal to the value retrieved from the Stirling curve, the biogas flow rate is varied until a match is found.

On the other hand, the cryogenic heat exchanger cold-side is modelled fixing a  $\Delta T$  both downstream and upstream the exchanger. Concerning the outlet temperature  $T_{N_2,out}$ , it has been evaluated imposing a  $\Delta T$  with  $T_4$  equal to 10 °C. Conversely, specific heat for Nitrogen flow is evaluated in section 3.2.1 as well, assumed constant over the whole heat exchanger surface. Finally, N<sub>2</sub> mass flow is retrieved from the First law for a closed system, as Eq. (40) states.

$$G_{N_2} = \frac{\phi_{th}}{c_{p,N_2} \cdot (T_{N_2,out} - T_{N_2,in})} \quad (40)$$

Where  $\phi_{th}$  is the amount of heat retrieved from the curve in Figure 18,  $c_{p,N_2}$  is the specific heat of the refrigerant fluid evaluated at the inlet temperature  $T_{N_2,in}$ .

## 2.5 HEAT TRANSFER AREAS

At this stage of the analysis, it is necessary to estimate the heat exchangers areas, in order to establish the feasibility of implementing a system with these operating conditions.

The sizing of a heat exchanger is done by performing a thermal design calculation and then the verification.

- The thermal design calculation aims to evaluate the heat exchanger area required to realize the desired heat transfer between two fluids, knowing their mass flow rates, inlet temperatures and at least one outlet temperature. The procedure consists in the selection of a type of heat exchanger, evaluating then the surface required to reach the desired outlet temperature.
- The verification calculation is done on an existing heat exchanger, whose heat transfer area, mass flow rates of the fluids involved, and their upstream temperature are known. The aim is to evaluate downstream temperatures and the thermal power exchanged.

The most used techniques to design a heat exchanger are the LMTD (logarithmic mean temperature difference) method and  $\epsilon$ -NTU method. Both methods belong to the category of *Lumped parameters models* (LPM), which can be used indifferently either to make a design and verification calculation or vice versa. Such models are based on the energy balances showed on Eq. (41) and Eq. (42).

$$C_h dT_h = U dA (T_h - T_c) \quad (41)$$

$$C_c dT_c = U dA (T_h - T_c) \quad (42)$$

Where subscripts  $h$  and  $c$  stand for hot fluid and cold fluid, respectively, while  $C$  is the heat capacity rate, given by the product between the mass flow rate and the specific heat, as Eq. (43) states.

$$C = \dot{m} \cdot c_p \quad (43)$$

The integration of Eq. (41) and (42) is performed under the following assumptions:

- Steady-state conditions.
- Negligible longitudinal heat conduction.
- Adiabatic conditions, i.e. no heat transfer with the surroundings.
- Constant heat capacity and overall heat transfer coefficient.

However, lumped parameters models are suitable for a single-phase flow with constant properties [19]. In this case, to design the economizer the  $\varepsilon$ -NTU method is used and then the LMTD one is exploited in order to perform the verification of the estimated areas.

### 2.5.1 $\varepsilon$ -NTU method

The  $\varepsilon$ -NTU method is based on the definition of an efficiency  $\varepsilon$  for the heat exchanger, given by the ratio of the thermal power actually exchanged  $\phi_t$ , and the maximum thermal power that can be transferred  $\phi_{t_{max}}$ , as shown by Eq. (44).

$$\varepsilon = \frac{\phi_t}{\phi_{t_{max}}} \quad (44)$$

$\phi_{t_{max}}$  represents the maximum achievable thermal power in a counter-current heat exchanger with infinite heat transfer area, where the fluid with the minimum heat capacity rate  $C_{min}$ , i.e. the product given by Eq. (43), undergoes the maximum temperature difference. In other words, the maximum thermal power achievable is reached when the outlet temperature of the fluid showing the minimum heat capacity rate equals the inlet temperature of the one having the maximum heat capacity rate. So, the maximum thermal power can be evaluated through the Eq. (45).

$$\phi_{t_{max}} = C_{min} \cdot (T_{h,in} - T_{c,in}) \quad (45)$$

The minimum thermal capacity, in general, is that of the cold fluid, especially in this analysis, because the mass flow rate of the biogas representing the cold side is lower than the initial flow rate, due to the sublimed CO<sub>2</sub> during the cryogenic heat exchange. Hence, knowing the thermal heat exchanged, the efficiency can be estimated.

Subsequently, the exchanger efficiency can be expressed as a function of two parameters:  $\varepsilon = f(NTU, C)$ , where the term NTU is the so-called *number of transfer units*, given by Eq. (46).

$$NTU = \frac{U \cdot A}{C_{min}} \quad (46)$$

Where  $U$  is the overall heat transfer coefficient  $\left[\frac{W}{m^2K}\right]$ , while the term  $C$  is the ratio of the heat capacity rate of the two fluids, as stated by Eq. (47), and  $A$  is the heat transfer area.

$$C = \frac{C_{min}}{C_{max}} \quad (47)$$

The relationship between these three parameters can be found in literature, where analytical correlations and diagrams are available. To set an Excel spreadsheet, the analytical correlations are preferred. The analytical expression exploited is the one referring to a double pipe counterflow heat exchanger, where the efficiency is related to the  $NTU$  factor and the heat capacity rate ratio by Eq. (48a) and (48b).

$$\varepsilon = \frac{1 - \exp[-NTU(1 - C)]}{1 - C \exp[-NTU(1 - C)]} \quad (C < 1) \quad (48a)$$

$$\varepsilon = \frac{NTU}{1 + NTU} \quad (C = 1) \quad (48b)$$

Hence, referring the Eq. (45a) or (45b) to  $NTU$  term, its value can be computed, as Eq. (49a) and (49b) exhibit.

$$NTU = -\frac{1}{1 - C} \cdot \ln\left(\frac{1 - \varepsilon}{1 - C \cdot \varepsilon}\right) \quad (C < 1) \quad (49a)$$

$$NTU = \frac{\varepsilon}{1 - \varepsilon} \quad (C = 1) \quad (49b)$$

Finally, once the number of transfer units is estimated, the required heat transfer area is computed through Eq. (46), expressed in terms of  $A$  [20].

## 2.5.2 LMTD method

In the logarithmic mean temperature difference (LMTD) method, the thermal power is linked to the temperature difference between the hot and cold fluid. Nevertheless, it is necessary to introduce a new temperature difference opportunely averaged, due to the temperature variation along the exchanger surface. The new temperature difference, called  $\Delta T_{ml}$ , is the logarithmic average between the temperature difference upstream and downstream the heat exchanger. This is valid for those exchangers where the wall conductance does not vary along the exchange surface.

Calling with  $\Delta T_1$  the upstream temperature difference and with  $\Delta T_2$  the downstream temperature difference, for a counter-current heat exchanger configuration, the new quantity  $\Delta T_{ml}$  is given by Eq. (50).

$$\Delta T_{ml} = \frac{\Delta T_1 - \Delta T_2}{\ln\left(\frac{\Delta T_1}{\Delta T_2}\right)} \quad (50)$$

Where  $\Delta T_1$  and  $\Delta T_2$  are given by Eq. (51) and (52).

$$\Delta T_1 = T_{h_{in}} - T_{c_{out}} \quad (51)$$

$$\Delta T_2 = T_{h_{out}} - T_{c_{in}} \quad (52)$$

Therefore, the thermal power exchanged within the component will be given by Eq. (53).

$$\phi_t = U \cdot A \cdot \Delta T_{ml} \quad (53)$$

Thus, comparing the value obtained through Eq. (53) with that retrieved from Figure 18, if there is a match the estimation is correct, otherwise the procedure has to be repeated [20].

### 2.5.3 Heat transfer area for cryogenic applications

Lumped parameter models are not suitable for the sizing of heat exchangers involving very low temperatures. This is because cryogenic heat exchangers require very high efficiencies, thus representing a challenging issue. Indeed, such components work in demanding conditions, involving large temperature differences, multiple streams (as for LNG processes), phase change, multi-component streams. On the other hand, traditional heat exchanger models neglect some physical effect that in high efficiencies processes cannot be, such as fluid properties variation, heat exchange with the surroundings, longitudinal thermal conductivity and flow distribution. As reported in Figure 19, the magnitude of such effects is compared, which can be all neglected for low-efficiency applications.

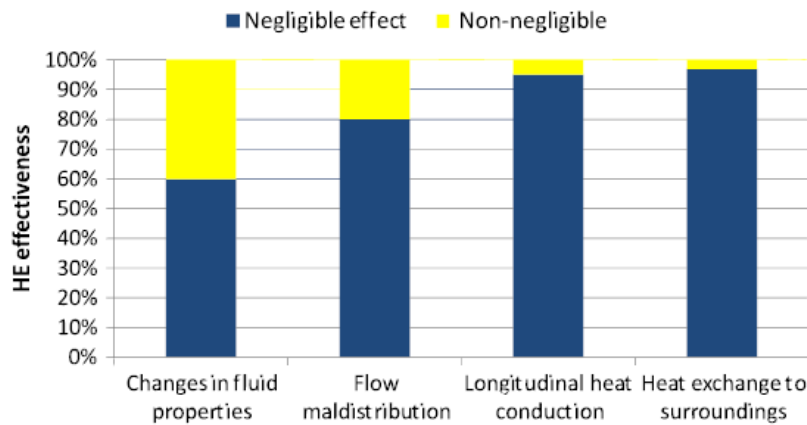


Figure 19 - Physical effects that should be considered compared to design effectiveness [19].

Furthermore, due to the validity of lumped parameters for single-phase flow, they are not suitable for cryogenic applications. To overcome this, another modelling technique can be exploited, i.e. *distributed parameters model* (DPM). Such a method consists in the division of the exchanger into zones or elements of different size, where lumped parameters models can be exploited. In such a way, in each region, LPM assumptions are better fulfilled. This technique is widely used for a different type of application; for instance, condensers and evaporator are

usually modelled by dividing the component into three zones: two regions where only a single-phase is found, and the intermediate one where a two-phase flow occurs. Moreover, it is possible to further divide each zone into elements in a given physical length, in a geometry-oriented approach [19].

In the present study, the geometry of the exchanger is not known a priori, requiring thus a different approach that allows performing a qualitative estimation for the heat transfer area. To this purpose, two methods have been developed, both based on LPM models, and discussed as follows.

- **Method 1**

The procedure consists mainly in the application of LPM over the entire length of the exchanger. First, the  $\epsilon$ -NTU method is applied to estimate the unknown heat transfer area, while the LMTD method is then exploited to check the correctness of the result. The procedure is the same already illustrated in section 2.5.1 and 2.5.2, with some variation. The first is in the assessment of the maximum thermal power achievable  $\phi_{t_{max}}$ , whose expression has to be modified in order to take into account the amount of latent heat released during the phase change, as Eq. (54) states.

$$\phi_{t_{max}} = C_{min} \cdot (T_{h,in} - T_{c,in}) + \phi_{lat} \quad (54)$$

Hence, using Eq. (44), to retrieve the effectiveness of the exchanger, and Eq. (49), to estimate NTU, the heat transfer surface is estimated. Subsequently, through the LMTD method, the logarithmic mean temperature difference is estimated, according to Eq. (50), thus computing the thermal power with a modified version of Eq. (53), i.e. adding the latent heat contribution, as expressed by Eq. (55).

$$\phi_t = U \cdot A_{ths} \cdot \Delta T_{ml} + \phi_{lat} \quad (55)$$

Due to the strong assumption that the phase change occurs within the whole exchanger surface, the estimated area will be that involving sensible heat only. Also, Eq. (55) does not return exactly the thermal power retrieved by the Stirling curve  $\phi_{st}$ , Figure 18. Hence, the error committed is evaluated through Eq. (56).

$$err = \frac{|\phi_t - \phi_{st}|}{\phi_{st}} \quad (56)$$

The quantity evaluated through Eq. (56), is also the error committed in the evaluation of the heat exchanger surface, whose value, accounting also for the latent heat release, will be given by Eq. (57).

$$A_{tot} = A_{ths} + \frac{\phi_{lat}}{U \cdot \Delta T_{ml}} \quad (57)$$

- **Method 2**

In this case, the exchanger is divided into two zones: the first is governed by sensible heat exchange only, while within the second one the phase change occurs, as shown in Figure 20. The two-region interface is identified through the frosting point of CO<sub>2</sub>,  $T_{frost}$ , which is retrieved from its relative phase diagram, given by [15]. In the same figure,  $T_o$  stands for the cold-fluid interface temperature.

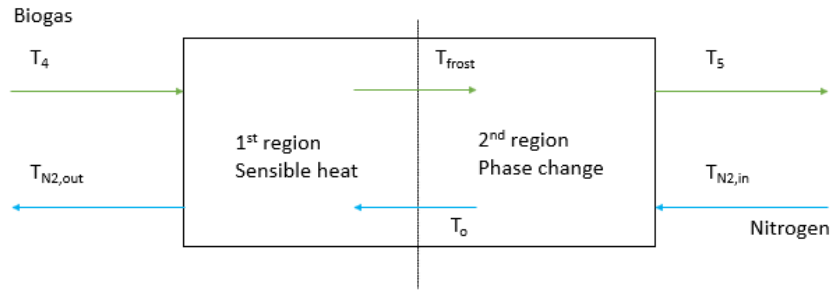


Figure 20 - Schematic of the CRYO-HX modelling for heat transfer surface estimation.

On the basis of the CRYO-HX design, explained in section 2.4, the known data are:

- $T_4$ , hot-side inlet temperature.
- $T_5$ , hot-side outlet temperature.
- $T_{N_2,in}$ , cold-side inlet temperature.
- $T_{frost}$ , retrieved from CO<sub>2</sub> phase diagram by interpolation.

Therefore, the unknowns are  $T_o$  and the CRYO-HX outlet cold-side temperature  $T_{N_2,out}$ . The estimation is carried starting from the second region. Here, the amount of heat exchanged, involving both sensible and latent heat contribution, is evaluated through Eq. (58).

$$\phi_2 = \dot{m}_{h,2} \cdot c_{p_{h,2}} \cdot (T_{frost} - T_5) + \phi_{lat} \quad (58)$$

The subscript 2 states for the second region, while the term  $\dot{m}_{h,2}$  corresponds to the vapor fraction of biogas that does not frost. As consequence, fixing the amount of heat exchanged equal on both cold and hot side, temperature  $T_o$  can be estimated through Eq. (59).

$$T_o = T_7 + \frac{\phi_2}{\dot{m}_{c,2} \cdot c_{p_{c,2}}} \quad (59)$$

The same procedure is followed in the first region, where first the amount of heat exchanged is evaluated  $\phi_1$ , thus obtaining the refrigerant outlet temperature  $T_{N_2,out}$  through Eq. (60).

$$T_{N_2,out} = T_o + \frac{\phi_1}{\dot{m}_{c,1} \cdot c_{p,c,1}} \quad (60)$$

Once all the temperatures are evaluated, the LMTD method is computed in each region separately. Using Eq. (51), (52) and (50), the logarithmic mean temperature difference in both zones is estimated, thus obtaining the heat transfer area by expressing Eq. (53) in term of A. Even in this case, the evaluated quantity will be affected by a certain error, which is estimated through Eq. (56), where  $\phi_t$  is given by the sum of the thermal power exchanged in each region.

Furthermore, other verifications are required. Indeed, in most of the cases, it has been found a violation of the minimum temperature difference imposed (10 °C), in correspondence of the two-region interface. To overcome this issue, a further goal seek analysis is performed: fixing the temperature difference between  $T_{frost}$  and  $T_o$  to the required value (10°C), the refrigerant fluid flow rate is varied, until the condition is fulfilled.

Both methods are thus applied in order to make a qualitative estimation of the heat transfer surface required to realize thermal fluxes involved. It is clear that the second method will be more accurate by dividing the exchanger into more elements, but this was not possible, due to the lack of any geometrical data [19].

### 3 RESULTS

In this section, output results coming from the methodology illustrated in the section 2 will be presented. Different scenarios have been considered, in order to have a clear picture of the whole system behaviour.

Three main scenarios have been analysed, as explained in section 2, that are:

- Scenario 1: biogas brought to temperature  $T_5 = -80^{\circ}\text{C}$ .
- Scenario 2: biogas brought to temperature  $T_5 = -90^{\circ}\text{C}$ .
- Scenario 3: biogas brought to temperature  $T_5 = -100^{\circ}\text{C}$ .

The pressure range considered is between 1 bar and 5 bar (absolute pressure). Starting from these thermodynamic conditions, calculus can be computed.

The biogas volume composition, considered for the analysis, is 60%  $\text{CH}_4$  and 40%  $\text{CO}_2$ , that translated into mass fraction, i.e. considering their densities, are 65%  $\text{CO}_2$  and 35%  $\text{CH}_4$ . Both components are considered as ideal gases, so that the biogas mixture is ideal as well.

#### 3.1 P-X PHASE DIAGRAMS FOR $\text{CH}_4 - \text{CO}_2$ MIXTURE

The first step consists in drawing the phase diagrams at the three different temperature considered. Exploiting the Yokozeky thermodynamic-based model developed by Falco in his master thesis [15], the phase diagrams at the three scenarios conditions are obtained. For the purpose of this work, only the S-SV and V-SV lines are drawn, representing the phase equilibria of interest in the working pressure range chosen. Such phase diagrams are presented in Figure 21, Figure 22 and Figure 23.

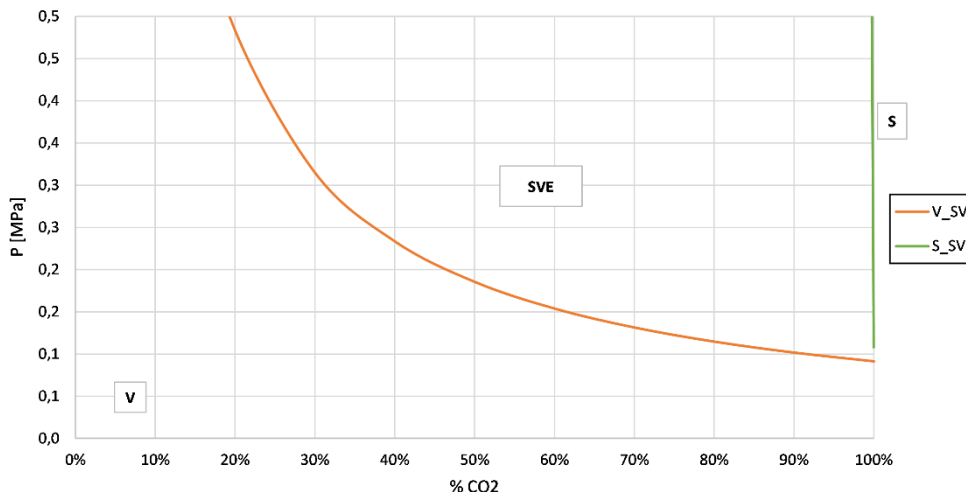


Figure 21 - P-x phase diagram for  $\text{CH}_4\text{-CO}_2$  mixture, obtained at  $-80^{\circ}\text{C}$ , where only S-SV and V-SV lines are drawn.

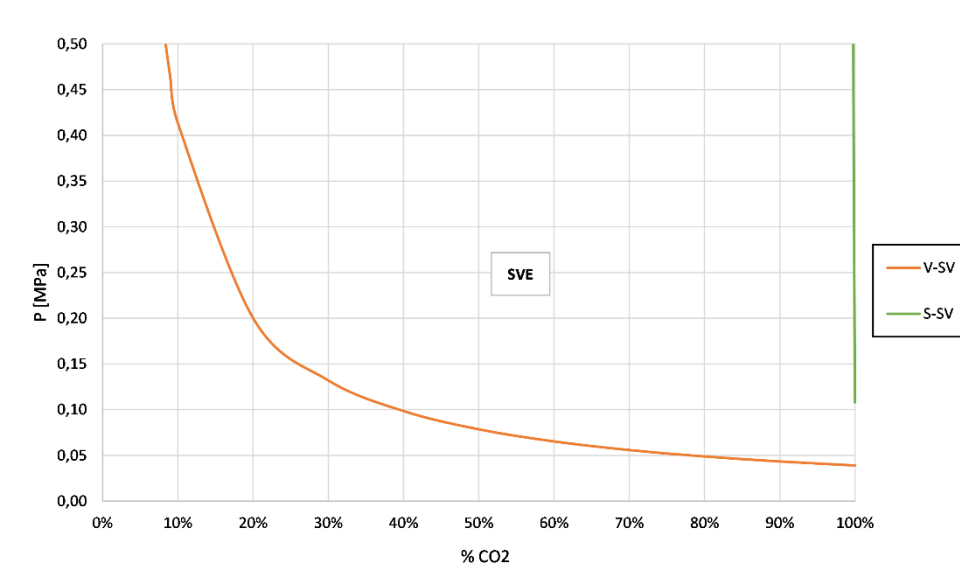


Figure 23 - P-x diagram for the binary  $CH_4$ - $CO_2$  mixture at  $-90$  °C, where only S-SV and V-SV lines are drawn.

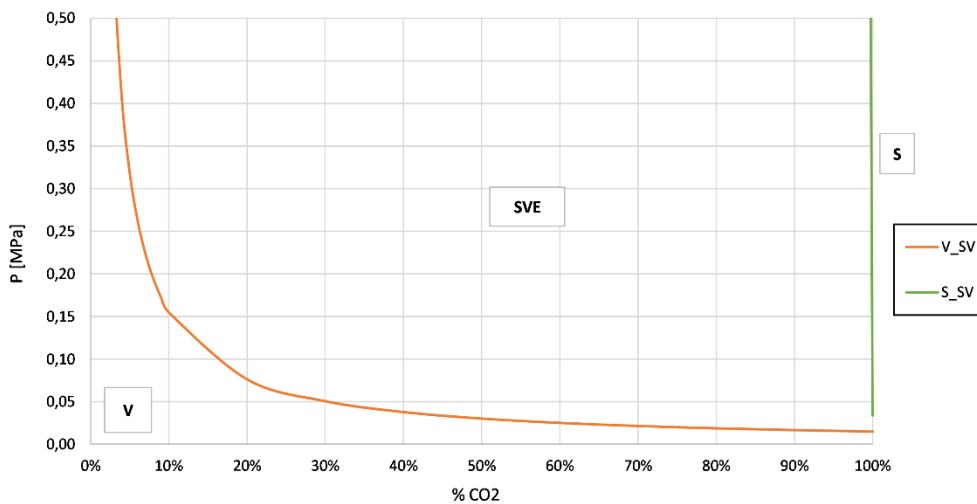


Figure 22 - P-x diagram for the binary mixture  $CH_4$ - $CO_2$ , at  $-100$  °C, where only S-SV and V-SV lines are drawn.

As can be noticed, the S-SV (Solid-Solid-Vapor) line in the pressure range considered, can be approximated to a straight vertical line. Furthermore, it is shown how the temperature influences the slope of the V-SV (Vapor-Solid-Vapor) equilibrium curve. Indeed, as the temperature is lowered, V-SV curve' slope is decreased as well, better noteworthy in Figure 24, where a comparison between the three curves is shown.

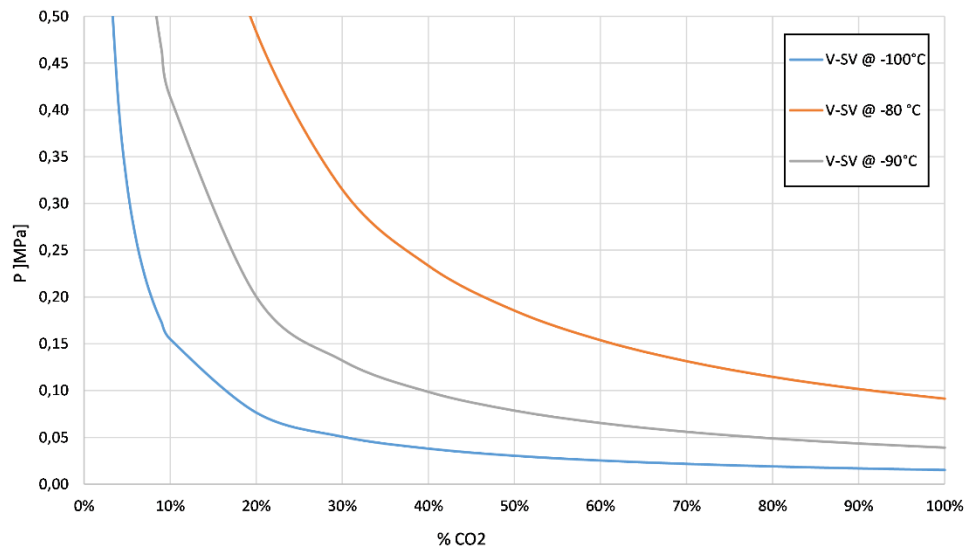


Figure 24 - Comparison between the three V-SV equilibrium curves.

Furthermore, it can be noticed that for higher temperatures (-80 °C) and lower pressures, no phase change in the mixture occurs. This is also demonstrated by applying the lever rule to each phase diagram, obtaining the results listed in Table 4.

Table 4 - Mass fraction of CO<sub>2</sub> frosted at different thermodynamic conditions.

CO <sub>2</sub> solid-phase mass fraction			
<i>p</i> [bar]	Scenario 1	Scenario 2	Scenario 3
1.00	0.00%	0.00%	27.86%
1.50	0.00%	18.49%	33.21%
2.00	0.00%	25.13%	35.01%
2.50	4.53%	27.84%	36.07%
3.00	13.10%	29.80%	36.36%
3.50	17.50%	31.97%	37.41%
4.00	21.02%	32.75%	37.65%
4.50	23.73%	34.08%	37.73%
5.00	25.91%	34.10%	38.57%

As it was predicted, CO<sub>2</sub> solid mass fraction rises increasing the pressure as well. Comparing the values listed in Table 4, it is shown that in the last two scenarios, for a biogas temperature outgoing the CRYO-HX of -90 °C and -100 °C, mass fraction assume similar values, especially for relatively high pressure. The same cannot be said for the first scenario, where no solid formation is observed up to 2 bar. A further rise in pressure will anyway cause lower solid fraction formation compared to those observed in the other two cases. This represents an interesting result from a technological point of view, as it would entail a lower operational cost, due to the low pressures involved.

Besides this, the sizing of the system can be achieved. Exploiting the information retrieved from the phase diagrams, the general behaviour of the system is meant to be defined, in order to understand the feasibility of realizing such a system.

## 3.2 PROPERTIES EVALUATION

To understand the overall system thermodynamic behaviour, it is first necessary to compute the properties of each component involved within the process, i.e. estimating the specific heat, latent heat of sublimation, density, for CH<sub>4</sub>, CO<sub>2</sub> and N<sub>2</sub>.

### 3.2.1 Specific heat evaluation

The evaluation of the specific heats for CO<sub>2</sub>, CH<sub>4</sub> and N<sub>2</sub> is performed through data fitting. Tables listing the specific heat capacity as a function of temperature have been found [21], from which the fitting has been carried. This operation is required since, in literature, values of the specific heat at the operating temperature are hard to find. By means of Matlab software, these data can be plotted and fitted, retrieving an equation describing the behaviour of the specific heat as temperature varies.

Concerning carbon dioxide specific heat, in Figure 25 is shown the plot of the specific heat against temperature, where data are retrieved from table [22]. In the same figure, are also shown the parameters concerning the goodness of the fit, where SSE stands for Sum of Squared estimate of Errors, also known as the residual sum of square (RSS), representing the inconsistency between the data and the estimation model. Such parameter is given by the summatory of the quadratic error between the *i*-th value of the curve the mean value. Small SSE values lead to greater accuracy of the fitting model. On the other hand, R<sup>2</sup> is a coefficient of proportionality between the variance and the correctness of the used model. Finally, RMSE is the root-mean-square error, that represents the relative standard deviation of the model applied [23].

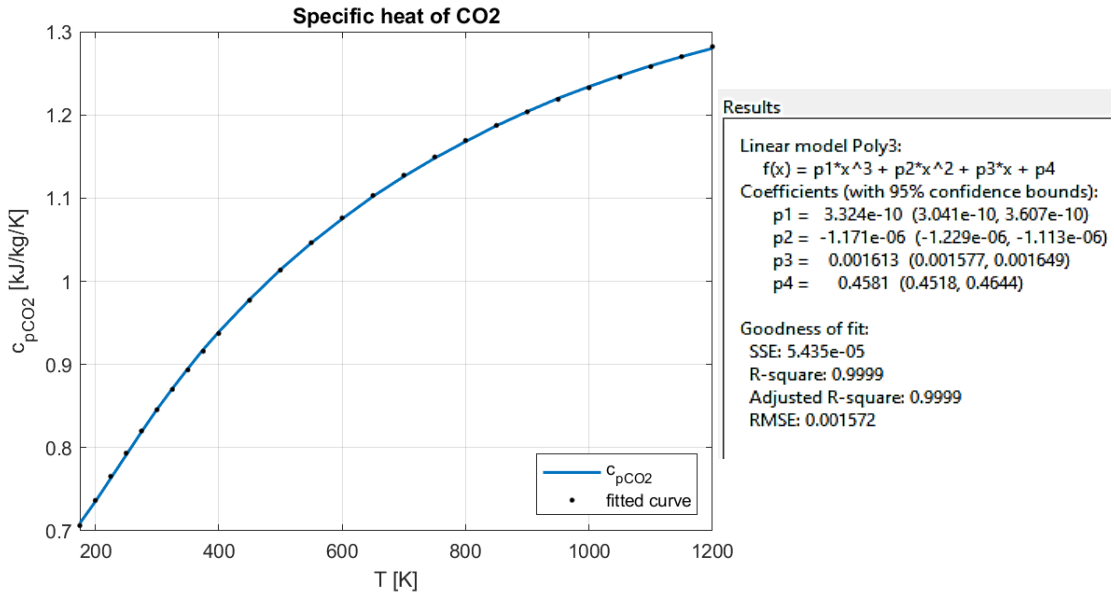


Figure 25 – Specific heat capacity of CO<sub>2</sub> as temperature varies, with the fitting coefficient and the goodness of fitting values.

The behaviour of the specific heat as a function of temperature, for CO<sub>2</sub>, is described by Eq. (61).

$$c_{pCO_2} = 3.324 \cdot 10^{-6} T^3 - 1.171 \cdot 10^{-6} T^2 + 0.001613 T + 0.4581 \quad (61)$$

Subsequently, substituting the temperatures of interest, expressed in K, the required specific heats are evaluated. Results are listed in Table 5.

Table 5 – CO<sub>2</sub> specific heat at the required temperatures.

$T_5$ [°C]	$T_5$ [K]	$c_p$ [kJ/kg/K]
-100	173.15	<b>0.707</b>
-90	183.15	<b>0.719</b>
-80	193.15	<b>0.732</b>

The same procedure is followed for CH<sub>4</sub> specific heat, where the plotted data, found in literature [24], and its fitted curve are shown in Figure 26. The function describing how methane specific heat evolves as a function of temperature is presented in Eq. (62).

$$c_{pCH_4} = -3.454 \cdot 10^{-9} T^3 + 6.522 \cdot 10^{-6} T^2 - 4.887 \cdot 10^{-4} T + 1.915 \quad (62)$$

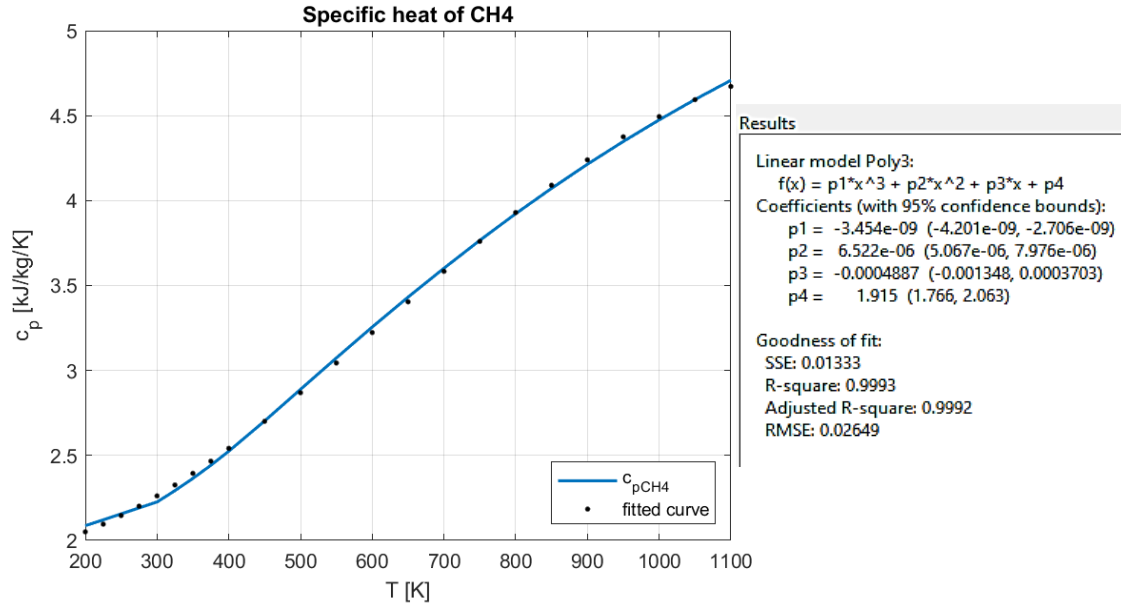


Figure 26 - CH<sub>4</sub> specific heat as function of temperature, with the fitting curve, as well as fitting coefficients and goodness of results.

As done for the CO<sub>2</sub>, exploiting Eq. (62), the required specific heats are estimated, whose values are listed in Table 6.

Table 6 – CH<sub>4</sub> specific heat at the temperatures considered.

$T_5$ [°C]	$T_5$ [K]	$c_p$ [kJ/kg/K]
-100	173.15	<b>2.022</b>
-90	183.15	<b>2.040</b>
-80	193.15	<b>2.058</b>

Finally, biogas specific heat can be evaluated performing a weighted average on its mass composition, as shown by Eq. (63).

$$c_{p_{biogas}} = c_{p_{CO_2}} \cdot \%CO_{2mass} + c_{p_{CH_4}} \cdot \%CH_{4mass} \quad (63)$$

Applying Eq. (63), the finale specific heat capacity of biogas mixture is found. Results are listed in Table 7.

Table 7 – Biogas Specific heat at the required temperatures.

$T_5$ (°C)	$T_5$ (K)	$c_p$ [kJ/kg/K]
-100	173.15	<b>1.171</b>
-90	183.15	<b>1.185</b>
-80	193.15	<b>1.200</b>

Concerning Nitrogen specific heat, its estimation is also required in order to estimate its flowrate within the cryogenic heat exchanger. The procedure is the same used for methane and carbon-dioxide.

The expression describing the behaviour of Nitrogen specific heat against temperature is represented by Eq. (64), obtained through the fitting of the curve, showed in Figure 27.

$$c_{p_{N_2}} = -2.604 \cdot 10^{-10} T^3 + 6.426 \cdot 10^{-7} T^2 - 0.0002882 T + 1.074 \quad (64)$$

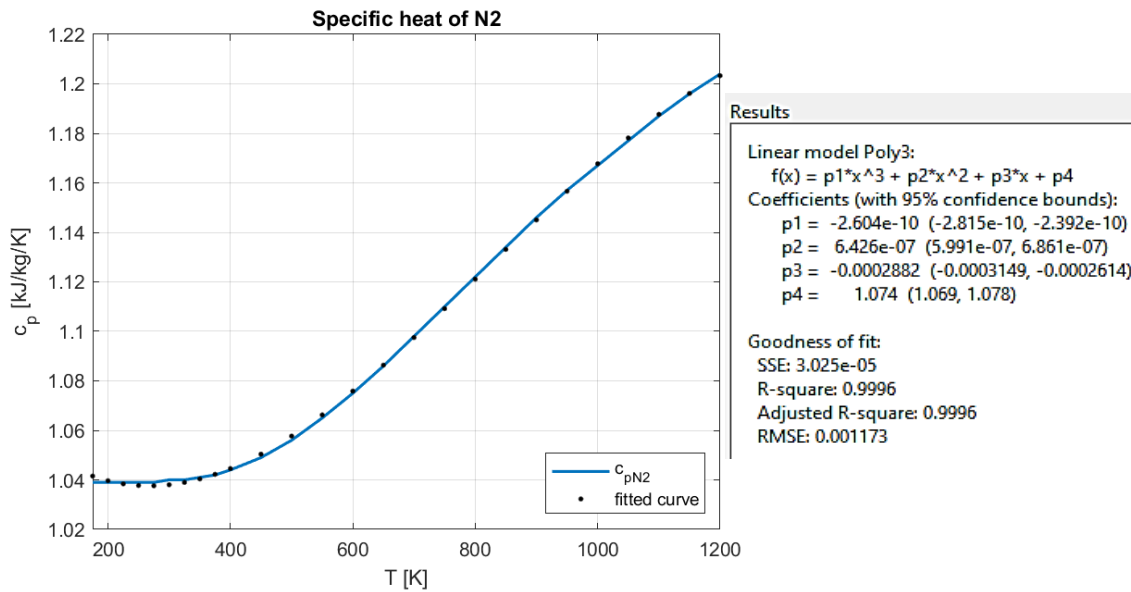


Figure 27 –  $N_2$  specific heat as function of temperature, with the fitting curve, as well as fitting coefficients and goodness of results.

Applying the Eq. (64) to the temperatures under analysis, Nitrogen specific heat is retrieved, whose values are listed in Table 8.

Table 8 – Specific heat of Nitrogen at temperatures of interests.

$T_{N_2,in} [^{\circ}C]$	$T_{N_2,in} [K]$	$c_p [kJ/kg/K]$
-120	153.15	1.044
-110	163.15	1.043
-100	173.15	1.042

### 3.2.2 Other properties

Concerning the other properties, the latent heat of sublimation has to be set. It has been found in literature, with a value of **573.03 kJ/kg**, assumed constant as pressure and temperature varies [25].

On the other hand, a non-negligible property is the density, whose value is a function of both temperature and pressure.

Biogas mixture is considered as an ideal one, therefore composed by ideal gases, i.e. CO<sub>2</sub> and CH<sub>4</sub>. Thanks to this assumption, it is possible to exploit the ideal gas Law expressed in terms of density, as Eq. (65) reports.

$$\frac{p}{\rho} = R^* \cdot T \quad (65)$$

Where  $R^*$  is the gas constant per unit mass, retrieved by dividing the gas constant,  $R = 8314$  J/kmol/K, by the molecular weight of the substance at which it has to be referred. For an ideal gas mixture, the gas constant of the mixture can be evaluated through the weighted average on its mass composition. Being  $x_{CO_2}$  and  $x_{CH_4}$  respectively the mass fractions of carbon dioxide and methan within the gas mixture, the gas constant for the biogas will be given by Eq. (66).

$$R_{biogas}^* = x_{CO_2} \cdot R_{CO_2}^* + x_{CH_4} \cdot R_{CH_4}^* \quad (66)$$

Hence, re-arranging Eq. (65) in order to obtain an expression for the density, Eq. (67) is obtained.

$$\rho = \frac{p}{R_{biogas}^* \cdot T} \quad (67)$$

Exploiting Eq. (67), it is possible to retrieve the density for the biogas mixture as a function of pressure and temperature.

Furthermore, once the gas constant for the biogas mixture is obtained, Laplace's coefficient could be computed. This is done by exploiting the Mayer's relationship, expressing thus the heat capacity ratio as Eq. (68) exhibits.

$$\gamma = \frac{c_p}{c_p - R^*} \quad (68)$$

Its value is estimated to be around 1.3 for the whole biogas mixture, which is exploited in the computation of the work of compression, Eq. (28).

### 3.3 COMPLETE SYSTEM ANALYSIS

In this section, the thermodynamic behaviour of such a system will be presented. Results coming from the procedure explained in section 2 are listed in this section, in order to have a qualitative picture of the system cornerstones.

First, the amount of heat produced by the Stirling engine has to be evaluated. As explained in section 2.4.2, the SPC-1 cooling power curve is exploited, Figure 18, obtaining thus the cooling power values listed in Table 9, where  $\phi_{st}$  stands for this quantity.



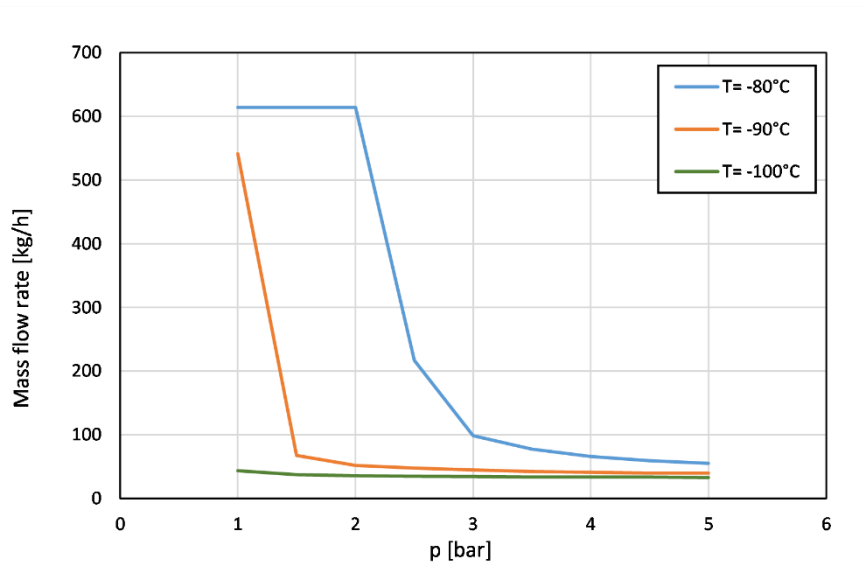


Figure 29 – Biogas mass flow rate behaviour as function of pressure, in the three different scenarios.

In addition, results coming from the analysis are listed in Table 10.

Table 10 – Results for the biogas mass flow rate in the three different scenarios.

	Scenario 1	Scenario 2	Scenario 3
$p$ [bar]	$\dot{m}_{gas}$ [kg/h]	$\dot{m}_{gas}$ [kg/h]	$\dot{m}_{gas}$ [kg/h]
1.00	614.24	541.31	43.54
1.50	614.24	67.72	37.38
2.00	614.24	52.01	35.70
2.50	217.01	47.56	34.79
3.00	98.66	44.81	34.54
3.50	77.37	42.15	33.70
4.00	66.06	41.26	33.51
4.50	59.45	39.84	33.45
5.00	55.05	39.82	32.82

Results exhibit a very wide range of flow rate that can be treated, at different operating conditions. When there is no phase change, the amount of biogas treated by the system reaches very high values, that is not so much realistic for the application analysed. Such a trend is due to the absence of solid formation within CRYO-HX component. Indeed, in these conditions, a higher amount of sensible heat is exploited, thus allowing to treat greater mass flows. Conversely, in those operating conditions involving carbon-dioxide frosting, it is observed a rapid mass flow rate decrease. Such a phenomenon is due to the release of latent heat of sublimation during the phase change, that has to be removed by the refrigerant fluid. The latent contribution covers the greater part of the thermal exchange, causing a reduction of sensible heat contribution, thus requiring a lower amount of mass flowing within the exchanger. Such behaviour is strongly observed in the third scenario when the biogas is cooled down up to -100 °C. Here, the amount

of biogas treatable varies in a tight range, from about 40 kg/h to 30 kg/h. A similar trend is shown in the second scenario, where at 1 bar no solid formation is observed, thus involving high biogas stream, while increasing the pressure, this quantity decreases with the same rate shown in the third case. On the contrary, the opposite trend is observed when biogas is brought to -80 °C, showing a wide variability range.

The mass flow rate of biogas is the main parameters for this simulation because it determines the overall system behaviour. Hence, results obtained for each component will be presented in the next paragraphs, avoiding the one concerning the dehumidification section, since the only parameter of interest is the outlet temperature, set to 5 °C.

### 3.3.1 Compressor

The compressor is the first component, whose aim is to pressurize biogas at the desired operating condition. Exploiting equation listed in section 2.1, results concerning the outlet temperature  $T_2$ , the work of compression and thus the power required are obtained, and listed in Table 11.

*Table 11 - Compressor results, including the discharge temperature, as well as the work of compression.*

$p_2$ (bar)	$T_2$ [°C]	$L_c$ [kJ]
1.00	-	-
1.50	27.98	29.99
2.00	30.27	52.99
2.50	32.15	71.88
3.00	33.75	88.04
3.50	35.17	102.22
4.00	36.43	114.91
4.50	37.57	126.43
5.00	38.62	136.99

As it was predictable, results show that increasing the pressure, the work expenditure increases as well. The same can be observed for the discharge temperature, whose rate of increase is proportional to the rise in pressure.

Furthermore, computing the product between the compression work  $L_c$  and the biogas flow rate, the power spent to perform the compression is estimated, whose evolution as function of pressure is illustrated in Figure 30. Here, it is observed that at  $T_5 = -80^\circ\text{C}$  the compression power  $W_c$  has a pick in correspondence of 2 bar. This is due to the increasing work of compression and to the high flow rate involved, i.e. when no solid formation occurs in the CRYO-HX component.

When the phase change occurs, instead,  $W_c$  curve has a downward trend, caused by the lower amount of biogas treated, as stated in Table 10.

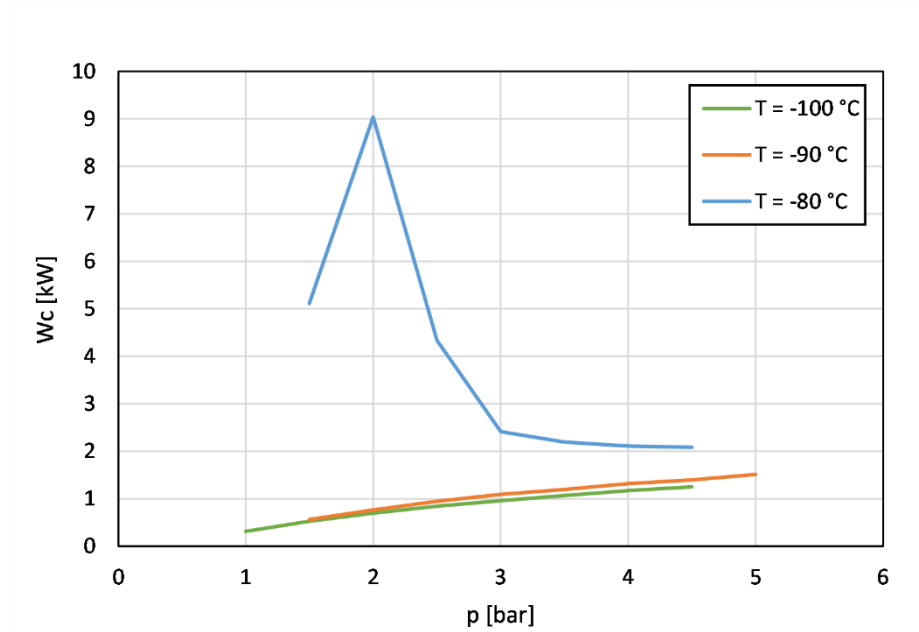


Figure 30 - Compression power at the different operating conditions analysed.

An opposite behaviour is registered for the other two scenarios, where an overall growing trend is observed, due to the lower amount of biogas treated. It is worthless to say that the case of 1 bar is not reported, since no compression is performed.

### 3.3.2 Economizer

ECO-HX is the first thermal step, where biogas is cooled down as much as possible, in order to better exploit the power supplied by the Stirling engine. The useful outputs are the outlet temperature  $T_4$ , corresponding to the incoming CRYO-HX stream, and the thermal power exchanged,  $\phi_{eco}$ .

In Figure 31, the hot-side downstream temperature ( $T_4$ ) evolution is shown, for the three different scenarios considered. The overall behaviour observed is increasing as pressure rises as well. Such trend is directly connected to the biogas flow decreasing trend, since the cold-side stream is constituted by the vapor fraction outgoing CRYO-HX component, which is lowered as pressure grows, due to higher amount of frosting  $\text{CO}_2$ .

Furthermore, the lowest temperature is reached in the second scenario ( $T_5 = -90$  °C), reaching a value of about  $-75$  °C. Moreover, when the biogas is brought to  $T_5 = -100$  °C, the outlet temperature reaches its minimum at around  $-60$  °C.

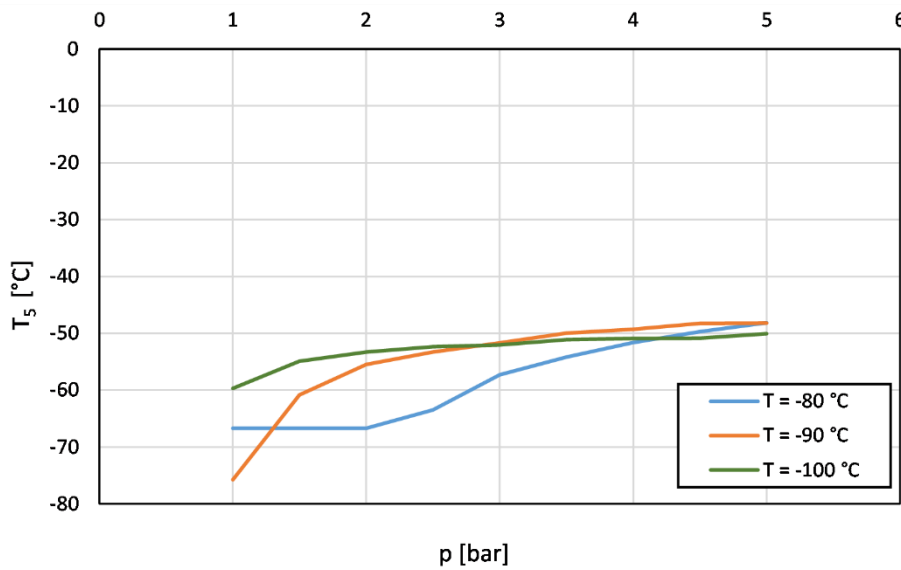


Figure 31 - ECO-HX downstream temperature, at the different operating conditions considered.

However, in all the three cases, it is observed that pressurizing the biogas up to 5 bar will cause an inlet CRYO-HX temperature around -50 °C. Hence, operating the system at low pressure will enhance the thermal exchange within the economizer.

In Figure 32, the second output parameter is plotted, i.e. the thermal power exchanged,  $\phi_{eco}$ .

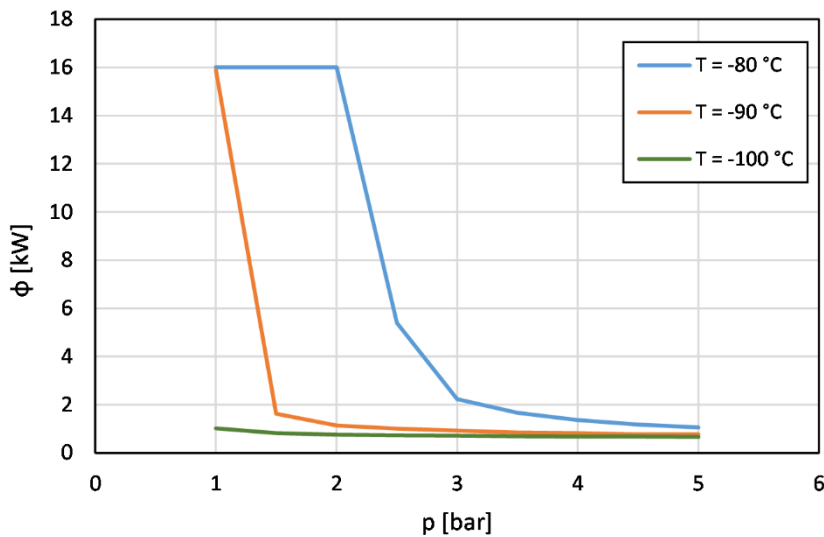


Figure 32 - Economizer thermal power exchanged, at different operating conditions.

The overall behaviour observed is the same shown for the flow rate. The main reason is that the thermal power and the biogas flow rate are directly proportional. Indeed, lowering the latter causes a decrease in  $T_4$ , thus involving a smaller amount of heat exchanged. Such a trend can be further noticed plotting these two quantities, as Figure 33 exhibits.

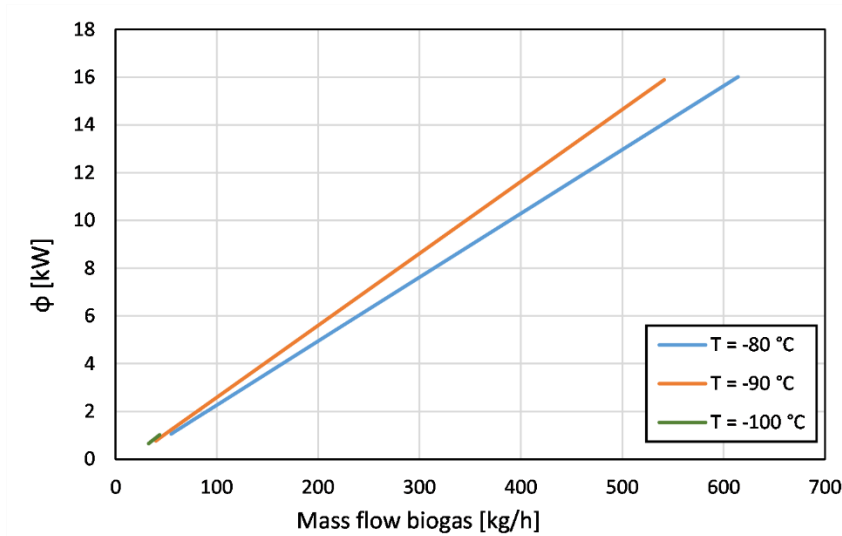


Figure 33 - Dependence between thermal power exchanged within economizer and biogas flow rate.

As can be observed from Figure 33, the dependence between the thermal power  $\phi_{eco}$  and the mass flow rate is linear, at any operating conditions. It has to be precise that the curve for the third scenario, green one, cannot be clearly appreciable due to lower flow rate values involved with respect to the other two scenarios.

### 3.3.3 Cryogenic heat exchanger

The cryogenic heat exchanger is the main component in such a system. Results that will be presented aim to illustrate how the solid formation during the phase change affects the thermodynamics. The focus is put on the estimation of the solid formation and the amount that do not undergoes any phase change, i.e. the vapor fraction, that it is exploited to perform thermal recovery within the economizer.

Scenario 1: when the biogas is brought to  $-80\text{ }^{\circ}\text{C}$ , results listed Table 12 are obtained.

Table 12 - CRYO-HX results obtained for scenario 1, for a downstream temperature of  $-80\text{ }^{\circ}\text{C}$ .

$p$ (bar)	$m_{frost}$ (kg/h)	$m_{vap}$ (kg/h)	$\phi_{sens}$ (kW)	$\phi_{lat}$ (kW)
1.00	0.00	614.24	2.700	0.000
1.50	0.00	614.24	2.700	0.000
2.00	0.00	614.24	2.700	0.000
2.50	9.84	207.17	1.134	1.566
3.00	12.92	85.74	0.643	2.057
3.50	13.54	63.83	0.546	2.154
4.00	13.89	52.18	0.490	2.210
4.50	14.11	45.34	0.455	2.245
5.00	14.26	40.79	0.430	2.270

Scenario 2: biogas brought up to -90 °C, results are listed in Table 13.

Table 13 - CRYO-HX results for scenario 2, when biogas is brought up to -90 °C.

$p$ (bar)	$m_{frost}$ (kg/h)	$m_{vap}$ (kg/h)	$\phi_{sens}$ (kW)	$\phi_{lat}$ (kW)
1.00	0.00	541.31	2.520	0.000
1.50	12.52	55.19	0.527	1.993
2.00	13.07	38.94	0.440	2.080
2.50	13.24	34.32	0.412	2.108
3.00	13.36	31.46	0.394	2.126
3.50	13.47	28.67	0.376	2.144
4.00	13.51	27.75	0.369	2.151
4.50	13.58	26.26	0.359	2.161
5.00	13.58	26.25	0.359	2.161

Scenario 3: results listed in Table 14 are obtained when biogas is cooled down to -100 °C.

Table 14 – CRYO-HX results in the third scenario, for a downstream temperature of -100 °C.

$p$ (bar)	$m_{frost}$ (kg/h)	$m_{vap}$ (kg/h)	$\phi_{sens}$ (kW)	$\phi_{lat}$ (kW)
1.00	12.13	31.41	0.409	1.931
1.50	12.41	24.97	0.364	1.976
2.00	12.50	23.20	0.350	1.990
2.50	12.55	22.24	0.343	1.997
3.00	12.56	21.98	0.341	1.999
3.50	12.61	21.09	0.333	2.007
4.00	12.62	20.90	0.332	2.008
4.50	12.62	20.83	0.331	2.009
5.00	12.66	20.16	0.325	2.015

As can be noticed, increasing the pressure involves high latent heat exchange  $\phi_{lat}$ , that has to be removed by the refrigerant fluid. Moreover, this effect reflects on the sensible heat  $\phi_{sens}$  contribution, which is lowered as pressure is increased. As consequence, the thermal exchange due to the temperature variation will be reduced, involving thus lower biogas flow rates. Such a phenomenon is registered when the phase change occurs. On the opposite, when no solid formation is encountered, a high amount of sensible heat can be exploited, leading to a greater amount of biogas flow as well.

In Table 12 it can be observed, at 2 bar, how a CO<sub>2</sub> frosted flow of few kg per hours leads to high latent heat formation. Moreover, such trend is observed in all the three scenarios, where the exothermic phase change covers the greater part of the overall heat exchanged.

Concerning the N<sub>2</sub> stream, the main results are listed in Table 15.

Table 15 – Results for the N<sub>2</sub> stream, used as refrigerant fluid.

<b><i>p</i></b> <b>[bar]</b>	<b>Scenario 1</b>		<b>Scenario 2</b>		<b>Scenario 3</b>	
	$T_{N_2,out}$ [°C]	$\dot{m}_{N_2}$ [kg/h]	$T_{N_2,out}$ [°C]	$\dot{m}_{N_2}$ [kg/h]	$T_{N_2,out}$ [°C]	$\dot{m}_{N_2}$ [kg/h]
<b>1.00</b>	-76.71	402.04	-85.77	360.16	-69.70	160.93
<b>1.50</b>	-76.71	402.04	-70.83	222.82	-64.91	146.91
<b>2.00</b>	-76.71	402.04	-65.47	196.00	-63.29	142.73
<b>2.50</b>	-73.46	352.78	-63.28	186.80	-62.34	140.39
<b>3.00</b>	-67.32	286.49	-61.70	180.69	-62.08	139.74
<b>3.50</b>	-64.17	261.28	-59.95	174.38	-61.14	137.52
<b>4.00</b>	-61.64	244.06	-59.32	172.21	-60.92	137.01
<b>4.50</b>	-59.69	232.29	-58.24	168.63	-60.86	136.85
<b>5.00</b>	-58.14	223.64	-58.23	168.58	-60.10	135.12

Even in this case, the trend is confirmed, i.e. increasing pressure lowers the refrigerant fluid mass flow rate. The outlet temperature is decreased as well, as a consequence of the  $\Delta T$  of 10 °C imposed with CRYO-HX hot-side inlet temperature,  $T_4$ .

Nitrogen mass flow rate trend is further due to the  $T_{N_2,out}$  estimation. Indeed, being constant the temperature difference between downstream cold-side and upstream hot-side, to remove a higher amount of heat released by the phase change, whose contribution increases as biogas pressure is grown, bigger nitrogen amount will be needed, involving thus greater flow rates.

The cold-side CRYO-HX is designed in a qualitative way, due to the lack of other information about the Stirling engine, for whom only the cooling power curve is provided (Figure 18).

### 3.4 HEAT TRANSFER SURFACE

In this section, results obtained concerning the heat exchange surface are presented. First, results for economizer heat transfer areas are shown, thus illustrating those coming from the CRYO-HX section, applying both 2 methods, explained in section 2.5.3.

An Excel spreadsheet is also set in this case, making the calculus automatic, for the ECO-HX case and for the first method concerning the CRYO-HX exchanger area. The application of the second method, instead, required a further goal seek analysis, in order to adjust temperature difference within the component. In Figure 34, the part of the Excel spreadsheet developed to compute the economizer area and the first method for the CRYO-HX component is presented.

<b>Economizer</b>			<b>Cryogenic HX ----&gt; Method 1</b>		
<b>ε-NTU method</b>			<b>ε-NTU method</b>		
Cmin	0,0072 kW/K		Cmin	0,0068 kW/K	Hot fluid
Cmax	0,0122 kW/K		Cmax	0,0396 kW/K	Cold fluid
Cmin/Cmax	0,589		Cmin/Cmax	0,171	
Wt,max	0,753 kW		Wt,max	2,475 kW	
ε	0,905		ε	0,945	
NTU	3,867		NTU	3,294	
U	35 W/m2/K		U	65 W/m2/K	
A	0,79 m2		A_sens	0,3424 m2	
<b>VERIFICA: LMTD</b>			<b>VERIFICA: LMTD</b>		
delta_T1	10,00 °C		delta_T1	10,00 °C	
delta_T2	49,08 °C		delta_T2	20,00 °C	
delta_Tml	24,56 °C		delta_Tml	14,43 °C	
phi_th	0,681 kW	OK	phi_th	2,3295 kW	
			err	0,4500%	
			A_tot	2,484 m2	

Figure 34 - Excel spreadsheet employed to estimate the heat transfer areas of ECO-HX and CRYO-HX (method 1) components.

As can be observed, in both cases, first the  $\epsilon - NTU$  method is applied, whose correctness is checked throughout the LMTD method. In the CYO-HX section, it is also computed the estimation error, whose value varies in a range of 0 %-13 %, evaluated through Eq. (56), being this methodology not properly suitable for such calculation. On the other hand, the Excel spreadsheet used to compute the second method, for the estimation of the cryogenic heat exchanger area, is illustrated in Figure 35.

1st region: sensible heat exchange only				2nd region: sensibi+latent heat exchange			
Hot side		Cold side		Hot side		Cold side	
T_in_cryo	222,23 K	T_N2_out	205,06 K	T_frost	212,68 K	T_o	202,68 K
T_frost	212,68 K	T_o	202,68 K	T_out_cryo	173,15 K	T_N2_in	153,15 K
G_gas	0,009 kg/s	G_N2	0,044 kg/s	G_gas	0,006 kg/s	G_N2	0,044 kg/s
cp_g1	1,231 kJ/kg/K	cp_N2_1	1,035 kJ/kg/K	cp_g2	1,218 kJ/kg/K	cp_N2_2	1,041 kJ/kg/K
phi_1	109,37 W	phi_1	109,37 W	phi_2	2287,80 W	phi_2	2287,80 W
U	35 W/m2/K			U	65 W/m2/K		
dT1	17,16 K			dT1	10,00 K		
dT2	10,00 K			dT2	20,00 K		
dTml	13,26			dTml	14,43		
A	0,236 m2			A	2,440 m2		
		phi	2,397 kW				
		err	2,44%				
		A_tot	2,675 m2				

T_in_cryo	-50,92 °C
T_frost	-60,47 °C
T_out_cryo	-100 °C
T_N2_out	-68,087 °C
T_o	-70,47 °C
T_N2_in	-120,00 °C
ΔT check	
diff_TN2_out	7,16 °C
dT_Hin,Cout	17,16 °C
dT_frost	10,00 °C
N2 mass flow variation	
G_N2	0,037941 kg/s
	136,588 kg/h
G'_N2	0,04438 kg/s
	159,77 kg/h
G'_N2 - G_N2	23,18 kg/h

Figure 35 – Part of the Excel spreadsheet exploited to compute method 2 in the estimation of CRYO-HX area.

In this case, it was necessary to compute other quantities, such as the CO<sub>2</sub> frosting temperature, retrieved from its phase diagram. Furthermore, it can be appreciated the check on the temperature difference on the right side of Figure 35. The term “dT\_frost” identifies the temperature difference registered at the two-region interface, whose value violated in most of the cases, the minimum temperature difference imposed. Such a phenomenon happens mainly when a phase change occurs in the second region. Therefore, another goal seek iteration is performed, in order to set this value equal to the minimum allowed, i.e. 10 °C. Moreover, observing the shape of the curve, reported in Figure 36, where a plot of the temperature evolution within the exchanger is drawn, it has observed that fixing the two region interface  $\Delta T$  to the minimum allowed, the hot-side inlet and cold-side outlet temperature difference will be always greater than 10 °C. The main cause of such trend can be ascribed to the only sensible heat exchange within the first region. Indeed, observing the curve trend in the second region, it can be appreciated how the hot-side temperature falls down rapidly, while the refrigerant temperature goes upwards with the same rate. This is liable to the latent heat released during the phase change, whose weight is greater than the sensible contribution. Furthermore, when no phase change occurs, the adjustment required is on the temperature difference between hot-side inlet and cold-side outlet streams, registered in the first region.

It has to be pointed out that Figure 36 does not represent the general behaviour of temperature distribution along the exchanger surface. Here it is reported just to have a better vision of the overall behaviour. However, such a trend is observed when the phase change occurs, while a change in slope is registered, for both curves, when no solid formation is encountered.

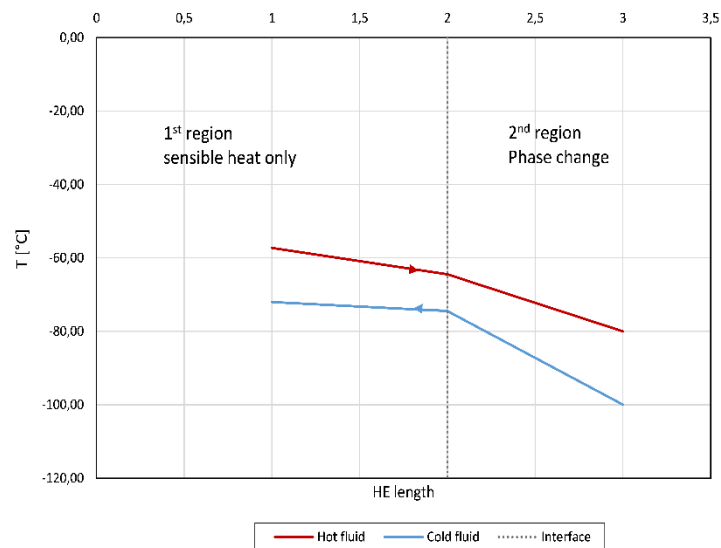


Figure 36 - Temperature evolution within the CRYO-HX component, used to as check for the second method.

Exploiting this knowledge and making use of the Excel spreadsheet already illustrated, results are obtained.

For what regards the overall heat transfer coefficient, due to the lack of any geometrical data, its value is retrieved from literature. In the ECO-HX, the value used is  $35 \text{ W/m}^2/\text{K}$ , valid for a gas-gas heat exchanger type [26]. Such value is also exploited in the first region when evaluating the heat transfer area exploiting method 2. Conversely, when the two-phase flow is registered, the overall heat transfer coefficient employed is taken from a journal article, where tests are carried on a plate type heat exchanger to remove  $\text{CO}_2$  from biogas mixture by cooling it down up to cryogenic levels. Such value is  $65 \text{ W/m}^2/\text{K}$  [27].

Concerning the ECO-HX component, results obtained for scenarios 1 and 2 are shown in Figure 37.

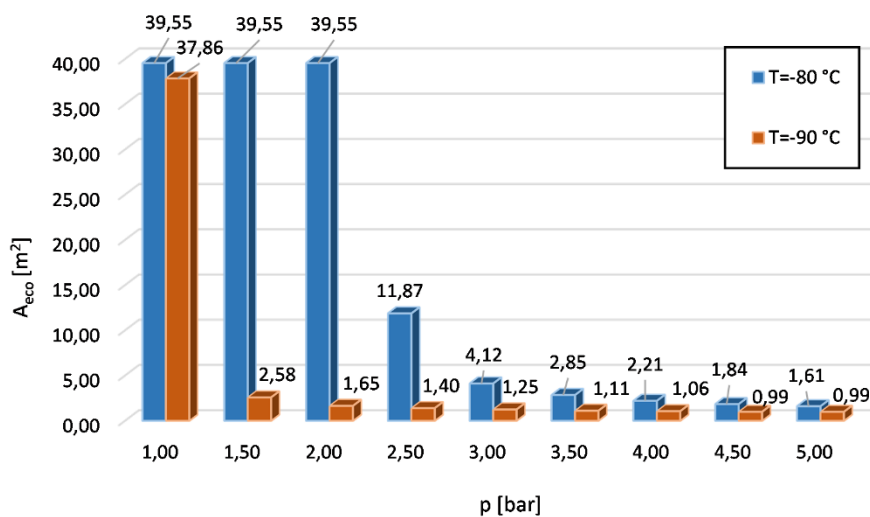


Figure 37 - ECO-HX heat transfer areas, for scenarios 1 and 2.

Results for the third scenario are not illustrated in Figure 37, due to the lower value involved, so that it is not clearly appreciable plotting all the three scenarios in the same figure. Hence, in Figure 38, the third scenario results are presented.

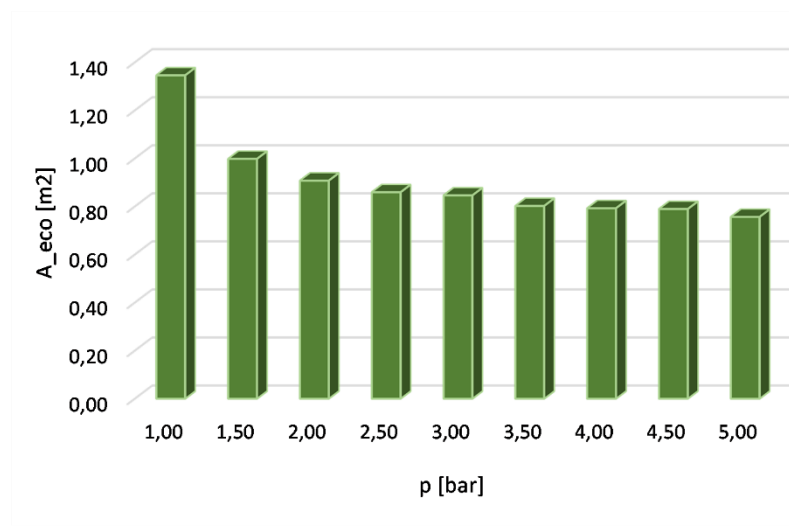


Figure 38 - Heat transfer areas for the third scenario, ECO-HX component.

Results prove how the heat transfer surface decreases as the biogas is compressed. Indeed, considering the mass flow rates, in Figure 29, such trend was predictable, due to lower amount of biogas treated, which in turns let decrease the thermal heat exchanged, thus requiring lower surface.

Observing Figure 37, it is found that the heat transfer area reaches very high value, not realistic. Indeed, such values are obtained in the cases where no CO<sub>2</sub> frosting occurs, thus exploiting a greater amount of biogas flow, involving thus higher amount of thermal power exchange. On the other hand, when CO<sub>2</sub> starts sublimating in the cryogenic heat exchanger, heat transfer areas go down very rapidly, reaching values lower than the unity. The same can be said concerning the third scenario, in Figure 38.

For what regards the cryogenic heat exchanger, both method results are presented, together with the computational error. In such case, resulting areas showed to have a similar value, although affected by different errors. Furthermore, the frosting point is also presented, necessary for the exchanger surface computation.

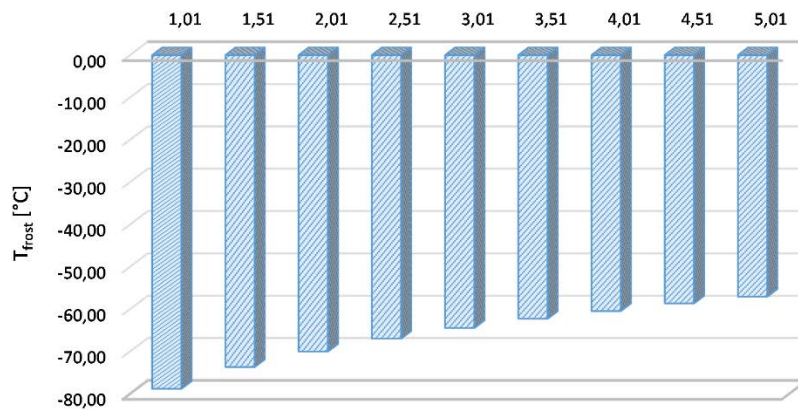


Figure 39 – CO<sub>2</sub> frosting point at different pressure conditions.

As Figure 39 exhibits, the temperature at which the phase change occurs decreases as pressure grows. Hence, pressurized biogas involves a smaller region of sensible thermal exchange only (region 1, considering the second method), due to its lower CRYO-HX inlet temperature, as Figure 31 explains, as well as to lower temperature at which carbon dioxide starts to sublime.

Furthermore, it has to be said that these values are retrieved from the phase diagram of the CO<sub>2</sub> mono-component. Thus, even though it has been found that at -80 °C no phase change occurs, such aspect is neglected. This approximation was necessary, due to lack of information from the binary mixture phase diagrams about the temperature at which CO<sub>2</sub> starts to sublime. It could be possible to estimate this value, but it would require the plot of many P-x phase diagram at different temperatures, which in terms of computational costs, is very expensive. Such consideration will play an important role in the estimation, leading thus to a certain amount of uncertainty in the results, that will be presented as follows.

Scenario 1: results listed in Table 16, exhibit a comparison between the two methods at the different operating pressures, cooling the biogas flow up to -80 °C.

Table 16 - Comparison between the two methods developed for the CRYO-HX area estimation, scenario 1.

P [bar]	Method 1			Method 2			
	A <sub>th,s</sub> [m <sup>2</sup> ]	A <sub>tot</sub> [m <sup>2</sup> ]	%err	A <sub>1</sub> [m <sup>2</sup> ]	A <sub>2</sub> [m <sup>2</sup> ]	A <sub>tot</sub> [m <sup>2</sup> ]	%err
1.00	5.347	5.347	0.00%	5.069	0.189	5.258	1.40%
1.50	5.347	5.347	0.00%	3.297	1.133	4.431	1.14%
2.00	5.347	5.347	0.00%	1.741	1.976	3.716	1.24%
2.50	1.604	3.274	13.72%	0.697	2.636	3.334	1.10%
3.00	0.942	3.135	8.88%	0.560	2.672	3.232	1.65%
3.50	0.778	3.075	6.81%	0.579	2.654	3.232	2.22%
4.00	0.680	3.037	5.48%	0.438	2.725	3.163	2.02%
4.50	0.618	3.012	4.62%	0.398	2.744	3.143	2.07%
5.00	0.574	2.995	4.02%	0.368	2.760	3.128	2.09%

Scenario 2: results listed in Table 17, compare the two methods applied, in the case the biogas is cooled down up to a temperature  $T_5$  equal to  $-90^{\circ}\text{C}$ .

Table 17 - Comparison between the two methods applied for the CRYO-HX area estimation, scenario 2.

$P$ [bar]	Method 1			Method 2			
	$A_{th_s}$ [ $\text{m}^2$ ]	$A_{tot}$ [ $\text{m}^2$ ]	%err	$A_1$ [ $\text{m}^2$ ]	$A_2$ [ $\text{m}^2$ ]	$A_{tot}$ [ $\text{m}^2$ ]	%err
1.00	4.991	4.991	0.00%	1.522	2.097	3.619	1.35%
1.50	0.693	2.819	4.89%	0.592	2.446	3.037	2.69%
2.00	0.546	2.764	2.87%	0.493	2.496	2.989	3.10%
2.50	0.500	2.747	2.24%	0.433	2.531	2.963	2.99%
3.00	0.470	2.737	1.84%	0.389	2.555	2.944	2.85%
3.50	0.440	2.726	1.45%	0.399	2.550	2.949	3.19%
4.00	0.429	2.723	1.32%	0.325	2.589	2.914	2.60%
4.50	0.413	2.717	1.12%	0.299	2.602	2.901	2.49%
5.00	0.412	2.717	1.12%	0.264	2.618	2.882	2.21%

Scenario 3: results listed in Table 18, exhibit the comparison between the two methods applied when biogas is brought to  $-100^{\circ}\text{C}$ .

Table 18 - Comparison between the two methods applied for the CRYO-HX area estimation, scenario 3.

$P$ [bar]	Method 1			Method 2			
	$A_{th_s}$ [ $\text{m}^2$ ]	$A_{tot}$ [ $\text{m}^2$ ]	%err	$A_1$ [ $\text{m}^2$ ]	$A_2$ [ $\text{m}^2$ ]	$A_{tot}$ [ $\text{m}^2$ ]	%err
1.00	0.460	2.519	0.96%	0.4916	2.294	2.786	3.97%
1.50	0.390	2.497	0.08%	0.419	2.341	2.759	4.01%
2.00	0.370	2.492	0.15%	0.373	2.370	2.742	3.67%
2.50	0.359	2.488	0.28%	0.332	2.393	2.725	3.32%
3.00	0.355	2.487	0.31%	0.294	2.413	2.707	2.93%
3.50	0.345	2.485	0.43%	0.302	2.409	2.711	3.10%
4.00	0.342	2.484	0.45%	0.236	2.440	2.675	2.44%
4.50	0.342	2.484	0.46%	0.201	2.454	2.655	2.14%
5.00	0.333	2.482	0.54%	0.180	2.462	2.642	2.00%

As it was foretalled, both methods exhibit similar results. Concerning the first procedure, it is observed that in such cases where no phase transition occurs, the computation returns the exact value. The same cannot be said when the computation is performed through method 2. The main reason lies in the HX region splitting. In fact, in such cases the goal seek analysis is carried acting on the temperature difference between the hot-side upstream and cold-side downstream, by varying Nitrogen flow rate. Indeed, once the iterations are performed, the  $\text{N}_2$  flow assumes slightly higher value with respect to those listed in Table 15, leading thus to higher amount of thermal power exchanged in the first region.

On the other hand, when phase change is registered, different errors are observed. Concerning method 2, its overall behaviour is quite uniform, varying in a range between 2% and 4%. The opposite is observed when method 1 is applied. In such case, a wide range of variation is registered, varying more or less from 13% to 0.1%. It is also noticeable from Table 17, that method 1 produces results with great accuracy. This observation leads to an important consideration. Plotting the errors as a function of the frosting percentage, as shown in Figure 40, a trend is found.

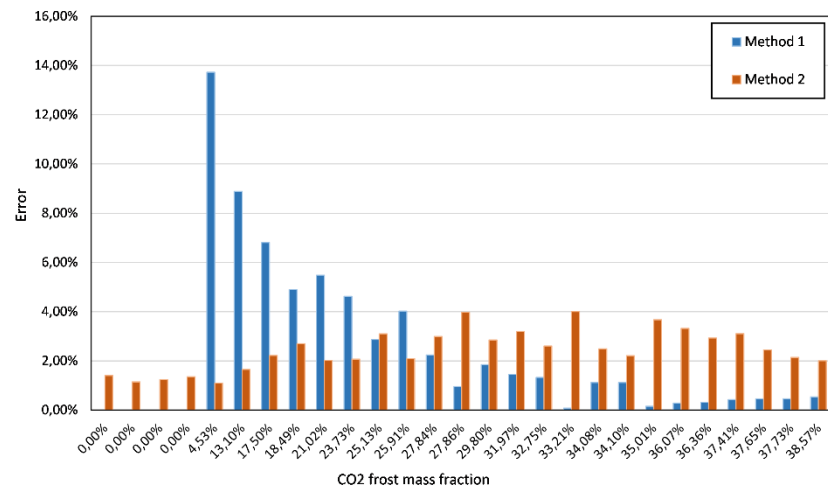


Figure 40 - Trend of the estimation error with respect to CO<sub>2</sub> solid mass fraction.

Observing the blue bars, representing the estimation error committed using method 1, it can be said that for low solid mass fraction it assumes high values. Subsequently, increasing the CO<sub>2</sub> frosting percentage the error falls down exponentially, assuming smaller values, as shown in the third scenario. Such behaviour is due to how the method has been set. Indeed, the amount of latent heat is assumed to be constant over the entire length of the exchanger, hence, growing solid CO<sub>2</sub> mass fractions will involve lower sensible heat contribution, whose effect reflects on the error calculation. On the other hand, method 2 exhibits a more or less uniform trend as phase change occurs, as it is more suitable for such calculations. Indeed, having other geometrical data on the heat exchanger, the accuracy could be increased by further splitting the exchanger into tinier elements, thus accounting for those physical quantities that are neglected, as illustrated in section 2.5.3.

The suitable solution in computing the heat transfer area is thus a combination of the two. When no phase change occurs, method 1 is preferred, since it returns the exact value. On the other hand, when CO<sub>2</sub> starts to sublime, method 2 should be computed, due to the accounting for properties variation, although it would be better to consider more zones or elements so that greater accuracy can be achieved.

## 4 OPTIMAL OPERATING CONDITIONS

---

The work done until now is meant to have a clear picture of the overall system behaviour. Hence, at this stage it is possible to examine a final layout, choosing among the illustrated conditions, the most suitable. Subsequently, an overall system sizing will be achieved, choosing a specific heat exchanger type where biogas cooling will be performed. Finally, an economic comparison between such a system and a traditional desulphurization one will be discussed.

Aiming to this purpose, together with Biokomp company, some operating constraints are fixed. The main restriction is set on the maximum amount of treatable biogas. Due to the range of pressure explored, both blower and compressor are bought, in order to test the different pressure conditions. When the compressor is used, the maximum allowed biogas flow is around 150 m<sup>3</sup>/h. Conversely, when a blower is exploited, such value decreases to a maximum of 100 m<sup>3</sup>/h, with a pressure increase of 500 mbar. The case involving the compressor will be widely discussed, and a final economic comparison with the blower case will be performed.

Other useful information regards the refrigerant exploited in the CRYO-HX component. Here, Nitrogen flowing is supposed to be compressed at 3 bar, with a flow rate of 18 m<sup>3</sup>/h.

### 4.1 SYSTEM SIZING

The first step is the estimation of the whole system thermodynamic cornerstones, under specific operating temperature and pressure conditions. Among those illustrated in section 4, the chosen one are:

- $T_5 = -80\text{ }^{\circ}\text{C}$ , when no CO<sub>2</sub> frosting is observed but H<sub>2</sub>S is expected to be removed.
- $p = 1.5\text{ bar}$ .

In such conditions, the system can treat a maximum biogas flow of 614.24 kg/h, as stated in Table 10, and no solid CO<sub>2</sub> formation is registered. It has to be recalled that the aim of the system is to condensate contaminants, avoiding CO<sub>2</sub> removal, to be subsequently exploited in a SOFC-based system. Hence, these conditions are the most suitable to reach such a purpose.

Therefore, exploiting the Excel spreadsheet illustrated in Figure 28, the thermodynamic cornerstones are retrieved. Moreover, another goal seeks analysis needs to be performed, in order to set the flow rate of the incoming biogas stream to the threshold value imposed. This adjustment is carried upstream the compressor, where the flow rate is expressed in m<sup>3</sup>/h by referring the density at such thermodynamic conditions, due to the wide temperature range that affects heavily the density. Indeed, despite the pressure is assumed to be constant over the

whole system (1.5 bar), plotting the density as a function of temperature, the trend illustrated in Figure 41 is found.

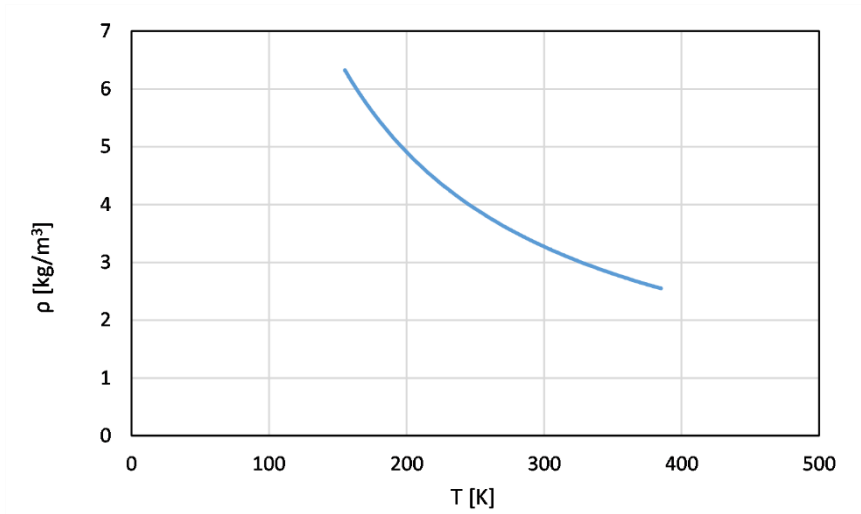


Figure 41 – Biogas density as a function of temperature, at a fixed pressure.

Hence, at a fixed pressure, as the temperature is lowered biogas density increases exponentially. Such trend reflects on the volumetric flow rate, evaluated by dividing the mass flow, expressed in kg/h, over the density referred at that pressure and temperature. Hence, the volumetric flow entering the system will differ from that found within the cryogenic heat exchanger. Because of that, the goal seek Excel function is exploited. Setting the incoming volumetric biogas flow rate equal to the maximum that the compressor can withstand, i.e. 150 m<sup>3</sup>/h, the mass flow rate is varied until convergence. Besides this, temperature estimation is not affected by such calculation.

Hence, performing the above-illustrated procedure, the thermodynamic cornerstones are retrieved. Table 19 lists the stream resulting temperature, where subscripts refer to each stream name.

Table 19 - Stream temperature results for the final scenario analysed.

$T_{biogas_{in}}$	25.00 °C
$T_2$	27.98 °C
$T_3$	5.00 °C
$T_4$	-66.71 °C
$T_5$	-80.00 °C
$T_{biogas_{out}}$	-5.00 °C
$T_{N_2,in}$	-100.00 °C
$T_{N_2,out}$	-76.71 °C

On the other hand, in Table 20 resulting flow rate values are listed, both in kg/h and m<sup>3</sup>/h, where stream  $S5_{frost}$  and  $S5_{vap}$  states for the biogas frosted fraction and the vapor one, respectively; whilst, in Table 21 the heat transfer rates exchanged in each system section are illustrated.

Table 20 – Biogas flow rate in the different system streams, both mass and volume rate are presented.

<b>Stream</b>	$\dot{m}_{biogas}$ [kg/h]	$\dot{m}_{biogas}$ [m <sup>3</sup> /h]
<b>S1</b>	164.59	150.00
<b>S3</b>	164.59	81.27
<b>S5</b>	164.59	64.78
<b><math>S5_{frost}</math></b>	0.00	0.00
<b><math>S5_{vap}</math></b>	164.59	64.78
<b><math>N_2 - in</math></b>	107.34	18.40

Table 21 - Thermal power exchanged in each system component.

<b>Component</b>	$\phi$ [kW]
<b>DH</b>	1.42
<b>ECO – HX</b>	4.29
<b>CRYO – HX</b>	0.72

As can be noticed from Table 19, temperatures shown seems not to be affected by the mass flow variation. This is mainly due to the same biogas flow rates registered in the ECO-Hx component, where on both hot and cold sides such value decreases, thus not affecting  $T_4$  estimation (Eq. (31)). Likewise, other temperatures do not vary from those values observed in section 3.3, due to the estimation methodology applied.

Conversely, what is affected by the mass flow variation are the thermal power exchanged, as Table 21 exhibits. Indeed, it can be observed how the cooling power provided to biogas from the Stirling engine is decreased significantly, from a value of 2.70 kW (Table 9) to 0.72 kW. The same can be observed within the ECO-HX, where such value was registered at around 16 kW, as Figure 32 claims.

Concerning results listed in Table 20, it can be appreciated how the volumetric flow rate decreases as the temperature is lowered, due to the density exponential growth, as portrayed by Figure 41.

## 4.2 HEAT EXCHANGER DESIGN

At this stage, a type of heat exchanger (HE) will be analysed, in order to make a subsequent estimation of such a system cost. Research is carried in this field, aiming to understand what the most suitable typology is to perform cryogenics. J.C. Pacio et al [19] published an article listing the most suitable heat exchanger types aiming to this purpose, that are summarized in Figure 42.

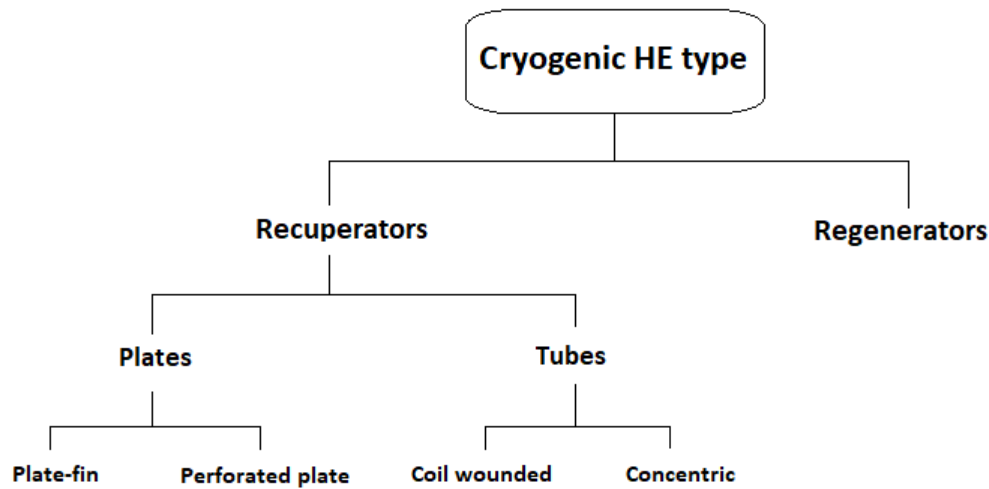


Figure 42 - Different heat exchanger type for cryogenic applications.

Cryogenic heat exchangers can be divided mainly into two categories: recuperators and regenerators. The first category groups all the HE typologies where heat is transferred from one fluid to the other across a separating surface. Conversely, into regenerators, both fluids alternatively flow in the same space and the thermal exchange occurs by means of a heat storage medium, which releases the thermal energy brought by the hot fluid to the cold one. Moreover, recuperators can be further split into plates and tubular type: to the first belong the plate-fin and the perforated plate configurations, whilst concentric and coil wounded belong to the tubular type. A brief description of such typologies is illustrated as follows, aiming to exhibit the main advantages and disadvantages:

- Concentric tube HEs are mainly employed for small scale application, especially for laboratory purpose.
- Coil-wounded heat exchangers (CWHE) are employed for large scale applications. It consists of a mandrel around which several helically wounded tubes are installed. Such configuration can be used including different tubes layer uniformly spaced, thanks to a punched brass strip. Each tubes-layer carries a particular fluid, resulting in a multi-stream arrangement. However, such equipment is quite expensive.

- Perforated-plate heat exchangers (PPHEs) are constituted by a parallel of perforated plates through which fluids flow. Each plate is separated by a spacer and the thermal exchange occurs laterally through the high-conductivity plates. Such configuration is employed in small scale applications, offering high heat transfer coefficient (HTC) even though resulting in expensive equipment.
- Plate-fin heat exchangers (PFHEs) are mainly composed of several corrugated plates separated by a thin metal layer. The two fluids flow alternatively into two adjacent plates, consisting in a parallel counter-current flow-arrangement. The corrugation, typically of the *chevron* type, act as a fin ensuring thus high heat transfer areas, notwithstanding larger chevron angles bring higher pressure drops. Hence, such a configuration results in compact and small-size HE, offering a very high heating surface density ( $m^2/m^3$ ), resulting in lower capital and operating costs, compared to traditional shell-and-tube HE types.

Among the heat exchangers discussed above, the chosen one is the plate-fin type, representing the most suitable for the application under analysis. Indeed, its compactness ensures low encumbrance and high heat transfer area, thus low capital costs.

Different companies provide such heat exchanger type. The one picked is the *brazed plate HE BV 95* provided by Pacetti company [28]. Such typology of HE is employed in different fields, such as civil applications and industrial applications, as for machine tool cooling and for refrigeration. Brazed plate HE works in a parallel counter-current flow-arrangement, where the two fluids circulate in separated circuits. A schematic flow diagram representing a typical BV plate HE is shown in Figure 43.

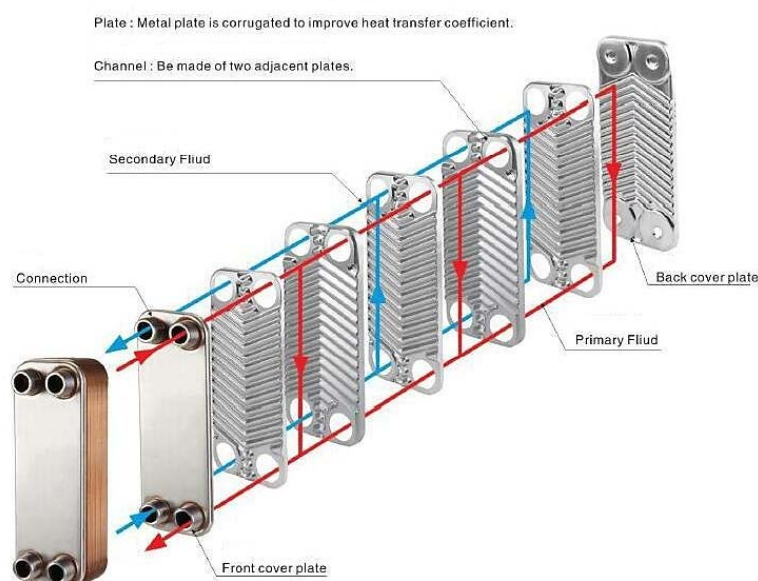


Figure 43 - BV brazed heat exchanger schematic flow arrangement and plate configuration [36].

Moreover, such typology can work with both liquid and gas flows. The absence of a gasket between plates, which are instead welded by a copper brazing, allows to work in a wide range of temperatures and to reach high pressures as well. The technical datasheet of BV 95 brazed heat exchanger is available in Table 22, whose geometry quantities are illustrated in Figure 44 [29].

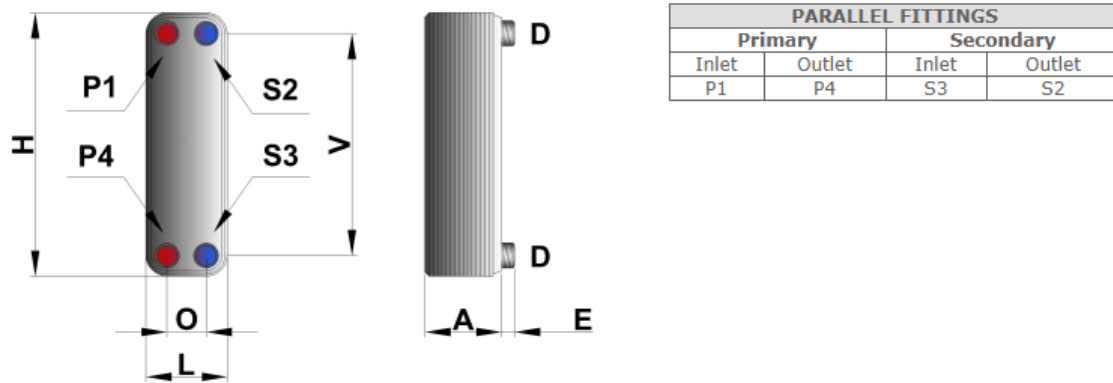


Figure 44 - Pacetti BV95 brazed heat exchanger, geometry scheme.

Table 22 - Pacetti BV 95 heat exchanger geometrical data.

Dimension	Unit	BV95
H	mm	616
L	mm	191
A	mm	11 + (np x 2.8)
E	mm	20
O	mm	92
V	mm	519
<b>D (threaded)</b>	inches	2''

The term np states for the number of plates. Furthermore, from the BV catalogue, it is available a formula to estimate the heat transfer area  $S_{th}$ , reported by Eq. (69).

$$S_{th} = 0.095 \cdot (np - 2) \quad (69)$$

Moreover, no information is given concerning the width of the plate, as well as the spacing between two adjacent plates. Such values are assumed because they will be exploited later. The typical plate thickness range is 0.5-3 mm, spaced one from the other by a distance that could vary between 1.5-5 mm [30]. Thus, looking at the parameter A, in Table 22 at the fourth row, np is multiplied by a factor of 2.8, that corresponds to the sum of the two unknown quantities. Therefore, on the basis of the typical dimension ranges, it is assumed a plate thickness of 0.8 mm, while the plate spacing corresponds to 2 mm.

Furthermore, Table 23 lists other useful features, such as the operating range conditions and the plate composition material as well.

*Table 23 - Pacetti BV 95 heat exchanger other features, i.e. operating conditions and material composition.*

<b>Working temperature</b>	-160 °C ÷ 200 °C
<b>Max working pressure</b>	30 bar
<b>Plate material</b>	Stainless steel 316L
<b>Brazing</b>	Copper 99.99 %

Hence, knowing the heat exchanger geometrical data that will be exploited to cool down the biogas, a more accurate estimation of the heat transfer area required to achieve the thermal powers listed in Table 21 can be performed. To accomplish such a requirement, the overall heat transfer coefficient has to be computed.

The estimation of the overall heat transfer coefficient requires other properties calculations. Indeed, for a flat separating surface, such coefficient is given by Eq. (70).

$$\frac{1}{U} = \frac{1}{h_i} + \frac{w_{ss}}{\lambda_{ss}} + \frac{1}{h_e} \quad (70)$$

Where  $h_i$  and  $h_e \left[ \frac{W}{m^2K} \right]$  are respectively the convective heat transfer for the inner and outer separating surface, i.e. of the two fluids flowing.  $w$  is the surface thickness, while  $\lambda \left[ \frac{W}{mK} \right]$  is its thermal conductivity; the subscript  $ss$  states for the separating surface material, in this case, stainless steel. Hence, convective coefficients  $h$  and conductivity  $\lambda$  need to be computed.

Concerning the convective heat transfer coefficient  $h$ , it is evaluated through Eq. (71).

$$h = \frac{Nu \cdot \lambda}{D_e} \quad (71)$$

Where  $D_e$  is the hydraulic diameter, that for a plate heat exchanger is given doubling the plate spacing  $b$ , as Eq. (72) demonstrate.

$$D_e = 2 \cdot b \quad (72)$$

On the other and, the term  $Nu$  stands for the Nusselt number, representing the ratio of the amount of heat exchanged by convection over the amount exchanged by conduction. Its value is retrieved by empirical correlations, varying depending on the thermal exchange mechanism. For a vertical flat plate, the heat transfer mechanism is the free convection, i.e. fluid flow is originated by the effect of gravity due to the density gradient, which is caused by thermal gradients. For such case, the flow is characterized by the Rayleigh dimensionless number, whose

value describes the flow regime: over a threshold level, established at  $10^9$ , the stream is turbulent, otherwise laminar flow occurs. Its value is retrieved by computing Eq. (73).

$$Ra = \frac{g \cdot \beta \cdot (T_s - T_m) \cdot x^3}{\nu \cdot \alpha} \quad (73)$$

The different terms composing Eq. (73) are listed as follows:

- $g$  is the gravitational acceleration, equal to  $9.81 \text{ m/s}^2$ .
- $\beta$  is the inverse of the mean fluid temperature.
- $T_s$  is the surface temperature, corresponding to the plate temperature, expressed in K.
- $T_m$  is the mean fluid temperature, evaluated as the arithmetic average between the upstream and downstream temperature, expressed in K.
- $x$  is the plate length, expressed in m.
- $\nu$  is the kinematic viscosity, expressed in  $\text{m}^2/\text{s}$ , given by Eq. (74), where  $\mu$  is the dynamic viscosity, expressed in  $\text{Pa} \cdot \text{s}$ .

$$\nu = \frac{\mu}{\rho} \quad (74)$$

- $\alpha$  is the thermal diffusivity, expressed in  $\text{m}^2/\text{s}$ , whose value is given by Eq. (75).

$$\alpha = \frac{\lambda}{\rho \cdot c_p} \quad (75)$$

Depending on  $Ra$  value, different correlations are available for  $Nu$  estimation. Churchill and Chu proposed an empirical correlation valid for all flow regime, computing an average Nusselt number, shown by Eq. (76).

$$\overline{Nu} = \left\{ 0.825 \cdot \frac{0.387 Ra^{1/6}}{\left[ 1 + \left( \frac{0.492}{Pr} \right)^{9/16} \right]^{8/27}} \right\}^2 \quad (76)$$

Where  $Pr$  is the Prandtl dimensionless number [27].

All the quantities described above need to be computed for both biogas and Nitrogen streams. In general, these thermophysical properties are computed at the mean fluid temperature and are retrieved by an online calculator, available at *engineering toolbox* website [21]. Here,  $\text{CH}_4$  and  $\text{N}_2$  properties are available at atmospheric pressure and over a wide temperature range ( $-160 \text{ }^\circ\text{C} \div 700 \text{ }^\circ\text{C}$ ), while for  $\text{CO}_2$  such range is limited up to  $-60 \text{ }^\circ\text{C}$ . Hence, in the latter case, the same procedure for specific heat estimation is exploited, described in section 3.2.1: plotting the value obtained at different temperatures a fitting analysis is performed, retrieving an equation

describing the property behaviour as a function of temperature. Such equations allowed to estimate the unknown properties at the mean fluid temperature  $T_m$ . Subsequently, properties have to be referred to the biogas mixture. Density is averaged over its volume composition, i.e. 60 % vol. of CH<sub>4</sub> and 40 % vol. of CO<sub>2</sub>, or it can be estimated through Eq. (67). Conversely, thermal conductivity and dynamic viscosity are referred to the biogas mixture by mean of Eq. (77) [31].

$$pr_m = \frac{\sum y_i pr_i (MW_i)^{\frac{1}{3}}}{\sum y_i (MW_i)^{\frac{1}{3}}} \quad (77)$$

Where the term  $pr$  stands for the generical property, while  $y$  is the molar fraction and  $MW$  stands for the molecular weight. Subscript  $i$  identifies the  $i$ -th component of the gas mixture, whilst  $m$  identifies the mixture composition.

For what regards the pressure influence on such properties, it can be neglected. To prove this, in the engineering toolbox website, within the same page where the calculator is found, different plots at different pressures are available, in a range between 1 bar and 1000 bar. Concerning the curves representing the cases at 1 bar and 10 bar, it has observed that for each biogas component and for N<sub>2</sub> as well, the discrepancy was very tiny, thus allowing the assumption of neglecting the effect of pressure. To prove this, Figure 45 exhibits the CO<sub>2</sub> dynamic viscosity behaviour as temperature varies, at different pressures.

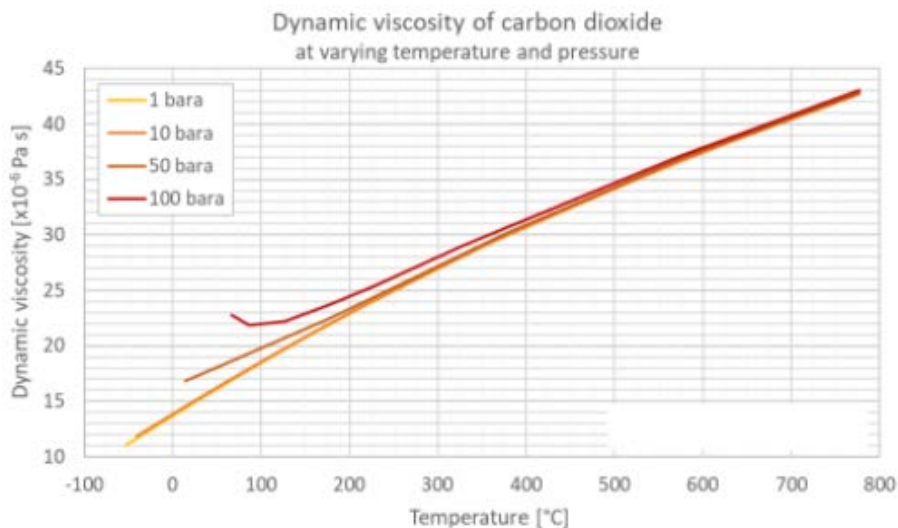


Figure 45 - Dynamic viscosity of CO<sub>2</sub> as temperature varies, at different pressures [21].

The yellow and orange curves are the one of interest. Observations demonstrate an overlapping of the two mentioned curves, hence proving that even for an increase of 10 bar such effect can be neglected. Furthermore, such a trend is confirmed for thermal conductivity.

For what regards methane, Figure 46 shows the dynamic viscosity as a function of both temperature and pressure. Looking at the yellow and orange curves, such trend is confirmed.

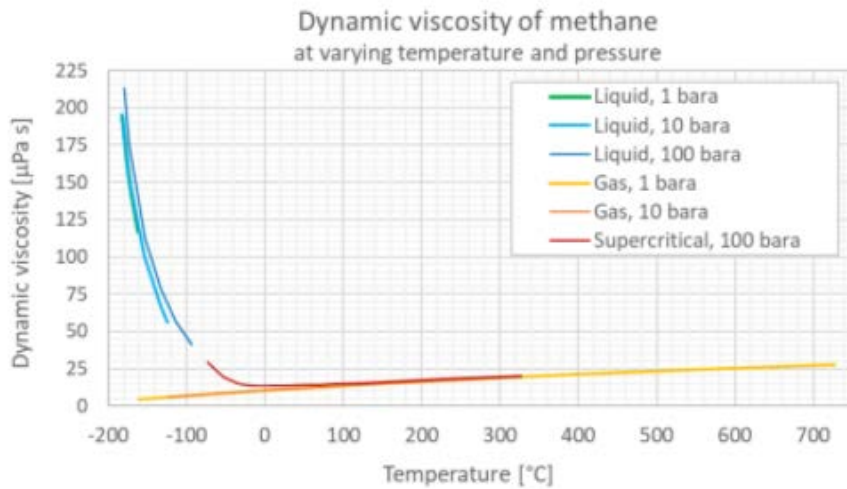


Figure 46 - Dynamic viscosity of methane as a function of both temperature and pressure [21].

The same consideration can be made concerning methane thermal conductivity.

Besides this, the thermal conductivity of stainless steel 316L has to be computed at the surface plate temperature  $T_s$ , whose value is supposed to be uniform over the whole plate surface. Hence, performing another fitting analysis, an equation describing the thermal conductivity as a function of temperature is retrieved. In Figure 47, both equation and the trend found are portrayed.

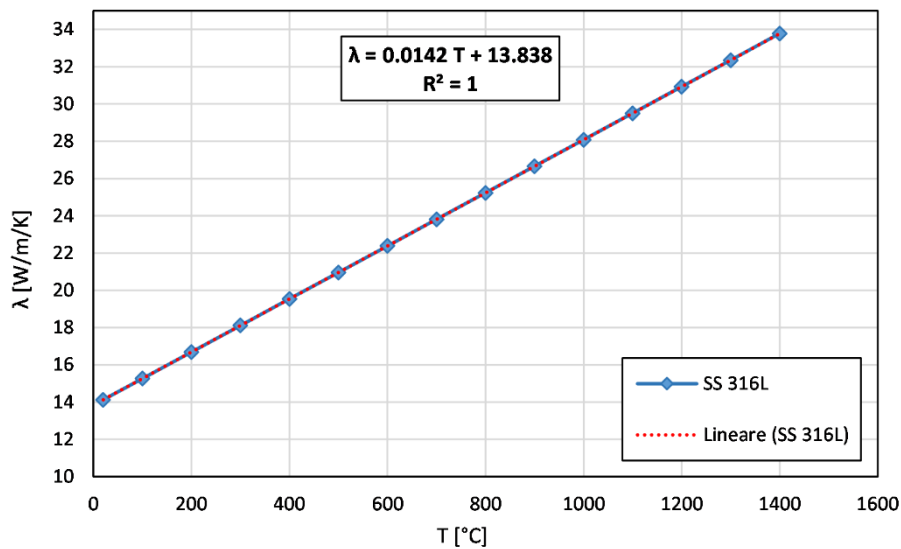


Figure 47 - Stainless steel 316L thermal conductivity trend as function of temperature, with the equation describing the curve behaviour, together with  $R^2$ .

The behaviour found is a straight line, allowing thus a quite accurate fitting, achieving an  $R^2$  equal to 1. Hence, as the temperature is lowered stainless steel thermal conductivity decreases as well.

Once the properties are estimated, the overall heat transfer coefficient can be computed. Results are presented as follows, illustrating the mean fluid and surface temperature employed, as well as properties estimation, used for computing both Rayleigh and Nusselt numbers.

In Table 24, temperature  $T_m$  and  $T_s$  are shown, at which properties are referred.

Table 24 – Mean fluid temperatures at which properties are estimated and surface temperature.

Component	Flow side	$T_m$ [°C]	$T_s$ [°C]
<b>ECO – HX</b>	Hot	-30.86	-32.00
	Cold	-42.50	-38.00
<b>CRYO – HX</b>	Hot	-73.36	-75.00
	Cold	-88.36	-85.00

It has to be pointed out that the plate surface temperature is assumed arbitrarily and to be different on the opposite plate sides. These results allowed thus to estimate all the properties mentioned above. In Table 25, such values are listed for biogas mixture stream within ECO-HX component.

Table 25 - Thermophysical properties for biogas stream within the ECO-HX.

Property	Hot-side	Cold-side
$\lambda$ [W/m/K]	0.0214	0.0201
$Pr$ [-]	0.75	0.76
$\mu$ [Pa s]	1.04E-05	9.90E-06
$\rho$ [kg/m <sup>3</sup> ]	2.03	2.13
$\nu$ [m <sup>2</sup> /s]	5.12E-06	4.65E-06
$c_p$ [J/kg/K]	1259.76	1243.08
$\alpha$ [m <sup>2</sup> /s]	8.39E-06	7.61E-06

The same is done for the CRYO-HX component, whose results are listed in Table 26.

Table 26 – Thermophysical properties for both biogas and  $N_2$  stream within CRYO-HX.

Property	Hot-side	Cold-side
$\lambda$ [W/m/K]	0.0163	0.0160
$Pr$ [-]	0.77	0.75
$\mu$ [Pa s]	8.34E-06	1.14E-05
$\rho$ [kg/m <sup>3</sup> ]	2.54	2.92
$\nu$ [m <sup>2</sup> /s]	3.28E-06	3.91E-06
$c_p$ [J/kg/K]	1200.00	1041.04
$\alpha$ [m <sup>2</sup> /s]	5.34E-06	5.27E-06

At this stage, exploiting equations (71), (73) and (76), the dimensionless numbers and the convective heat transfer coefficient are computed for both cold and hot side of the two heat exchangers. Results are listed in Table 27.

Table 27 – Dimensionless numbers and convective heat transfer coefficient results for CRYO-HX and ECO-HX.

Component	Flow side	$Ra$ [-]	$Nu$ [-]	$h$ [W/m <sup>2</sup> /K]
<b>ECO – HX</b>	Hot	1.51E+08	38.42	205.64
	Cold	7.56E+08	65.77	331.07
<b>CRYO – HX</b>	Hot	6.43E+08	62.60	254.91
	Cold	1.21E+09	76.84	307.76

Hence, in order to compute the overall heat transfer coefficient, the thermal conductivity of stainless steel 316L has to be evaluated. Its value is retrieved at the plate temperature, assumed as the arithmetic average between the surface temperatures on both cold and hot sides. In Table 28 such results are shown.

Table 28 - Stainless steel 316L thermal conductivity results.

Component	$\lambda$ [W/m/K]
<b>ECO – HX</b>	13.34
<b>CRYO – HX</b>	12.70

Finally, the overall heat transfer coefficient is computed for both ECO-HX and CRYO-HX, throughout Eq. (69). Such values are listed in Table 29.

Table 29 - Overall heat transfer coefficient of both ECO-HX and CRYO-HX.

Component	$U$ [W/m <sup>2</sup> /K]
<b>ECO – HX</b>	<b>125.89</b>
<b>CRYO – HX</b>	<b>138.21</b>

As can be noticed, the overall heat transfer coefficient for both heat exchanger is quite high. This is due to the high convective heat transfer coefficients, due to the great mass flow rates involved. However, high HTC is the characteristics of plate-fin heat exchangers, as was previously explained. Indeed, applying the LMTD method, thus exploiting Eq. (50) and (51), the heat transfer area required to realize the desired thermal exchanges, listed in Table 21, can be computed. Subsequently, making use of Eq. (68), which is provided by the technical datasheet of Pacetti company, the number of plates is retrieved. Thus, the total plate bundle length is estimated, as well as dimension A, Table 22, the encumbrance of each heat exchanger and finally the heating surface density. The latter is a parameter that compares the heat transfer area to the total heat exchanger volume, by making the ratio of such dimensions.

Table 30 exhibits the final heat exchangers dimensions that allow the required thermal power listed in Table 21.

*Table 30 - Heat exchangers final dimensions.*

<b>Component</b>	<b><i>ECO – HX</i></b>	<b><i>CRYO – HX</i></b>
$S_{th} [m^2]$	2.95	0.363
$np$	34	6
$A [mm]$	106.20	27.80
<b>HE volume <math>[m^3]</math></b>	0.0125	0.0033
<b>Heating surface density <math>[m^2/m^3]</math></b>	235.80	110.93

As it is shown, heat transfer areas  $S_{th}$  are significantly decreased with respect to those obtained in section 4.4, where around 40 m<sup>2</sup> for ECO-HX and 5 m<sup>2</sup> for CRYO-HX were exhibited. This trend is due to the high heat transfer coefficient involved within the plate-fin HE. Furthermore, the compactness of such equipment is also demonstrated by the parameter A, representing the heat exchanger depth, whose value never overcome the metre unit, and by the number of plates required to obtain such thermal exchanges. Hence, this reflects on the heat exchanger encumbrance, whose values are quite low, thus allowing to have greater heating surface densities. The latter implies that for a cubic metre encumbrance the heat transfer area of such equipment is very high, around 100-200 m<sup>2</sup>/m<sup>3</sup>. The last consideration leads to the proof of lower capital costs involved in the installation of such a component, as will be discussed as follows.

## 4.3 ECONOMIC ANALYSIS

### 4.3.1 Investment cost

In this section, an economic estimation of HE capital expenditure will be performed, in order to evaluate a final cost concerning the whole system. Other components prices are provided by Biokomp company so that the only unknowns are those related to the exchangers. By exploiting the cost functions, available on the Turton book [32], it will be assessed a capital cost for both CRYO-HX and ECO-HX, so that the overall expenditure for such a system could be compared with that of a traditional desulphurization system.

Hence, exploiting the knowledge of Turton book [32], the cost function for heat exchanger capital expenditure estimation are retrieved, as Eq. (78) states.

$$C_{BEC} = C_p^0 \cdot (B_1 + B_2 \cdot F_m \cdot F_p) \quad (78)$$

Where:

- $C_p^0$  is the equipment cost referred to the base conditions, whose value is given by Eq. (79).

$$C_p^0 = 10^{[K_1 + K_2 \log_{10} A + K_3 (\log_{10} A)^2]} \quad (79)$$

Where  $K_1$ ,  $K_2$ ,  $K_3$  are parameters to fit the expression to the real cost of the device, available in the literature depending on the HE type, while  $A$  is the so-called size parameter, that for heat exchangers corresponds to the area ( $m^2$ ).

- $F_m$  is the material factor, representing a correction parameter accounting for the specific material composing the equipment.
- $F_p$  is the pressure factor, whose value accounts for the discrepancy between the operating pressure from the base conditions. Its value is retrieved by computing Eq. (80).

$$F_p = 10^{[C_1 + C_2 \log_{10} P + C_3 (\log_{10} P)^2]} \quad (80)$$

Where  $C_1$ ,  $C_2$ ,  $C_3$  are parameters to fit the expression to the real conditions, whose values are available from tables; the term  $P$  stands for the operating pressure.

- $B_1$  and  $B_2$  are two other parameters, available in Turton book, and depend on the HE types.

Exploiting tables available in Turton book, all the above-mentioned parameters can be estimated. The cost function shown in Eq. (79) are referred to specific equipment size range, due to the validity range of the constant parameters. Hence, to account for the different

operating conditions, i.e. when the size parameter of the specific component is out of the cost function range, the six-tenth rule can be applied, as shown by Eq. (81).

$$\frac{C_1}{C_0} = \left(\frac{S_1}{S_0}\right)^{0.6} \quad (81)$$

Where  $C$  refers to the purchasing cost,  $S$  represents the equipment size, in this case the area. The subscripts 1 and 0 stands for the equipment with the required attribute and to that referred at the base conditions, respectively.

Moreover, the cost evaluated through Eq. (78) refers to a specific year, in such case to 2001 (year at which different parameters are available on the Turton book). Hence, the purchasing cost has to be converted into that of the present time, thus accounting for the changing in the economic conditions, as shown by Eq. (82).

$$\frac{C_2}{C_1} = \frac{I_2}{I_1} \quad (82)$$

Where  $I$  is the cost index, which includes all the time effect on the economy scale; subscripts 1 and 2 stands for, respectively, the base time at which cost is known and the time at which it is required. In the energy and chemical industry, the most commonly used cost indexes are the *MSECI (Marshall and Swift Equipment Cost Index)* and *CEPCI (Chemical Engineering Cost Index)*. The one that will be exploited is the CEPCI one, available at [33], where the corresponding value for the year 2020 is retrieved. In Table 31 results concerning the two HE cost estimation are presented.

Table 31 - Capital cost estimation for CRYO-HX and ECO-HX.

Component	CRYO-HX	ECO-HX
$K_1$	4.6656	4.6656
$K_2$	-0.1557	-0.1557
$K_3$	0.1547	0.1547
$B_1$	0.96	0.96
$B_2$	1.21	1.21
Parameter	Area [m <sup>2</sup> ]	Area [m <sup>2</sup> ]
A	2.95	0.363
Material	SS	SS
$F_M$	2.45	2.45
$F_p$	1	1
$C_p^0$ (2001) [€]	€ 389,762	€ 389,762
$C_{BEC}$ (2001) [€]	€ 1,529,623	€ 1,529,623
CEPCI 2001	394.00	394.00
CEPCI 2020	580.40	580.40
$C_{BEC}$ (2020) [€]	<b>€ 19,438</b>	<b>€ 68,294</b>

As can be noticed, the pressure factor is equal to 1. This is due to the null value of its constant parameters. Furthermore, parameter A is shown to be equal to 1000 m<sup>2</sup>. Indeed, the range of validity for the estimation of  $C_p^0$  is between 10 m<sup>2</sup> and 1000 m<sup>2</sup>. Thereby, its estimation is performed considering the upper limit of such range, that is subsequently referred to the actual areas, listed in Table 30, through Eq. (81). However, it can be observed how the capital cost of both heat exchanger is quite cheap, proving thus that the compactness of such equipment ensures lower economic expenditure, guaranteeing high heat transfer area. Hence, the type of heat exchanger picked is demonstrated to be suitable for such an application, allowing to reduce the costs of the whole system and ensuring good thermodynamic behaviours.

Finally, the total plant cost can be estimated. Indeed, in Table 32 all the capital expenditure that will be incurred are presented. It is shown that the overall system cost amounts to around € 335,000.

*Table 32 - Capital costs for the cryogenic system.*

<b>Description</b>	<b>Cost</b>
COMPRESSOR	€ 38,000
CHILLER	€ 4,500
STIRLING ENGINE	€ 104,350
ECO-HX	€ 68,294
CRYO-HX	€ 19,438
TRANSPORT OF THE STIRLING AND CRIOSYSTEM	€ 3,500
CONTAINER AND CANOPY	€ 32,000
ELECTRICAL CONNECTION AND WIRES	€ 7,000
CARBON VESSEL SYSTEM AND DUST FILTER	€ 6,500
ASSEMBLY	€ 6,500
TECHNICAL DOCUMENTATION, USER MANUALS AND CERTIFICATIONS	€ 9,500
PIPELINE, FLEXIBLE PIPES, GASKETS, SCREWS AND BOLTS	€ 17,000
ELECTRICAL BOX, PLC AND SOFTWARE	€ 15,000
TRASPORT FROM BOKOMP SITE (IT) TO LITHUANIA	€ 3,500
<b>Total cost</b>	<b>€ 335,081</b>

Instead, if a blower is installed, such capital cost can be lowered up to € 275,364. The main reason of such decrease can be computed to two factors. The first, is due to the lower blower capital expenditure, whose price amounts to € 2,297. Conversely, the heat exchanger size in such case decreases as well, due to the lower heat transfer areas involved, as a result of the

smaller volumetric biogas flow that the system can treat. However, the sizing with these operating conditions is avoided because it shows the same thermodynamic results. Besides this, being a demonstration project, Biokomp decided to install a compressor, in order to explore different operating conditions. If 1.5 bar will be proved to be the most suitable pressure condition, a blower would be sufficient to achieve the purpose the system is designed for, so that the cost will be lowered by 17.82%, from € 335.000 to € 275.000.

Furthermore, it has to be pointed out that costs listed in Table 32 are not the selling prices from the customer's point of view, but they only represents the costs of each component taken from the supplier. Indeed, there is a lack of engineering, direct and indirect costs, safety margins, company profits, and so on.

Conversely, for a typical desulphurization system its capital cost amounts to €50,000 for polyurethane plant, while for a steel-realized plant such cost increases up to € 90,000. However, Biokomp company provided a comparative table listing capital costs involving a chemical desulphurization system polyurethane-made, one of those described in section 1.1.1, for sulphur compounds removal. These quantities are exhibited in Table 34.

*Table 33 - Capital costs for a traditional desulphurization system.*

<b>Description</b>	<b>Cost</b>
COMPRESSOR	€ 38,000
BLOWER	€ 2,297
DESULPHURIZATION SYSTEM	€ 50,000
DEHUMIDIFICATION SYSTEM	€ 17,000
TRANSPORTATION OF DEHUMIDIFICATION AND DESULPHURIZATION UNITS	€ 15,000
ELECTRICAL CONNECTION AND WIRES	€ 20,000
SILOXANE CARBON VESSEL SYSTEM AND DUST FILTER	€ 10,000
ASSEMBLING	€ 20,000
TECHNICAL DOCUMENTATION, USER MANUALS AND CERTIFICATIONS	€ 15,000
PIPELINE, FLEXIBLE PIPES, GASKETS, SCREWS AND BOLTS	€ 30,000
ELECTRICAL BOX, PLC AND SOFTWARE	€ 10,000
CRANE FOR THE INSTALLATION	€ 5,000
<b>Total Costs</b>	<b>€ 232,297</b>

It can be noticed how the total capital cost is lower than around € 100,000. Moreover, considering that the desulphurization system is able to remove from 1000 ppm to 50 ppm, an

activated carbon-based adsorption bed should be installed downstream, thus increasing the overall capital expenditure. Even in this case, the considerations done for Table 32 are true.

In Figure 48 a comparison between the capital costs of the two different solution is presented.

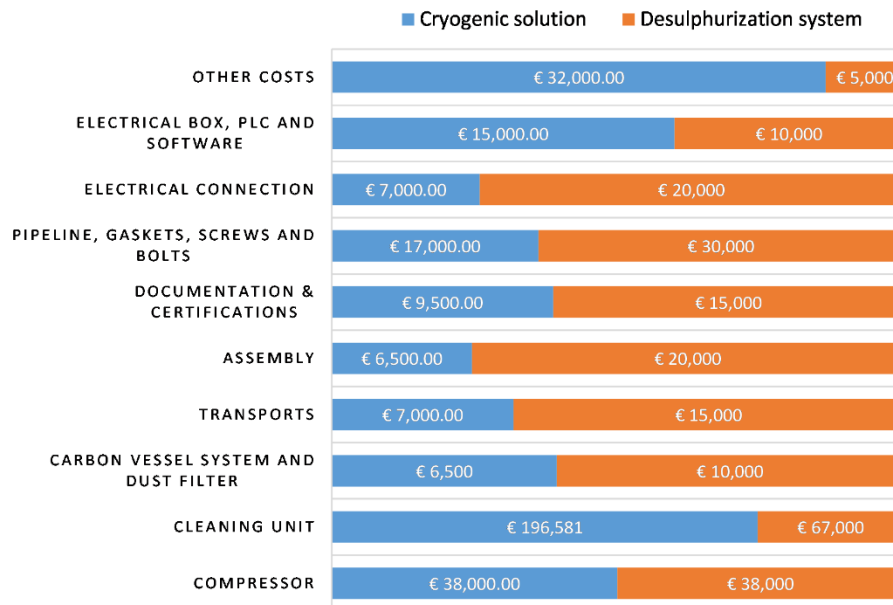


Figure 48 – Capital costs for the two system configurations; within the cleaning unit are summarized different equipment costs: for the cryogenic solution, it includes HEs, Stirling engine and chiller components. While, for the desulphurization system, the cleaning unit groups both desulphurization and dehumidification systems.

The highest cost discrepancy is observed at the cleaning unit, where the cryogenic solution exhibits a cost of € 196,581 against € 67,000 registered for traditional desulphurization system. The main difference lies on the Stirling engine cost, that cover more than half of the cleaning unit cost. However, it can be further noticed how in general costs involved in the cryogenic solution are lower than those accounted for the desulphurization system, although the overall capital costs are 30.67 % higher.

#### 4.3.2 Operating cost

The comparison between the innovative cryogenic solution and the standard desulphurization system is also performed for what concerning operating costs. The electric power consumption of both compressor and chiller are available from Biokomp. It is stated that with these working conditions, the compressor consumption,  $W_{el_{compressor}}$ , should amount up to 10 kW, whilst the chiller should spend around 4.5 kW of electricity,  $W_{el_{chiller}}$ . Concerning the Stirling engine, its power consumption,  $W_{el_{stirling}}$ , is retrieved from the SPC-1 cooling power curve, Figure 18, looking at the blue curve. To cool the biogas down up to -80 °C, 5.5 kW of electrical power should be spent. Operating cost are listed in Table 33.

Table 34 - Electrical consumption of the cryogenic cleaning unit.

$W_{el_{compr}}$	10 kW
$W_{el_{chiller}}$	4.50 kW
$W_{el_{stirling}}$	5.50 kW
<b>Total consumption</b>	<b>20 kW</b>

Thus, considering a capacity factor (CF) of 0.9, the yearly electrical consumption amounts to 157,680 kWh/y. Then, Considering the electricity cost for Lithuanian companies, from [34] it is retrieved that such costs is estimated to be 0.076 €/kWh. Hence, the annual electrical expenditure to drive such a system can be evaluated, corresponding to **11,984 €/y**. Finally, retrieving the total amount of biogas treated per year, whose value is 1,182,600 m<sup>3</sup>/y, a cost per unit volume can be estimated: 0.0101 €/m<sup>3</sup>. It has to be pointed out that such estimation is incomplete, due to the lack of information on other operating costs, such as general maintenance costs, components substitution, and other operating expenditures.

Operating costs are also available for the traditional desulphurization system, concerning chemical agents and electrical consumptions. In Table 35 components involving electricity expenditure are presented, where  $W_{el_{DH}}$  stand for the dehumidification system electrical consumption, whilst  $W_{el_{DS}}$  represents the electrical consumption for the desulphurization system.

Table 35 - Electrical consumption of a traditional desulphurization system.

$W_{el_{compr}}$	10 kW
$W_{el_{DH}}$	5 kW
$W_{el_{DS}}$	10 kW
<b>Total consumption</b>	<b>25 kW</b>

Hence, considering a capacity factor of 0.9, the annual electrical power consumption is 197,100 kWh/y. Considering the electricity price for Lithuanian companies, the annual cost for electricity expenditure is **14,980 €/y**. On the other hand, in Table 36 chemical agents' expenditures are listed, together with their annual costs.

Table 36 - Chemical agent costs for a traditional desulphurization system.

Chemical	NaOH	Additive EC-3
Mass consumption [g/h]	60 g/h	120 g/h
Price [€/kg]	0.30 €/kg	1.10 €/kg
Annual cost [€/y]	141.91	1,040.69

Hence, summing up the yearly expenditures, it is found that **€ 16,162/y** are spent. There would be at least the disposal of exhausted products, saturated with sulphur compounds and any other impurities to be added to such estimation, but no data were available from Biokomp company. Despite this, such value can be compared with that obtained for the cryogenic system: it can be said that using a traditional desulphurization system will implies higher operating costs, despite it involves lower capital expenditures, as illustrated in Figure 49.

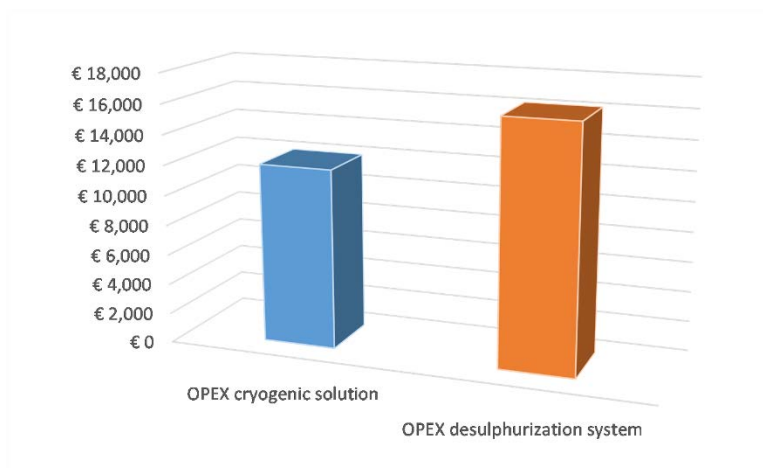


Figure 49 – OPEX comparison between the two system configurations.

In general, it can be concluded that contaminants removal performed through the cryogenic system should involve 25.85 % lower operational expenditure, allowing to save € 4,179 per year, hence making them more convenient in terms of capital return. However, it has been demonstrated that the two different system configurations involves similar CAPEX (Capital Expenditure), with a discrepancy of € 100,000, which can be lowered for the cryogenic system by exploiting a blower instead of compressor, making thus such system configuration competitive with respect to those involving traditional sulphur removal systems.

## 5 CONCLUSIONS

---

In the present work, an overall sizing of a novel cryogenic system for biogas cleaning is performed. Such a system is meant to be designed and constructed by Biokomp company, being a partner of the European project “Waste2Watts”. A brief discussion is conducted on the main existing technologies performing biogas cleaning, focusing on SOFC-based applications. Nowadays, main cryogenic system companies join their efforts on the bioLNG production, inducing the system to be designed as an innovative one. The layout of the mentioned system, illustrated in Figure 13, consists of a compressor followed by a dehumidification section and two heat exchangers, where biogas cleaning is performed through lowering the temperature up to cryogenic levels.

The thermodynamic behaviour of such a system is first estimated, in order to understand, together with Biokomp company, what are the optimal operating condition. To achieve such results, different P-x phase diagrams concerning the binary mixture CH<sub>4</sub>-CO<sub>2</sub> are drawn, at different operating temperatures. Exploiting the Yokozeky thermodynamic model-based software provided by the previous thesis writer, three main phase diagrams are considered, mainly at -80 °C, -90 °C and -100 °C, in a range between 1 bar and 5 bar of gauge pressure. These were used to retrieve the amount of CO<sub>2</sub> frosting at the different operating conditions. Results exhibited that for relatively high temperatures, i.e. -80 °C, no solid CO<sub>2</sub> is observed up to 2 bar. Conversely, lowering in temperature translates into an increasing amount of frosting CO<sub>2</sub>, as can be appreciated in Table 4.

Performing the overall system sizing, it has been observed how the maximum amount of biogas mass flow that the system can withstand increases as the CO<sub>2</sub> frosting fraction decreases. Such a trend, highlighted in Figure 29, is mainly due to the lower fraction of sensible heat exploited within the cryogenic heat exchanger. Indeed, increasing the pressure, at lower temperatures, involves higher amounts of CO<sub>2</sub> solid formation, whose phase transition is observed to be exothermic. Hence, the fraction of latent heat increases, which has to be removed by the refrigerant fluid flow. This behaviour reflects also on the thermal power exchanged within the ECO-HX. Figure 32 exhibits economizer heat transfer rate at the different operating condition. It is observed the same behaviour shown by the mass flow. Indeed, these two quantities are directly proportional, since biogas stream is found on both hot and cold sides.

Subsequently, a qualitative estimation of the heat transfer areas is performed. Since no information was given on heat exchangers, the *LMTD* and  $\epsilon - NTU$  methods are exploited. Furthermore, due to the phase change within CRYO-HX, such methods are observed to do not

be the most suitable. Indeed, two different methods are developed, in order to have an estimation for the CRYO-HX heat transfer surface, both based on the lumped parameters models. Concerning the ECO-HX, the computed values are exact, due to no phase transition occurring, whose values vary from around 40 m<sup>2</sup> to 0.5 m<sup>2</sup>. Also, in this case, the heat transfer area is shown to be dependent on the carbon dioxide frosting percentage, due to the relation with the thermal power exchanged at the different operating conditions. The same trend is observed concerning CRYO-HX. Here, results obtained are affected by a certain amount of uncertainty, due to the strong assumption made in the two methods applied. However, both procedures showed similar results, with heating surfaces varying from around 5 m<sup>2</sup> to 0.5 m<sup>2</sup>, appreciable in section 3.4.

Finally, once a qualitative thermodynamic behaviour is established, a final scenario can be explored. The optimal operating conditions are identified, for which a realistic design is performed. Some constraints are fixed together with Biokomp company, regarding maximum flow rate the system can withstand, i.e. 150 m<sup>3</sup>/h of incoming biogas. The system is then designed on the thermodynamic point of view, and a heat exchanger type is chosen in order to estimate the overall system capital cost. The most suitable heat exchanger is found to be the plate-fin type. Such equipment has been proved to be compact and to realize high heat transfer surfaces, as can be observed in Table 30. Indeed, the plate corrugation act as a fin, thus increasing the heat transfer rate, resulting in higher HTC, as shown in Table 29. Furthermore, their compactness is shown to results in lower capital costs, thus leading such cryogenic technique to be competitive in the market.

Finally, an economic comparison is carried considering to realize such a process with either cryogenic or desulphurization system. It has proved, notwithstanding the lack of further information, that cryogenic solution involves lower operational costs, as no chemical agents are used and therefore do not need to be disposed of.

In conclusion, it has to be said that experimental tests have to be performed in order to validate such results. Furthermore, the present study does not include the effect of H<sub>2</sub>S on the biogas mixture, even though it has been found, in literature, that working at these temperature and pressure conditions, it should be condensate. However, this case is demanded to further experimental developments.

## REFERENCES

---

- [1] "Waste2Watts." <https://waste2watts-project.net/description/>.
- [2] A. Lussier, S. Sofie, J. Dvorak, and Y. U. Idzerda, "Mechanism for SOFC anode degradation from hydrogen sulfide exposure," *Int. J. Hydrogen Energy*, vol. 33, no. 14, pp. 3945–3951, 2008, doi: 10.1016/j.ijhydene.2007.11.033.
- [3] H. Madi *et al.*, "Solid oxide fuel cell anode degradation by the effect of siloxanes," *J. Power Sources*, vol. 279, pp. 460–471, 2015, doi: 10.1016/j.jpowsour.2015.01.053.
- [4] Desotec, "Desotec iron sponge process." <https://www.desotec.com/it/carbonologia/casi/hydrogen-sulphide-removal-biogas-part-1>.
- [5] AirScience, "AirScience desulphurization system." <https://www.airscience.ca/purification-by-desulfurization>.
- [6] H. Wasajja, R. E. F. Lindeboom, J. B. van Lier, and P. V. Aravind, "Techno-economic review of biogas cleaning technologies for small scale off-grid solid oxide fuel cell applications," *Fuel Process. Technol.*, vol. 197, no. September 2019, p. 106215, 2020, doi: 10.1016/j.fuproc.2019.106215.
- [7] Paqell, "THIOPAQ O&G description - Paqell company." <https://www.paqell.com/thiopaq/process-description/>.
- [8] J. Hofmann *et al.*, "J. Hofman *et al.*," *Pressureless cryogenic conversion of biogas into liquefied biomethan and solid carbon dioxide*. 2016.
- [9] Y. Tan, W. Nookuea, H. Li, E. Thorin, and J. Yan, "Cryogenic technology for biogas upgrading combined with carbon capture-a review of systems and property impacts," *Energy Procedia*, vol. 142, pp. 3741–3746, 2017, doi: 10.1016/j.egypro.2017.12.270.
- [10] M. J. Tuinier and M. Van Sint Annaland, "Biogas purification using cryogenic packed-bed technology," *Ind. Eng. Chem. Res.*, vol. 51, no. 15, pp. 5552–5558, 2012, doi: 10.1021/ie202606g.
- [11] Cryo pur, "Cryo pur cryogenic system." <http://www.cryopur.com/it/tecnologia/>.
- [12] PG&E, "Cryogenic Separation. Technical Analysis," pp. 1–15, 2018.
- [13] Pioneer, "Pioneer Air System -DCR system." <https://pioneerair.com/biogas-treatment/>.
- [14] "StirLIN-2 Liquid Nitrogen System," 2016.
- [15] F. Falco, "Application of the Yokozeki thermodynamic model for the design of an innovative cryogenic system for biogas purification," 2020.
- [16] A. Yokozeki, "Analytical Equation of State for Solid-Liquid-Vapor Phases," *Int. J.*



- [33] Chemical engineering, "CEPCI cost index." <https://www.chemengonline.com/2020-cepci-updates-july-prelim-and-june-final/>.
- [34] GlobalPetrolPrice, "Globalpetrolprices.com." [https://it.globalpetrolprices.com/Lithuania/electricity\\_prices/](https://it.globalpetrolprices.com/Lithuania/electricity_prices/).
- [35] S. Cryogenics, "spc-1-cryogenerator." <https://www.stirlingcryogenics.eu/en/products/cryocoolers/spc-1-cryogenerator>.
- [36] Simuwu, "brazed-plate-heat-exchanger." <https://www.simuwufurnace.com/technical-news/brazed-plate-heat-exchanger.html>.